สายอากาศแถวลำดับสะท้อนไมโครสตริปโดยใช้เทคนิค การกระจัดกระจายด้านหลัง

นางสาวปิยาภรณ์ กระฉอดนอก

วิทยานิพนธ์นี้เป็นส่วนหนึ่งของการศึกษาตามหลักสูตรปริญญาวิศวกรรมศาสตรดุษฎีบัณฑิต
สาขาวิชาวิศวกรรมโทรคมนาคม
มหาวิทยาลัยเทคโนโลยีสุรนารี
ปีการศึกษา 2550

MICROSTRIP REFLECTARRAY ANTENNA

USING BACKSCATTERING TECHNIQUE

Piyaporn Krachodnok

A Thesis Submitted in Partial Fulfillment of the Requirements for the

Degree of Doctor of Philosophy in Telecommunication Engineering

Suranaree University of Technology

Academic Year 2007

MICROSTRIP REFLECTARRAY ANTENNA

USING BACKSCATTERING TECHNIQUE

Suranaree University of Technology has approved this thesis submitted in partial fulfillment of the requirements for the Degree of Doctor of Philosophy.

Thesis Examining Committee

_____

(Prof. Dr. Monai Krairiksh)

Chairperson

_____

(Asst. Prof. Dr. Rangsan Wongsan)

Member (Thesis Advisor)

_____

(Asst. Prof. Dr. Chuwong Phongcharoenpanich)

Member

_____

(Asst. Prof. Dr. Rangsan Tongta)

Member

_____

(Asst. Prof. Dr. Chanchai Thongsopa)

Member

_____	_____
(Prof. Dr. Pairote Sattayatham)	(Assoc. Prof. Dr. Vorapot Khompis)
Vice Rector for Academic Affairs	Dean of Institute of Engineering

ปิยาภรณ์ กระฉอดนอก : สายอากาศแถวลำดับสะท้อนไมโครสตริปโดยใช้เทคนิคการกระจัดกระจายด้านหลัง (MICROSTRIP REFLECTARRAY ANTENNA USING BACKSCATTERING TECHNIQUE) อาจารย์ที่ปรึกษา : ผู้ช่วยศาสตราจารย์ ดร. รังสรรค์ วงศ์สรรค์, 164 หน้า.

วิทยานิพนธ์ฉบับนี้นำเสนอสายอากาศชนิดแถวลำดับสะท้อนไมโครสตริป (microstrip reflectarray) โดยใช้เทคนิคการกระจัดกระจายด้านหลัง ซึ่งโครงสร้างของสายอากาศประกอบด้วยตัวสะท้อนที่มีลักษณะราบเรียบและสายอากาศป้อนกำลังคลื่นวางที่ด้านหน้าตัวสะท้อน พื้นผิวตัวสะท้อนประกอบด้วยแถวลำดับของแผ่นสะท้อนวางบนแผ่นวงจรพิมพ์โดยไม่มีสายนำสัญญาณ สายอากาศดังกล่าวถูกออกแบบด้วยเทคนิคการจัดเฟสของสัญญาณให้เกิดคุณลักษณะเสมือนผิวโค้งของสายอากาศตัวสะท้อนที่มีการป้อนสัญญาณเข้าที่ด้านหลังตัวสะท้อน โดยใช้การควบคุมเฟสด้วยวิธีปรับขนาดแผ่นสะท้อน เพื่อทำให้เกิดความกว้างลำคลื่นขนาดใหญ่ ซึ่งจะสามารถควบคุมให้ลำคลื่นแมตช์กับพื้นโลก (earth-matched beam) ได้ ข้อดีของสายอากาศชนิดนี้คือ ต้นทุนต่ำ น้ำหนักเบา และติดตั้งง่าย วัตถุประสงค์ของสายอากาศชนิดนี้ได้ถูกนำเสนอเพื่อใช้สำหรับสถานีฐานของการสื่อสารเครือข่ายท้องถิ่นแบบไร้สาย (Wireless Local Area Network : WLAN) ที่ต้องการสายอากาศเพียงตัวเดียวในการแผ่กระจายคลื่นในห้องขนาดใหญ่ หรือเพื่อใช้สำหรับดาวเทียมวงโคจรต่ำ (Low Earth Orbit : LEO) ขนาดเล็ก สำหรับการวิเคราะห์เพื่อหาคุณลักษณะของแผ่นสะท้อนนั้น ได้นำระเบียบวิธีโมเมนต์ (Method of Moments : MoM) มาใช้ในการคำนวณเพื่อหาคำตอบของสมการอินทิกรัล โดยใช้ค่าฟังก์ชันกรีนไดแอดิก (dyadic Green's function) ซึ่งเป็นผลตอบสนองของสนามที่จุดสังเกตอันเนื่องมาจากจุดกำเนิด และใช้การวิเคราะห์แผ่นสะท้อนด้วยหลักการแถวลำดับอนันต์ (infinite array) มาช่วยในการคำนวณ จะทำให้ได้คุณสมบัติของสายอากาศที่สำคัญ คือค่าสัมประสิทธิ์การสะท้อน (reflection coefficient) นอกจากนั้นวิทยานิพนธ์ฉบับนี้ได้นำเสนอการสังเคราะห์สายอากาศแถวลำดับสะท้อนไมโครสตริปที่ใช้เทคนิคการจัดเฟสของสัญญาณให้เกิดคุณลักษณะเสมือนผิวโค้งที่มีรูปทรงเป็นไปตามสมการเรขาคณิตแบบต่างๆ ได้แก่ สามเหลี่ยม ควอเดรติค โคไซน์ โคไซน์ยกกำลังสอง เกาส์ วงกลม และพาราโบลิก เพื่อวิเคราะห์หาคุณลักษณะของสายอากาศ ได้แก่ การประวิงเฟส (phase delay) แบบรูปการแผ่พลังงาน (radiation pattern) อัตราขยายสูงสุด (maximum gain) และความกว้างลำคลื่นครึ่งกำลัง (half-power beamwidth) จากนั้นจะเลือกตัวสะท้อนที่มีคุณลักษณะเหมาะสมสำหรับการแผ่กระจายคลื่นในห้องขนาดใหญ่มาสร้างสายอากาศต้นแบบที่ความถี่ 10 GHz เพื่อนำไปวัดทดสอบคุณลักษณะเปรียบเทียบความแม่นตรงกับผลการคำนวณ จากการวัดทดสอบสายอากาศต้นแบบพบว่า สายอากาศที่ออกแบบ

มีแบบรูปการแผ่พลังงานใกล้เคียงกับผลที่ได้จากการคำนวณ ซึ่งสามารถนำผลที่ได้ไปใช้ในการออกแบบสายอากาศตามวัตถุประสงค์ดังกล่าวต่อไป และในส่วนสุดท้ายของวิทยานิพนธ์ได้นำเสนอการปรับปรุงประสิทธิภาพของสายอากาศแถวลำดับสะท้อนแบบลำคลื่นกว้างด้วย

สาขาวิชาวิศวกรรมโทรคมนาคม ลายมือชื่อนักศึกษา_____

ปีการศึกษา 2550 ลายมือชื่ออาจารย์ที่ปรึกษา_____

PIYAPORN KRACHODNOK : MICROSTRIP REFLECTARRAY ANTENNA USING BACKSCATTERING TECHNIQUE. THESIS ADVISOR : ASST. PROF. RANGSAN WONGSAN, Ph.D. 164 PP.

REFLECTARRAY/BROAD-BEAM ANTENNA/METHOD OF MOMENTS

This thesis presents the microstrip reflectarray antenna using backscattering technique. The antenna structure consists of a flat reflector and an exciting feed at the front of reflector. On the reflecting surface, there are many isolated printed patches which array on flat printed circuit board (PCB) without any transmission line power dividers. To achieve broad-beamwidth and hence earth-matched beam antenna, reflectarray antenna is specifically designed to emulate the curvature of the back-feed reflector by using variable patch size. This antenna fulfills the need for low cost, light weight, and easy installation. The proposed antenna is aimed to use for base station of Wireless Local Area Network (WLAN) communication, which require only one antenna for field radiating in the large room, or for small Low Earth Orbit (LEO) satellite. For the element characteristics analysis, the Method of Moments (MoM) is used to solve the integral equation. By using the infinite array analysis and the dyadic Green's function, the response of field at the observation point due to the source, the required property such as reflection coefficient is calculated. In addition, this thesis presents the synthesis of microstrip reflectarray antenna that emulates the back-feed curved reflector antenna which have the various functions of elementary geometries i.e., triangular, quadratic, cosine, circular, squared cosine, Gaussian, and parabolic. The antenna characteristics i.e., phase delay, radiation pattern, maximum gain and

half-power beamwidth of the variety of reflectarray types are analytically determined. Furthermore, the reflector which has appropriate characteristics for field radiating in the large room will be constructed antenna model at 10 GHz. The reflectarray antenna will be realized and experimented to validate the technique and the developing analysis tool. It is obvious that the designed antenna provides the agreement with the calculated results. The results from the investigation can be applied for designing the antenna for further applications. In the last part, this thesis investigates performance improvement for broad-beam microstrip reflectarray antenna.

School of Telecommunication Engineering Student's Signature_____

Academic Year 2007 Advisor's Signature_____

ACKNOWLEDGEMENT

I would like to take this opportunity to express my gratitude to many individuals who concerned in the completion of this thesis.

First of all, I am so grateful to my advisor, Asst. Prof. Dr. Rangsan Wongsan, who has been giving me helpful suggestion and stimulating the progress of this research since the first day I became his advisee. I also appreciate his kindness in accepting me as one of his advisees.

I would like to express my gratitude to the thesis examination committees, Prof. Dr. Monai Krairiksh, Asst. Prof. Dr. Rangsan Tongta, Asst. Prof. Dr. Chuwong Phongcharoenpanich, and Asst. Prof. Dr. Chanchai Thongsopa, for their invaluable advices and kind supports.

Special thanks for the fellow members of the Wireless Communication Research & Labolatory, Suranaree University of Technology, for their best wishes and wonderful friendships.

Finally, I am greatly indebted to all of my teachers in the past and my family, who love me much and exactly understand my life throughout the study period.

Piyaporn Krachodnok

TABLE OF CONTENTS

Page

TABLE OF CONTENTS (Continued)

Page

TABLE OF CONTENTS (Continued)

Page

TABLE OF CONTENTS (Continued)

Page

TABLE OF CONTENTS (Continued)

Page

TABLE OF CONTENTS (Continued)

Page

LIST OF TABLES

Table **Page**

LIST OF FIGURES

Figure **Page**

LIST OF FIGURES (Continued)

Figure **Page**

LIST OF FIGURES (Continued)

Figure **Page**

LIST OF FIGURES (Continued)

Figure **Page**

CHAPTER I

INTRODUCTION

1.1 Background of Problems and Significance of the Study

With the extensive growth of the communication technology especially for wireless communication system, an antenna is an important component to propagate signal energy in a desired direction. The characteristics of antennas (performance, technology, and cost) are important issues in wireless communication systems. The shaped-beam antenna for satellite communication was first developed to achieve approximately uniform coverage of the earth (Kishk, 1989; Hay, Bateman, Bird, and Cooray, 1999; Olver, Clarricoats, Kishk, and Shafai 1994). Recently, the similar requirement but different applications; that is, the indoor high speed data transmission: wireless local area networks (WLAN) operating in the millimeter wave, again attracts considerable attentions (Bird, Kot, Nikolic, James, and Barker, 1994; Fernandes, C.A. and Fernandes, J.G., 1999; Smulders and Herben, 2001; Smulders, Khusial, and Herben, 2001). Especially, the large-scale indoor base station of such system, it is desirable the wider-beam antenna for covering an effectively broad area. Therefore, the widely circular beam antenna is an alternative for WLAN applications as shown in Figure 1.1. The required important feature is the transmitted power that has to be efficiently distributed over the coverage whereas outside the coverage the field strength has to fall off rapidly.

In order to meet this stringent requirement toward omnipresent communication, a significant number of technological challenges will need to be researched. The related literatures have been reported by several authors. In Smulders, Khusial, and Herben (2001), the authors presented the design of a 60 GHz shaped reflector antenna for WLAN access points by using backscatter reflector, which was fabricated from the modified parabolic surface. Also, Wongsan and Thaivirot (2006) presented the synthesis of radiation patterns, which were radiated from the variety of shaped backscatters to provide the different wide beams for indoor WLAN applications. From these researches, the backscatters have been fabricated from the circular metallic sheet that their surfaces are shaped to be geometric curvature. In case of indoor WLAN systems and small LEO satellites, such antennas are improper because their structures suffer from mechanical drawbacks such as bulkiness and the need for an expansive custom mold for each new coverage specification, which greatly increase the cost.

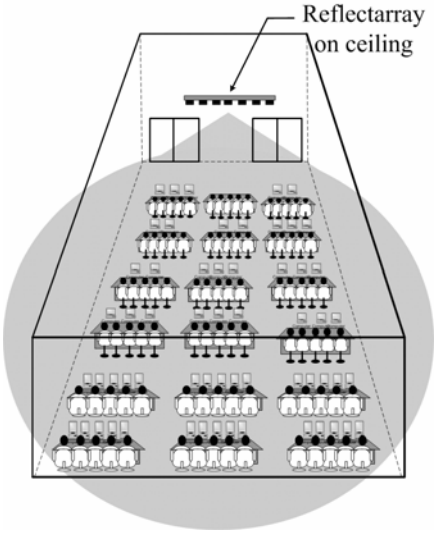

Figure 1.1 Reflectarray for WLAN large-scale indoor base station.

Recently, a novel type of antenna that combines some of the best feature of microstrip array and parabolic reflector was presented in Munson, Haddad, and Hanlen (1987). The microstrip reflectarray consists of a flat reflector and an exciting feed at the front of reflector. On the reflecting surface, there are many isolated elements (e.g. printed patches, dipoles, or rings), which array on flat printed circuit board (PCB) without any transmission line power dividers. The reflection phase from the reflectarray elements are designed so that the reflected energy from the array is collimated to form a main beam in a given direction. A reflectarray configuration is attractive because it allows a single mechanical design to be used repeatedly for a wide variety of different coverage specifications without the need for expensive fabrication of a new mold. The only change of dimension of printed reflecting elements are required in order to generate the different beams. Thus, many of the high recurring costs associated with shaped-reflector antennas can be eliminated with flat printed reflectarrays (Pozar, Targonski, and Pokuls, 1999). The flat geometry of a reflectarray also lends itself to easier placement and deployment on the WLAN large-scale indoor base station and small low earth orbit (LEO) satellites and also in terms of manufacture. In addition, a flat printed reflectarray antenna fulfills the antenna requirement for low cost, low profile, light weight, and easy installation.

This thesis concentrates on a microstrip reflectarray antenna using discretization of elementary geometrical functions to form a wide beam antenna. A microstrip reflectarray antenna consists of a single dielectric layers with periodic arrays of etched conductive microstrip elements, designed to efficiently transform an incident electromagnetic field into collimated radiation. Reflectarray operates by impressing a phase shift on the reflected energy. The aperture phase delay of

reflectarray elements are calculated and synthesized to compare for each geometrical function. Moreover, this thesis presents a full-wave moment method treatment of the field scattered by an infinite uniform array of conducting elements, and this tool is used to generate the required element design data for implementing microstrip reflectarray. Using these tools, 30×30 cm reflectarray model was designed, manufactured, and tested at 10 GHz.

1.2 Research Objectives

The objective of this research is organized as follows:

1.2.1 To study the method to design and develop microstrip reflectarray antenna for WLAN large-scale indoor base station and small LEO satellite.

1.2.2 To control the half-power beamwidth (HPBW) of antenna to form earth matched beam and to provide coverage area by using single antenna.

1.2.3 To validate the proposed concept, an X-band microstrip reflectarray antenna will be designed based on the developed Method of Moments (MoM) analysis tool.

1.3 Scope and Limitations of the Study

The phase and radiation pattern synthesis method for microstrip reflectarray that has to illuminate a predefined circular area are presented by using variety of the discretization of elementary geometrical functions such as, triangular, quadratic, cosine, circular, squared cosine, Gaussian, and parabolic distributions. These backscatter functions are discussed on merit and demerit to find appropriate radiation characteristics such as radiation pattern, -3 dB beamwidth, and maximum gain for

utilization in WLAN application. To design the propose antenna, the Method of Moments (MoM) and the infinite-array are applied to calculate the scattering coefficients characteristic. Then, phase of reflected fields are obtained and the actual size of microstrip patch elements are known. Having confirmed the validity of this approach, the X-band antenna prototype is designed and developed. This reflectarray is tested experimentally.

1.4 Expected Benefits

1.5.1 To obtain a broad-beam microstrip reflectarray antenna by using patch of different sizes.

1.5.2 To obtain the simulation program which develop from MoM and can apply to use with the realize problem of microstrip reflectarray analysis.

1.5.3 To obtain a conclusion about the shaped-beam microstrip reflectarray which is earth matched beam application.

1.5 Thesis Organization

The remainder of this thesis is organized as follows. In Chapter 2, we present several types of reflectarray design techniques found in the literatures from text books and academic publications. In addition, this chapter briefs overview of reflectarray antenna concept and provides theoretical backgrounds of reflectarray antenna for the design and analysis of a broad-beam microstrip. The method of moment and the infinite-array are applied to calculate the reflection phase characteristic.

In Chapter 3, we presents the design and synthesis of phase for microstrip reflectarray using the variety of discretization of elementary geometrical functions

such as, triangular, quadratic, cosine, circular, squared cosine, Gaussian, and parabolic distributions. The general approach will be presented to determine the required phase delay of reflectarray elements, which are duplicated the same radiating aperture as backscatters, which are determined on the construction of the curvature of a shaped backscatter surface with the help of Snell's law. In addition, we apply this approach into the variety of elementary geometrical functions to calculate the radiation patterns of reflectarrays. To compensate these phase delays, the elements must have corresponding phase advancements designed. Also, this section gives an example of how the compensating phase is calculated for each element of a reflectarray with a broadside-directed beam.

Having confirmed the validity of this reflectarray approach, the X-band antenna prototype is designed and developed which are given in Chapter 4. Properties of the material used in the designs are presented and the manufacturing process is also summarized. We select a reflectarray types in order to choose the best radiation characteristic for the WLAN large-scale indoor base station application. Furthermore, the experimental process was carried out, followed by a complete description of the results obtained in the anechoic chamber. Interpretation of the results will be made in addition to a comparison with the anticipated performance. Performance comparison between the simulated and measured results is also conducted.

In chapter 5, we propose performance improvement for broad-beam microstrip reflectarray antenna. The optimized feed distance is calculated from the aperture efficiency with considering spillover, taper, and feed blockage efficiencies and has investigated the influence of the feed position on the -3 dB beamwidth (HPBW) and gain performance. In addition, the influence of the unit cell size of reflectarray on the

gain performance has investigated. A reflectarray with different element sizes and reduced grid spacing have been designed at 10 GHz.

The last chapter, Chapter 6, provides conclusions of the research work and suggestion for future studies.

CHAPTER II

BACKGROUND THEORY

2.1 Introduction

The important requirements of future antennas are low-cost, simplicity in fabrication and easy operation. Despite reducing production costs of microstrip antennas, any cost reduction and ease of manufacturing of a large number of systems are highly desirable. In addition, the antenna needs to be highly reliable to provide continuous coverage to the user. The human aspect of the new design should not be overseen. Moreover, new antenna designs should aim at being lightweight and non-intrusion for enhancing reliability due to their simplicity. Given the strong requirement and challenges of developing new antennas for the wireless communications systems, the aim of this thesis is to investigate and design a broad-beam reflectarray antenna.

Since the microstrip reflectarray is a fairly new antenna concept, therefore, this chapter gives a more detailed discussion and literature surveys of up-to-date of the development history and key design methodologies for this antenna. A review of current antenna characteristics and the relevant reflectarray theory will be done. To achieve reflectarray antenna for WLAN large-scale indoor base station, an analytical approach is taken. In addition, this chapter will present the general design approach as far as it concerns the phase characteristic that describes the desired phase delay of reflectarray elements. The phase calibration will be established by using technique of

a full-wave Method of Moments including derived dyadic Green's function. The numerical tools for determining the reflection coefficients of an infinite array of uniform elements, which located on dielectric substrates, are developed. The effects of element geometry and dimensions on the array reflection coefficients are studied in Chapter 3. The results of this study are then used to select and characterize the element geometry of reflectarray antenna.

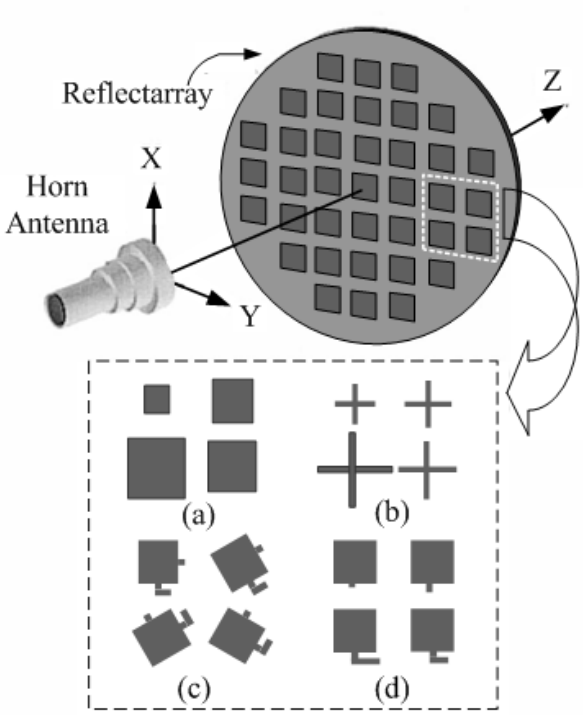

Figure 2.1 Configuration of a reflectarray antenna.

2.2 Reflectarray Concept

The reflectarray antenna consists of a flat or curved reflecting surface and an illuminating feed as shown in Figure 2.1. On the reflecting surface, there are many isolated elements (e.g., open-ended waveguides, printed patches, dipoles, or rings) without any power division transmission lines. The feed antenna illuminates these

isolated elements, which are designed to scatter the incident field with electrical phases that are required to form a planar phase front in the far-field distance. This operation is similar to the concept of a parabolic reflector with front feed that naturally reflects and forms a planar phase front when a feed is placed at its focal point. Thus, the term “flat reflector” is sometimes used to describe the reflectarray, which utilizes both technologies of reflector and array. As shown in Figure 2.1, there are several methods for reflectarray elements design to achieve a planar phase front. For example, one is to use identical microstrip patches with different-length phase-delay lines attached so that they can compensate for the phase delays over the different paths from the illuminating feed. The other is to use variable-size patches, dipoles, or rings so that elements can have different scattering impedances and, thus, different phases to compensate for the different feed-path delays. The third method, for circular polarization only, the reflectarray has all identical circularly polarized elements but with different angular rotations to compensate for the feed path length differences.

2.3 Literature Review of Development History

The reflectarray antenna concept was first demonstrated during the early 1960s (Berry, Malech, and Kennedy, 1963). Open-ended waveguide elements with variable-length waveguides were used to demonstrate the capability of achieving co-phasal re-radiated far-field beams. Since, during this early time, most wireless operations were done at relatively low microwave frequencies, the large-waveguide reflectarrays resulted in very bulky and heavy antennas. In addition, the efficiencies of these reflectarrays were not studied and optimized. More than ten years later (in the mid 1970s), the very clever concept of the “spiraphase” reflectarray was developed

(Phelan, 1977), in which switching diodes were used in an eight-arm spiral or dipole element of a circularly polarized reflectarray to electronically scan its main beam to large angles from the broadside direction. This is possible because, by angularly rotating a circularly polarized radiating element, its propagating electrical phase will also change by an amount proportion to the amount of rotation. However, due to the thick spiral cavity and large electronic components, the spiraphase reflectarray was still relatively bulky and heavy. Its aperture efficiency was still relatively poor. Thus, no continued development effort was followed. It should be noted here that, in order to have good efficiency for the reflectarray, the intricate relations among the element phasing, element beamwidth, element spacing, and focal length/diameter (*f/D*) ratio must be well designed; otherwise, a large backscattered component field or mismatched surface impedance would result.

Due to the introduction of the printable microstrip antennas, the technologies of reflectarray and microstrip radiators were combined. Various printed microstrip reflectarray antennas were developed in the late 1980s and early 1990s for the purpose of achieving reduced antenna size and mass. These printed reflectarrays came in various forms, but all have flat low-profile and low-mass reflecting surfaces. The reflectarrays that used identical patch elements with different-length phase delay lines (Munson et al., 1987; Huang, 1991; Metzler, 1992; Zhang et al., 1993; Javor et al., 1995; and Chang, 1995) have their elements similar to those illustrated in Figure 2.1(d). The phase delay lines, having lengths on the order of a half-wavelength long or less, are used to compensate for the phase differences of different path lengths from the illuminating feed. The second approach, shown in Figure 2.1(b), used elements that are made of printed dipoles with variable dipole lengths (Kelkar, 1991). Different

dipole lengths yield different scattering impedances, which then provide the different phases needed to compensate for the different path-length delays. Similarly, microstrip patches with variable patch sizes (Pozar and Metzler, 1993; Targonski and Pozar, 1994), shown in Figure 2.1(a), were also developed. Circularly polarized microstrip patches with identical size but vary angular rotations (Huang and Pogorzelski, 1998; and Huang, 1995), shown in Figure 2.1(c), were designed to form a co-phasal far-field reflectarray beam. In addition, several other reflectarrays or equivalent developments during the 1990s are worth mentioning here. Printed variable length dipole elements were used to form a frequency-scanned grating-reflector antenna with an offset feed (Johansson, 1990). Printed annular rings of variable diameters arranged in Fresnel zone configuration were also used to focus the beam (Gao and Barton, 1995). In the 1996 Phased Array Conference, a 94-GHz monolithic reflectarray (Colin, 1996), using a 1-bit p-type, intrinsic, n-type (PIN) diode phase shifters, was reported to achieve wide-angle (±45º) electronic beam scanning. In the same conference, a 35-GHz reflectarray, using waveguide/dielectric elements with 3-bit ferrite phase shifters (Tolkachev, Denisenko, Shishlov, and Shubov, 1996), was also reported to achieve ±25º beam scanning. One proposed technique (Huang, 1995), although not yet developed, is worth mentioning here. By using the angular rotation technique with circularly polarized elements, miniature or micro-machined motors could be placed under each element to achieve wide-angle beam scanning without the need of T/R modules and phase shifters. For application in the spacecraft area, a deployable and low-mass 1-meter diameter inflatable reflectarray antenna (Huang and Feria, 1999) at the X-band frequency was developed. Another unique spacecraft application of the reflectarray was conceived (Huang, 1996) and developed (Pozar,

Targonski, and Pokuls, 1999) by using its many elements, with a numerical phase synthesis technique, to form an uniquely shaped contour beam. From all the above developments, it can be seen that, at the beginning of the Twenty-First Century, the reflectarray antenna technology is becoming mature enough and has a variety of possible applications throughout the microwave and millimeter-wave spectra.

By early 2000, the reflectarray antennas were developed spaciously. Here, the several performance improvement techniques are worth mentioning. The first technique used multi-layer stacked patches to improve the reflectarray bandwidth from a few percent to more than ten percent (Encinar, 2001). As an extension to the 1-m X-band inflatable reflectarray mentioned above, a 3-m Ka-band inflatable reflectarray consisting of 200,000 elements was also developed (Huang, Feria, and Fang, 2001), which is currently known as the electrically largest reflectarray. An amplifying reflectarray was developed (Bialkowski, Robinson, and Song, 2002; Bialkowski and Song, 2002; Clark, Huff, and Bernhard, 2003) for each element of the reflectarray to amplify the transmitted signal and, thus, achieving very high overall radiated power. Spatial power combining techniques are presented (Arpin, Shaker, and McNamara, 2004) to offer an attractive means for achieving high-directivity antennas. In order to achieve good antenna efficiency, the most critical segment of the reflectarray design is the characteristics of elements. The element performance was optimized by using the genetic algorithm technique (Zich, Mussetta, Tovaglieri, Pirinoli, and Orefice, 2002; Kurup, Himdi, and Rydberg, 2003) and an iterative projection method (Costanzo, Venneri, Di Massa, and Angiulli, 2005). The reflectarray using a subreflector and array feed configuration to achieve fine beam scanning was also studied (Khayatian, and Rahmat-Samii, 2003; Chaharmir, Shaker,

Cuhaci, and Sebak, 2003). To combat the shortcoming of narrow bandwidth, dual-band multi-layer reflectarrays using variable patch size (Encinar and Zornoza, 2003; Shaker and Cuhac, 2005; Ginn, Lail, and Boreman, 2007), annular rings (Han and Chang, 2003; Han, Strassner, Chang, and Huang, 2003; Misran, Cahill, and Fusco, 2003; Han, Rodenbeck, Huang, and Chang, 2004; Strassner, Han, and Chang, 2004) and crossed dipoles (Zawadzki and Huang, 2003) are also being developed. Another development, which is worth mentioning here, is a folded reflectarray configuration (Pilz and Menzel, 1998; Menzel, Pilz, and Al-Tikriti, 2002; Lebererand and Menzel, 2005), where two reflecting surfaces are used to reduce the overall antenna profile due to the feed height of a conventional reflectarray. Others methods are used to set the phase shift introduced by the reflective element into the reflected wave such as half-wave dipoles or spiral elements (Martynyuk, Lopez, and Martynyuk, 2004), proximity-coupled (Chang and Wei, 2004), QUAD-EMC element (Chang and Suchen, 2005), varactor diode-tuned elements (Hum, Okoniewski, and Davies, 2005), and double cross loops (Chaharmir, Shaker, and Cuhaci, 2006).

2.4 Advantages/Disadvantages of Microstrip Reflectarrays

To achieve a low-reflecting surface profile and low antenna mass, reflectarrays using printed microstrip elements have been developed. These reflectarrays combine some of the best features of the traditional parabolic reflector antenna and the microstrip-array technology together. As with the parabolic reflector, the reflectarray can achieve very good efficiency (>50 percent) for very large aperture since no power divider is needed and thus very little resistive insertion loss is encountered here. On the other hand, very similar to an array antenna, the reflectarray can have its main

beam designed to tilt at a large angle (>50º) from its broadside direction. Low-loss electronic phase shifters can be implanted into the elements for wide-angle electronic beam scanning. With this beam scanning capability of the reflectarray, the complicated high-loss beamforming network and high-cost transmit/receive (T/R) amplifier modules of a conventional phased array are no longer needed. One significant advantage of the printed reflectarray is that, when a large aperture (e.g., 10-m size) spacecraft antenna requires a deployment mechanism, the flat structure of the reflectarray allows a much simpler and more reliable folding or inflation mechanism than the curved surface of a parabolic reflector. The flat reflecting surface of the reflectarray also lends itself to flush mounting onto an existing flat structure without adding significant mass and volume to the overall system structure. The reflectarray, being in the form of a printed microstrip antenna, can be fabricated with a simple and low-cost etching process, especially, when produced in large quantities. Another major feature of the reflectarray is that, with hundreds or thousands of elements in a reflectarray having phase adjustment capability, the array can achieve very accurate contour beam shape with a phase synthesis technique. With all the above capabilities, there is one distinct disadvantage associated with the reflectarray antenna. That is its inherent narrow bandwidth, which generally cannot exceed much beyond ten percentages. Although the reflectarray has narrow bandwidth, due to its multitude of capabilities, the development, research, and application of the printed reflectarray antenna would be boundless in the future.

The applications of large antennas with flat surfaces bring the following advantages to their design and deployment:

1. No shaping requirements: main reflector flatness greatly eases the

manufacturing shaping requirement, which is generally needed to achieve high gain.

2. Light weight materials: reflector surfaces can be made of lightweight materials, which can subsequently lower the deployment expenses of such antennas for many spacecraft applications.

3. Compact size: many newly fabricated materials are designed to bring an element of compactness to the design of large antennas before being fully launched. Moreover, the compact antenna is more easily transported by spacecraft before their deployment. This compactness allows the reflector/antenna structure to be rolled or folded before it is fully deployed in outer space.

2.5 Reflected Wave and Phase Delay of the Reflectarray Antenna

2.5.1 Reflected Wave of Front-Fed Parabolic Reflector

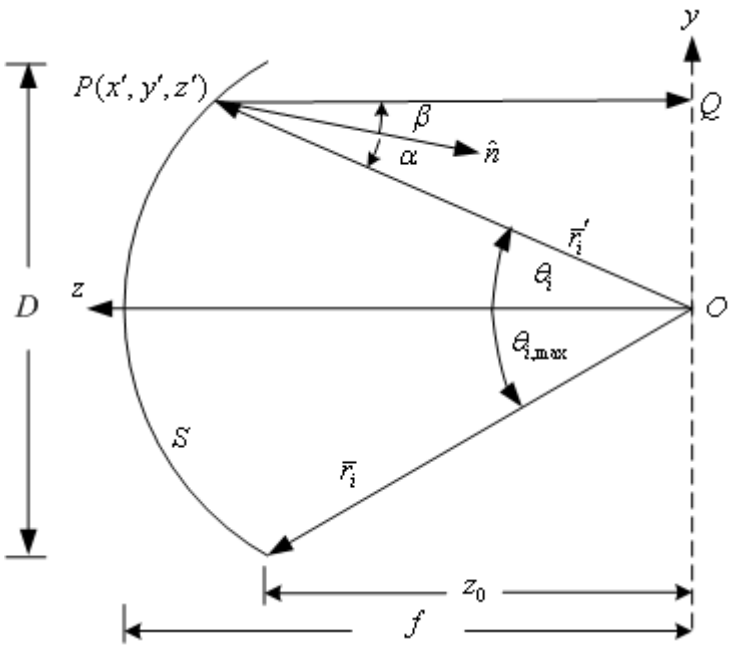

Figure 2.2 Two-dimensional configuration of a front-fed parabolic reflector.

As a high-gain aperture antenna, the front-fed parabolic reflector has widely been used. Figure 2.2 shows two-dimensional configuration of a front-feed parabolic reflector that rays emanating from the focal point of the reflector are transformed into plane waves. For any angle θ_0, the total length of the incident wave from the focus to a line perpendicular to the axis of the parabola and intercepting at the focal point, is a constant equal to 2*f* given by Equation (2.1), where *f* is the focal distance. This is also known as the equal phase front condition.

$$OP + PQ = \text{constant} = 2f \tag{2.1}$$

The expression that is usually very prominent in the analysis of reflector is that relating the subtended angle $\theta_{i,\max}$ to the *f*/*D* ratio.

$$\begin{aligned} \theta_{i,\max} &= \tan^{-1}\left(\frac{D/2}{z_0}\right) \\ &= 2\tan^{-1}\left(\frac{D}{4f}\right), \end{aligned} \tag{2.2}$$

where *D* is aperture dimension and $\theta_{i,\max}$ is the maximum angle between the vertical axis and the reflected ray, respectively.

2.5.2 Reflected Wave of Microstrip Reflectarray

Referring to the properties of a parabolic reflector, we recall that the process of focusing requires that the microwaves be reflected towards the focal point and that they arrive at the focus in phase. In a parabola, the reflection criteria is met by Snell's law, while a reflectarray, such criteria will be achieved by steering the array to the desired angle (i.e. along the steering angle during transmission, and towards the

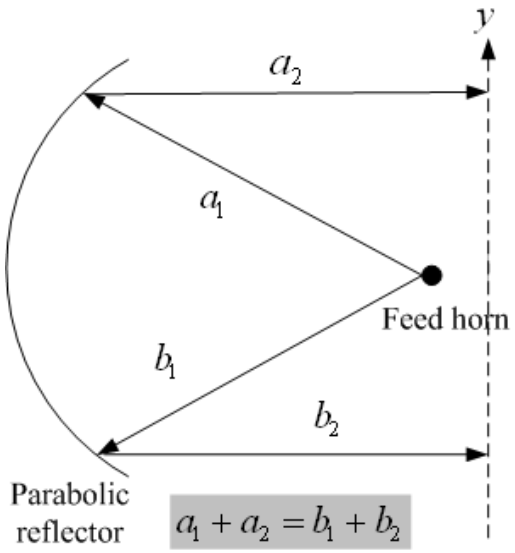

(a) Parabolic reflector

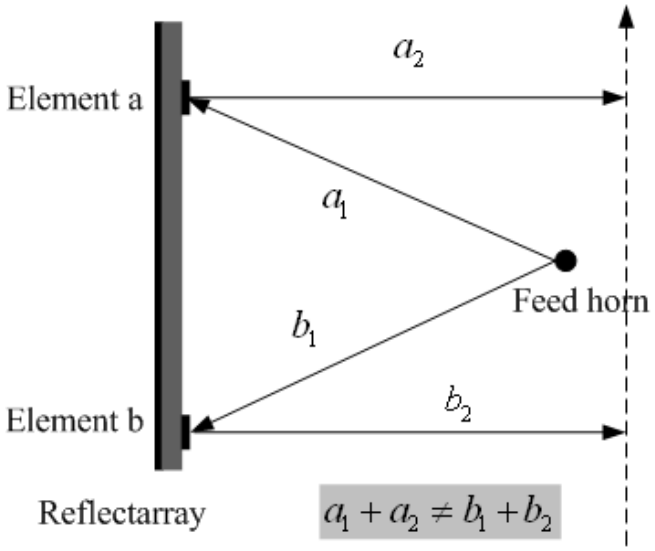

(b) Reflectarray

Figure 2.3 Reflected wave of reflector antenna.

focus during reception). The proper phasing criteria in a parabolic reflector is easily achieved because for any point on the parabola, the total length traveled by the wave from the focus to a line perpendicular to the axis of the parabola and intercepting at

the focal point, is a constant equal to 2*f*. In a reflectarray, as shown in Figure 2.3, this condition is not met since the distance from feed to any element, is dependant on the location of each element on the array.

In order to produce a plane wavefront from a source producing a spherical wavefront, it is necessary to introduce appropriate phase compensation across the spherical wavefront. For a parabolic reflector, this was achieved by using the intrinsic phasing properties of a curved parabolic dish. In a reflectarray antenna, the objective is to construct a planar antenna array that is capable of scattering an incident wavefront with suitable phasing superimposed such that a planar wavefront is collimated along some predetermined direction. In this way, the normal parabolic dish antenna can be replaced by a flat reflector or by a conformal surface.

2.5.3 Phase Delay of Microstrip Reflectarray

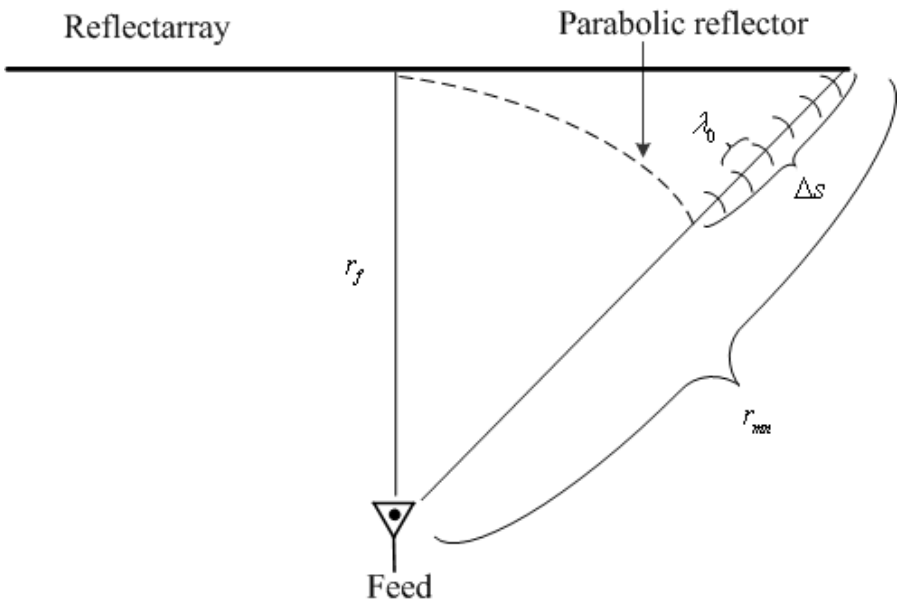

Figure 2.4 Spatial phase delay of the reflectarray.

The basic principle underpinning the operation of a reflectarray is the means by which to make the constituent elements of the array scatter the incident signal with the appropriate phases necessary for plane wave formation. Link the parabolic dish reflector, the basic design philosophy for a reflectarray requires that the total phase delay from the feed to a fix aperture plane is constant for all elements. The differential spatial phase delay can be best explained by referring to Figure 2.4, where the differential spatial phase delay, Δs, is the difference between the electrical paths r_f and r_{mn}. This Δs can be many multiples of the wavelength at the center operating frequency, such as $\Delta s = Nd\lambda_0$, where *N* is an integer and *d* represents the fractional number of a free-space wavelength λ_0. At each patch location on the reflectarray, *Nd* could be different numbers. In order to achieve constant aperture phase for the reradiated waves, the *d* at each patch location is compensated for by the appropriate patch size. However, as frequency changes, the *Nd* will change accordingly. Since the dimensions of patch are fixed, then a frequency excursion error will occur in the reradiated phase front. The old $Nd\lambda_0$ now becomes $Nd(\lambda_0 + \Delta\lambda_0)$, where $\Delta\lambda_0$ is directly proportion to the frequency change. The amount of phase change is, therefore, $Nd\Delta\lambda_0$, which can be a significant portion of a wavelength (360º). To reduce the amount of frequency excursion error, the integer number *N* must be reduced. There are two ways to reduce *N*. One is to design the reflectarray with a larger *f/D* ratio, and the other is simply to use a reflectarray with a small electrical diameter. With a fixed *f/D* ratio, the larger the electrical diameter, the larger the *N* will be (Pozar, Targonski, and Pokuls, 1999).

One can easily see that waves from the point source located at a distance r_f from the origin will travel a longer distance to the reflecting elements located on the extremities of the array as expressed in Equation (2.3).

$$r_{mn} = \sqrt{r_f^2 + x_{mn}^2 + y_{mn}^2} \tag{2.3}$$

Consequently, a phase delay ($\Delta\Phi_{mn}$) must be applied to each element to ensure that the electrical distance from feed to any element remains constant. The equation governing the delay values is given by Equation (2.4) (Pozar, Targonski, and Syrigos, 1997), and by implementing this value at each of the reflectarray elements, one can produce a plane wave just like parabolic reflectors or an array antennas.

$$\Delta\Phi_{mn} = k_0\left(r_{mn} - r_f\right) \pm 2\pi N, \tag{2.4}$$

where N is an integer and k_0 is wavenumber, respectively.

It should be noted that the implementation of the above phase shift at each element will yield a broadside transmission. Moreover, application of the array theory can be used to produce, for example, a beam along a desired direction by using Equation (2.5).

$$\Delta\Phi_{mn} = k_0\left[r_{mn} + \bar{r}_i \cdot \hat{r}_0\right] \pm 2\pi N \tag{2.5}$$

and

$$\bar{r}_i \cdot \hat{r}_0 = ms_x \sin\theta\cos\phi + ns_y \sin\theta\sin\phi\,, \tag{2.6}$$

where s_x and s_y are the element spacing in x and y directions, respectively.

Finally, another characteristic that describes a reflectarray is the subtended angle $\theta_{i,\max}$.

$$\theta_{i,\max} = \tan^{-1}\left(\frac{D}{2f}\right) \tag{2.7}$$

2.5.4 Phase Delay of Microstrip Reflectarray Using Backscattering Technique

Because of the use of the backscattering technique, the design of the shaped reflector antenna must satisfy the Snell's law for a reflecting surface that angle of incidence is equal to angle of reflection with respect to the normal vector (Smulders et al., 2001). To achieve broad-beamwidth for earth-matched beam reflectarray antenna, phase of each array element is specific designed to emulate the curvature of the backscatter. Figure 2.5 illustrates the incidence of wave on the surface of an analysis model of printed microstrip reflectarray using backscattering technique. Application of Snell's law of reflection for the reflector leads to the following differential equation:

$$\frac{dy_r}{dx_r} = \tan\left(\frac{1}{2}\theta_i - \frac{1}{2}\theta_r\right) \tag{2.8}$$

and

$$\theta_{r,\max} = \tan^{-1}\left(\frac{D_c - D}{2h}\right). \tag{2.9}$$

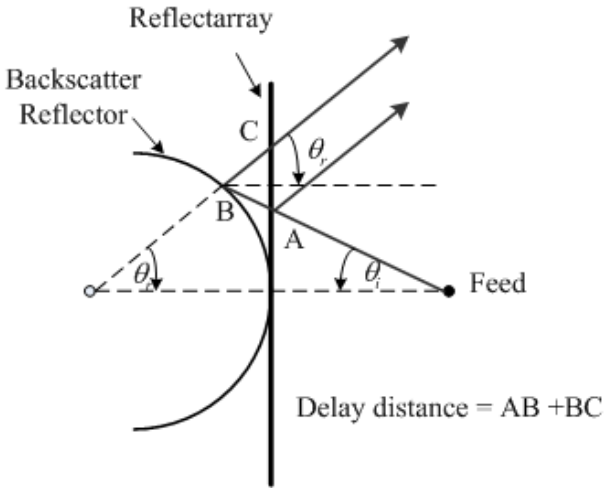

(a)

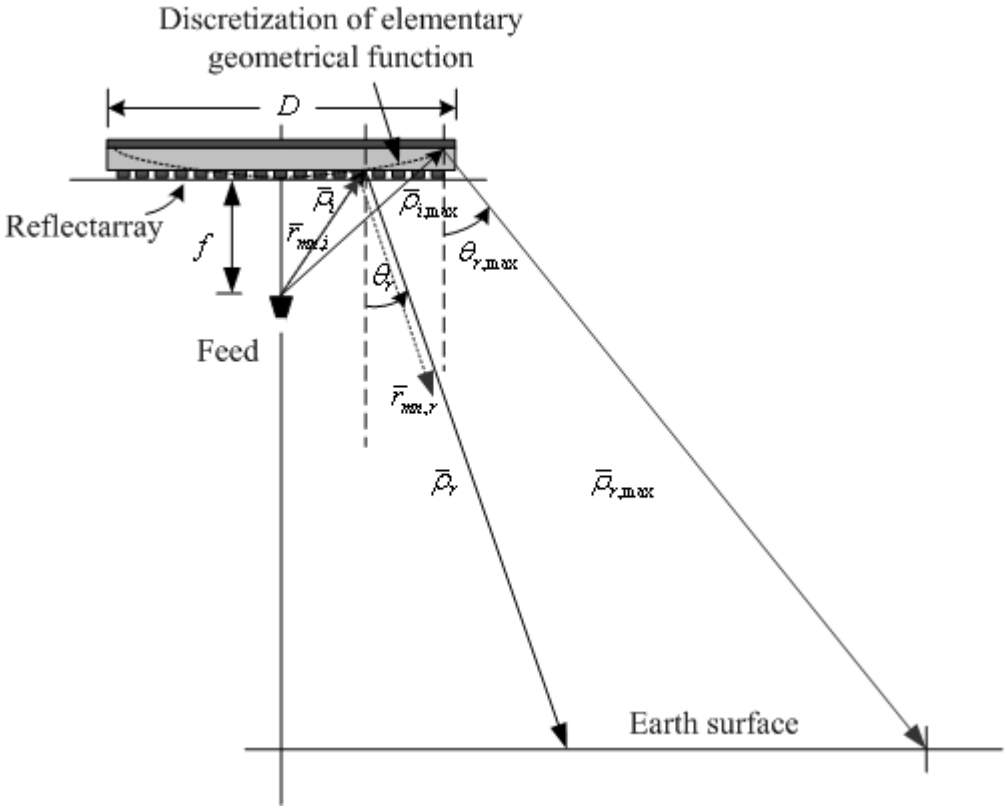

(b)

Figure 2.5 Reflectarray antenna by using backscattering technique.

The basic design principle requires that the phase $\Delta\Phi_{mn}$ of the field reflected from an element in the reflectarray using backscattering technique be chosen so the total phase delay from the feed to a fixed aperture plane in front of the reflectarray is difference for all elements.

$$\begin{aligned}\Delta\Phi_{mn} &= k_0\left(AB+BC\right)\pm 2\pi N \\ &= k_0\left(\rho_i+\rho_r-r_{mn}\right)\pm 2\pi N,\end{aligned} \tag{2.10}$$

where $\bar{\rho}_i$ and $\bar{\rho}_r$ are defined in Figure 2.5.

2.6 Analysis of an Infinite Array of Uniform Microstrip Elements

2.6.1 Incident and Reflected Fields

Figure 2.6 depicts the geometry of an infinite planar array of uniform elements printed on a single layer dielectric substrate of thickness d, with scalar permittivity $\varepsilon_r\varepsilon_0$ and permeability μ_0. The permittivity may be complex to account for losses in the dielectric. In order to determine the solution used to design and analyze a microstrip reflectarray, we assume an incident plane wave with an electric field of the form

$$\bar{E}^i = \bar{E}_0 e^{-jk_0\hat{r}_i\cdot\bar{R}} \tag{2.11}$$

where the complex vector $\bar{E}_0$ defines the amplitude and direction of the incident field. When a uniform plane wave is incident on a microstrip surface, the behavior of the reflected wave depends on the polarization of the incident wave. In order to be specific about the direction of the incidence electric field $\bar{E}^i$, we define a plane of

incidence as the plane containing the vector indicating the direction of propagation of the incident wave and normal to the boundary surface. Since the polarization of $\bar{E}_0$ in an arbitrary direction can always be decomposed into two components, one perpendicular and the other parallel to the plane of incidence as given by

$$\bar{E}_0 = \hat{a}_\theta^i E_{0\theta} + \hat{a}_\phi^i E_{0\phi}, \tag{2.12}$$

with

$$\begin{aligned} \hat{a}_\theta^i &= \hat{a}_x \cos\theta_i \cos\phi_i + \hat{a}_y \cos\theta_i \sin\phi_i - \hat{a}_z \sin\theta_i \\ \hat{a}_\phi^i &= \hat{a}_x \sin\phi_i - \hat{a}_y \cos\phi_i. \end{aligned} \tag{2.13}$$

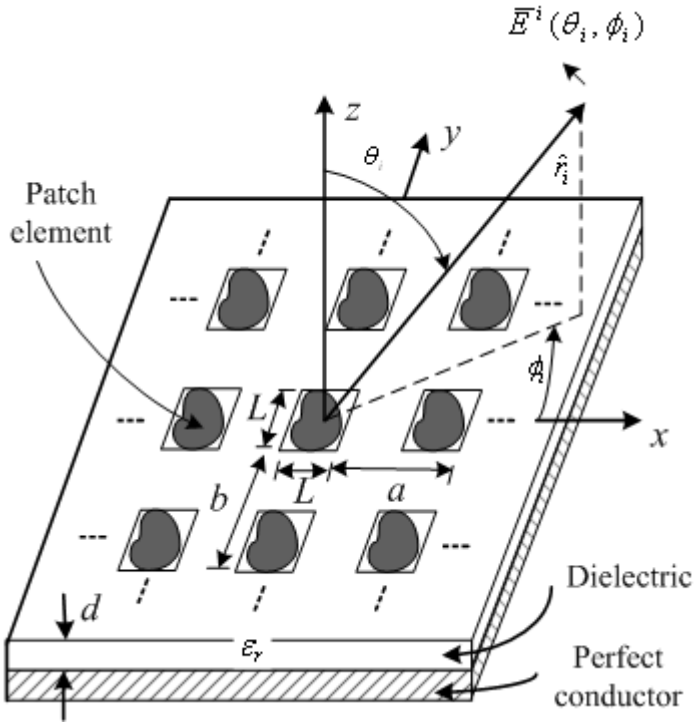

Figure 2.6 Microstrip reflectarray.

Where $\bar{R}$ is a position vector locating an arbitrary observation point,

$$\bar{R} = \hat{a}_x x + \hat{a}_y y + \hat{a}_y z\,, \tag{2.14}$$

k_0 is wave number of free space, and $\hat{r}_i$ is a unit vector of incident propagation

$$\hat{r}_i = -\hat{a}_x u_i - \hat{a}_y v_i - \hat{a}_z w_i\,, \tag{2.15}$$

and

$$\begin{aligned} u_i &= \sin\theta_i \cos\phi_i \\ v_i &= \sin\theta_i \sin\phi_i \\ w_i &= \cos\theta_i . \end{aligned} \tag{2.16}$$

With these results one can readily rewrite $\bar{E}^i$ as

$$\bar{E}^i = \bar{E}_0 e^{jk_0(xu_i + yv_i + z\cos\theta_i)}\,. \tag{2.17}$$

The phase reference for this incident field and the following fields are at the bottom of substrate. In the absence of array elements, the total electric field in the region $z \geq 0$ will be the sum of the incident field and field which is reflected from the grounded dielectric slab,

$$\bar{E}^T = \bar{E}^i + \bar{E}^r\,. \tag{2.18}$$

The reflected field produced by the grounded dielectric slab can be expressed as

$$\bar{E}^r = \bar{\bar{R}} \cdot \bar{E}_0 e^{jk_0(xu_i + yv_i - z\cos\theta_i)}\,, \tag{2.19}$$

where $\bar{\bar{R}}$ is the grounded dielectric slab's dyadic reflection coefficient

$$\bar{\bar{R}} = R_{\theta\theta}\hat{a}_\theta^r\hat{a}_\theta^i + R_{\phi\phi}\hat{a}_\phi^r\hat{a}_\phi^i, \tag{2.20}$$

with

$$\begin{aligned}\hat{a}_\theta^r &= \hat{a}_x\cos\theta_i\cos\phi_i + \hat{a}_y\cos\theta_i\sin\phi_i + \hat{a}_z\sin\theta_i \\ \hat{a}_\phi^r &= \hat{a}_x\sin\phi_i - \hat{a}_y\cos\phi_i.\end{aligned} \tag{2.21}$$

The presence of the elements gives rise to additional scattered field components. The resulting field induces a surface current on the perfectly conducting strip and this surface current $\bar{J}^S$, radiates in the presence of the grounded dielectric slab to produce a scattered electric field $\bar{E}^s$. The total electric field is given by

$$\bar{E}^T = \bar{E}^i + \bar{E}^r + \bar{E}^s. \tag{2.22}$$

The scattered fields in reflection coefficient form can be expressed as

$$\bar{E}^s = \bar{\bar{S}}\cdot\bar{E}_0 e^{jk_0(xu_i + yv_i - z\cos\theta_i)}, \tag{2.23}$$

where $\bar{\bar{S}}$ is the element's dyadic reflection coefficient.

$$\bar{\bar{S}} = S_{\theta\theta}\hat{a}_\theta^r\hat{a}_\theta^i + S_{\phi\theta}\hat{a}_\phi^r\hat{a}_\theta^i + S_{\theta\phi}\hat{a}_\theta^r\hat{a}_\phi^i + S_{\phi\phi}\hat{a}_\phi^r\hat{a}_\phi^i. \tag{2.24}$$

With the above result, the field in the reflection direction is a summation of the field reflected from the ground dielectric slab and the field scattered by surface elements. As depicted in Figure 2.6, we can be written total reflected field

as

$$\bar{E}^r_{tot} = \bar{E}^r + \bar{E}^s = \bar{\bar{R}}^{tot} \cdot \bar{E}_0 e^{jk_0(xu_i + yv_i - z\cos\theta_i)}, \tag{2.25}$$

where the total dyadic reflection coefficient is

$$\bar{\bar{R}}^{tot} = \bar{\bar{R}} + \bar{\bar{S}}. \tag{2.26}$$

Next, sections 2.6.2-2.6.8 will present the determination of the ground dielectric slab' and array elements' dyadic scattering coefficients, $\bar{\bar{R}}$ and $\bar{\bar{S}}$, respectively. The last section, Section 2.6.9, considers the total dyadic reflection coefficient of an infinite planar array (elements plus ground dielectric slab' contribution).

2.6.2 Grounded Dielectric Slab's Dyadic Reflection Coefficient

In order to determine the grounded dielectric slab's dyadic reflection coefficient, $\bar{\bar{R}}$, we will consider the incident plane wave at angle (θ_i, ϕ_i) in the (x, y, z) coordinate system that is transformed under the coordinate rotations shown in Figure 2.7 to

$$\bar{E}^i(x', y', z') = \bar{E}_0 e^{jk_0(x'u_i' - z'\cos\theta_i)} \tag{2.27}$$

where $u_i' = \sin\theta_i$.

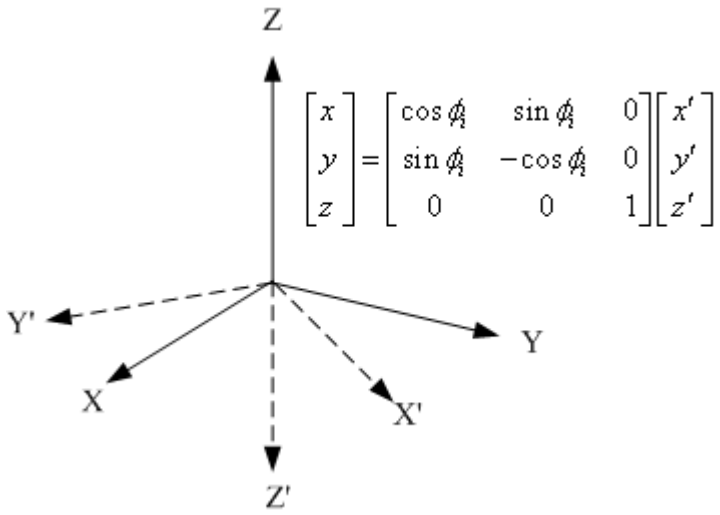

Figure 2.7 The coordinate transformation used to evaluate incident and reflected fields on a ground dielectric slab.

The transformation from the (x, y, z) coordinate system to the (x', y', z') coordinate system is achieved by rotating the original coordinate system through an angle ϕ_i, about the *z*-axis followed by a 180º rotation about the x' axis to reverse the *z*-axis direction. As shown, this transformation aligns the x' axis with the plane defined by the wave vector and the *z*-axis. Under this transformation, a projection of either a TM to *z*- or TE to *z*-polarized incident wave onto the plane of the dielectric yields a single vector component. As a result a simple transmission line analogy may be used to evaluate reflected and total fields on a grounded dielectric slab in the absence of the patch radiators.

As depicted in Figure 2.8, separated reflection coefficients may be calculated for TM to *z*-polarized waves ($\hat{a}_\theta$-polarization) and TE to *z*-polarized waves ($\hat{a}_\phi$-polarization) with

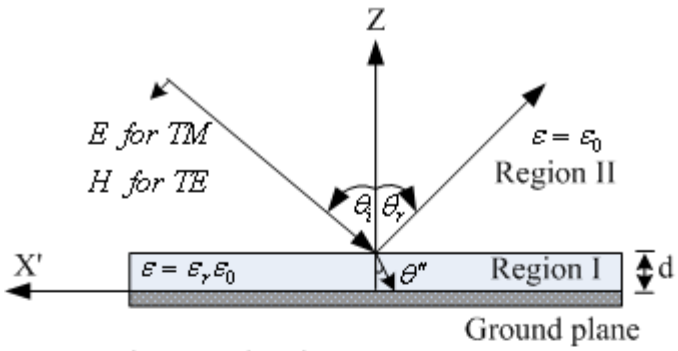

Equivalent circuit

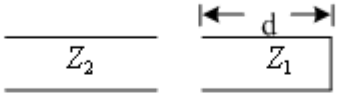

TM reflection coefficient

$$\Gamma^{TM} = \frac{Z_L - Z_2}{Z_L + Z_2},$$

where

$$Z_L = jZ_1 \tan(k_1 d)$$

$$Z_2 = \eta_2 \cos(\theta_i) = \eta_0 \cos(\theta_i)$$

$$Z_1 = \eta_1 \cos(\theta'') = \frac{\eta_0}{\varepsilon_r}\sqrt{\varepsilon_r - \sin^2(\theta_i)} = \frac{\eta_0}{\varepsilon_r} s$$

$$k_1 = k_0\sqrt{\varepsilon_r}\cos(\theta'') = k_0\sqrt{\varepsilon_r - \sin^2(\theta_i)} = k_0 s$$

TE reflection coefficient

$$\Gamma^{TE} = \frac{Z_L - Z_2}{Z_L + Z_2},$$

where

$$Z_L = jZ_1 \tan(k_1 d)$$

$$Z_2 = \eta_2 \sec(\theta_i) = \eta_0 \sec(\theta_i)$$

$$Z_1 = \eta_1 \cos(\theta'') = \frac{\eta_0}{\sqrt{\varepsilon_r - \sin^2(\theta_i)}} = \frac{\eta_0}{s}$$

$$k_1 = k_0\sqrt{\varepsilon_r}\cos(\theta'') = k_0\sqrt{\varepsilon_r - \sin^2(\theta_i)} = k_0 s$$

Figure 2.8 Transmission line equivalent circuits for plane wave incident on ground dielectric slab.

$$\Gamma^{TM} = \frac{js\tan(k_0 sd) - \varepsilon_r \cos(\theta_i)}{js\tan(k_0 sd) + \varepsilon_r \cos(\theta_i)}, \tag{2.28}$$

and

$$\Gamma^{TE} = \frac{js\tan(k_0 sd) - s\sec(\theta_i)}{js\tan(k_0 sd) + s\sec(\theta_i)}, \tag{2.29}$$

where

$$s = \sqrt{\varepsilon_r - \sin^2(\theta_i)}\,. \tag{2.30}$$

In the primed coordinate system, the tangential reflected field at the dielectric/air interface is given by

$$\bar{E}^r_{\tan}(x', y', -d) = \Gamma^{TM} E_{0\theta} e^{jk_0(x'\sin\theta_i + d\cos\theta_i)}(\hat{a}_\theta \cdot \hat{a}_{x'})\hat{a}_{x'}, \tag{2.31}$$

for a TM incident field and given by

$$\bar{E}^r_{\tan}(x', y', -d) = \Gamma^{TE} E_{0\phi} e^{jk_0(x'\sin\theta_i + d\cos\theta_i)}(\hat{a}_\phi \cdot \hat{a}_{y'})\hat{a}_{y'}, \tag{2.32}$$

for a TE incident field.

Transformation back to the unprimed coordinate system permits the tangential reflected field at $z = d$ to be described in component form as

$$\begin{aligned}\begin{bmatrix}\bar{E}_x^r(x,y,d)\\ \bar{E}_y^r(x,y,d)\end{bmatrix} &= \begin{bmatrix}\cos\phi_i & \sin\phi_i\\ \sin\phi_i & -\cos\phi_i\end{bmatrix}\begin{bmatrix}\bar{E}_{x'}^r(x',y',-d)\\ \bar{E}_{y'}^r(x',y',-d)\end{bmatrix}\\ &= \begin{bmatrix}\cos\phi_i & \sin\phi_i\\ \sin\phi_i & -\cos\phi_i\end{bmatrix}\begin{bmatrix}\Gamma^{TM}\cos\theta_i & 0\\ 0 & -\Gamma^{TE}\end{bmatrix}\begin{bmatrix}\bar{E}^i\cdot\hat{a}_\theta\\ \bar{E}^i\cdot\hat{a}_\phi\end{bmatrix},\end{aligned} \tag{2.33}$$

where the evaluation of $\bar{E}^i\cdot\hat{a}_\theta$ at $z=d$ for a yield TM incident field would

$$\bar{E}^i\cdot\hat{a}_\theta = \hat{a}_\theta^i E_{0\theta} e^{jk_0(xu_i+yv_i+d\cos\theta_i)}. \tag{2.34}$$

Similarly, the total tangential electric field, $\bar{E}^i_{\tan}+\bar{E}^r_{\tan}$, at $z=d$ is given by

$$\begin{bmatrix}\bar{E}_x^i+\bar{E}_x^r\\ \bar{E}_y^i+\bar{E}_y^r\end{bmatrix} = \begin{bmatrix}\cos\phi_i & \sin\phi_i\\ \sin\phi_i & -\cos\phi_i\end{bmatrix}\begin{bmatrix}(1+\Gamma^{TM})\cos\theta_i & 0\\ 0 & -(1+\Gamma^{TE})\end{bmatrix}\begin{bmatrix}\bar{E}^i\cdot\hat{a}_\theta\\ \bar{E}^i\cdot\hat{a}_\phi\end{bmatrix}. \tag{2.35}$$

The derivation of the reflected fields from grounded dielectric slab follows from the discussion of reflected fields. However, interest now focuses on the total θ- and ϕ-polarized fields not only the tangential components. The tangential field at the air/dielectric interface has been derived and is given by Equation (2.35). By enforcing $\nabla\cdot E=0$, the normal component of the reflected field can be determined in term of the tangential components as

$$E_z^r = \frac{\sin\theta_i\cos\phi_i E_x^r + \sin\theta_i\sin\phi_i E_y^r}{\cos\theta_i}. \tag{2.36}$$

Once cartesian components of the reflected field are determined the θ- and ϕ-components that follow from

$$E_\theta^r = E_x^r \cos\theta_r \cos\phi_r + E_y^r \cos\theta_r \sin\phi_r - E_z^r \sin\theta_r$$
$$E_\phi^r = -E_x^r \sin\phi_r + E_y^r \cos\phi_r \tag{2.37}$$

with the reflected and incident angles related by

$$\theta_r = \theta_i$$
$$\phi_r = \phi_i + \pi. \tag{2.38}$$

The reflection coefficient defined as the ratio of reflected field to incident field at $z = 0$ that follows from Equations 2.33, 2.36 and 2.37 as

$$R_{\theta\theta} = -\Gamma^{TM} e^{j2k_0 d\cos\theta_i} = \frac{k_0\varepsilon_r \cos\theta_i \cos k_1 d - jk_1 \sin k_1 d}{k_0\varepsilon_r \cos\theta_i \cos k_1 d + jk_1 \sin k_1 d} e^{2jk_0 d\cos\theta_i}$$
$$R_{\phi\phi} = \Gamma^{TE} e^{j2k_0 d\cos\theta_i} = \frac{k_1 \cos k_1 d - jk_1 \cos\theta_i \sin k_1 d}{k_1 \cos k_1 d + jk_1 \cos\theta_i \sin k_1 d} e^{2jk_0 d\cos\theta_i}. \tag{2.39}$$

In matrix form, the reflected field due to $\hat{q}$ polarized incident field is given by

$$\begin{bmatrix} \bar{E}_\theta^r \\ \bar{E}_\phi^r \end{bmatrix} = \begin{bmatrix} R_{\theta\theta} & 0 \\ 0 & R_{\phi\phi} \end{bmatrix} \begin{bmatrix} \hat{a}_\theta \cdot \hat{q} \\ \hat{a}_\phi \cdot \hat{q} \end{bmatrix} e^{jk_0(u_i x + v_i y - z\cos\theta_i)}. \tag{2.40}$$

2.6.3 Element's Dyadic Scattering Coefficient

In order to determine the array elements' dyadic reflection coefficients, $\bar{\bar{S}}$, a four-step procedure is followed:

1. Electric field integral equation (EFIE) formulation: An integral equation that yields the current density on the surface of the array elements' is formulated using boundary conditions (i.e. the tangential electric field must be zero on the array element surface).

2. Determination of the spectral electric-field Green's function: The field produced inside a dielectric structure, by an infinitesimal dipole arbitrarily placed on substrate, is derived in two-dimensional spectral domain form.

3. Determination of the periodic spatial electric-field Green's function: The result of the second step is generalized to the case of an infinite periodic array of infinitesimal dipoles, and then inverted into the spatial domain in closed form using Poisson's sum formula.

4. Full-wave Method of Moments solution of the EFIE: This method is applied to determine the current density on the surface of the conducting array elements. From this current, the scattering coefficient of the infinite array are obtained.

2.6.4 Electric Field Integral Equation (EFIE) Formulation

The electric field integral equation (EFIE) for the surface currents induced on the microstrip element by an incident plane wave is derived as follows. The scattered field in both the dielectric and air regions must be a solution to the wave equation

$$\nabla \times \nabla \times \bar{E} - k^2 \bar{E} = -j\omega\mu\bar{J}\,, \tag{2.41}$$

where

$$\begin{aligned} k &= k_0 = \omega\sqrt{\varepsilon_0\mu_0} \qquad \textit{for} \quad z > d \\ k &= \sqrt{\varepsilon_r}k_0 = \omega\sqrt{\varepsilon_r\varepsilon_0\mu_0} \quad \textit{for} \quad 0 \le z \le d. \end{aligned} \tag{2.42}$$

It can be shown (Collin,1990) that the solution to Equation (2.41) can be formulated in

terms of a Green's function as

$$\begin{aligned}\bar{E}(x,y,z) = &\iiint_{V_0} \bar{\bar{G}}(x,y,z/x_0,y_0,z_0)\cdot\bar{J}(x_0,y_0,z_0)dV_0 \\ &+\iint_{S_0}\left[(\hat{n}\times\nabla_0\times\bar{E})\cdot\bar{\bar{G}}+(\hat{n}\times\bar{E})\cdot\nabla_0\times\bar{\bar{G}}\right]dS_0,\end{aligned} \tag{2.43}$$

where $\bar{\bar{G}}$ is a dyadic Green's function which in the notation of (Itoh, 1989) is

$$\bar{\bar{G}} = \sum_{i=x,y,z}\sum_{j=x,y,z} \hat{i}G_{ij}\hat{j} \ . \tag{2.44}$$

The element G_{xy} represents the *x*-directed electric field due to a *y*-directed infinitesimal electric dipole.

Over a boundary defined by the plane $z = 0$ and the upper hemisphere at infinity, the surface integral term will vanish. If one assumes small but finite losses in both air and dielectric regions, the electric field on the upper hemisphere at infinity will be zero. Therefore, over this region, both terms in the surface integral are zero. At the plane $z = 0$, the tangential electric fields are zero and therefore the contribution of the second term in the surface integral is zero. One need now only insure that $\bar{\bar{G}}$ is zero when evaluated along the ground plane to insure zero contribution from the surface integral.

Equation (2.43) can now be tailored to the problem of finding the electric field due to surface current, $\bar{J}^S$, along the plane $z = d$.

$$\begin{aligned}\bar{E}(x,y,z) &= \iiint_{V_0} \bar{\bar{G}}(x,y,z/x_0,y_0,z_0)\cdot \bar{J}(x_0,y_0,z_0)dV_0 \\ &= \iint_{S_0} \bar{\bar{G}}(x,y,d/x_0,y_0)\ \cdot \bar{J}^S(x_0,y_0)dx_0dy_0\end{aligned} \tag{2.45}$$

Because the Green's function satisfies all the boundary conditions of the grounded dielectric slab, it follows that $\bar{E}^s$ as derived from Equation (2.45) fulfills all the boundary conditions of the grounded dielectric slab. Also, the total tangential electric field over the surface of the patch must be zero,

$$\bar{E}^i_{\tan} + \bar{E}^r_{\tan} = -\bar{E}^s_{\tan} = -\iint_{S_0} \bar{\bar{G}}(x,y,d/x_0,y_0)\ \cdot \bar{J}^S(x_0,y_0)dx_0dy_0, \tag{2.46}$$

where the integration is over the surface of the patch. It should be noted that only the G_{xx}, G_{xy}, G_{yx} and G_{yy} components are required. Equation (2.46) is the desired electric field integral equation for the unknown surface current $\bar{J}^S$. Equation (2.46) is solved numerically for the surface current $\bar{J}^S$, as discussed in the following sections.

The solution to Equation (2.46) is most concisely formulated in the Fourier Transform or spectral domain. The advantages of this approach are two fold. First, convolution in the spatial domain, as exemplified by Equation (2.46), is recast to multiplication in the spectral domain using the convolution theorem. Second, perhaps the most important factor, is that the associated Green's functions can be determined in the spectral domain and are generally algebraic expressions. The approach is to perform Fourier transformations along the major axes in a plane that perpendicular to the surface normal. This approach is appropriate for any infinite planar stratified media and has applications relevant to such diverse topics as the design of frequency

selective surfaces (Mittra, Chan, and Cwik, 1988), radio wave propagation above a lossy earth and microstrip circuit design (Itoh, 1989). We can define a Fourier Transform pair as follows

$$\begin{aligned}\tilde{A}(k_x,k_y,z) &= \int_{-\infty}^{\infty}\int_{-\infty}^{\infty} A(x,y,z)\ e^{-jk_x x}e^{-jk_y y}dxdy,\\ A(x,y,z) &= \frac{1}{4\pi^2}\int_{-\infty}^{\infty}\int_{-\infty}^{\infty} \tilde{A}(k_x,k_y,z)\ e^{jk_x x}e^{jk_y y}dk_x dk_y,\end{aligned} \tag{2.47}$$

which when applied to Equation (2.45) yields in component form

$$\tilde{E}^s(k_x,k_y,d) = \iint_{S_0} \bar{\bar{G}}(k_x,k_y,d/k_x,k_y)\ \cdot \tilde{J}^S(k_x,k_y)dk_x dk_y \tag{2.48}$$

or

$$\begin{bmatrix}\tilde{E}_x^s(k_x,k_y,d)\\ \tilde{E}_y^s(k_x,k_y,d)\end{bmatrix} = \begin{bmatrix}G_{xx}(k_x,k_y,d) & G_{xy}(k_x,k_y,d)\\ G_{yx}(k_x,k_y,d) & G_{yy}(k_x,k_y,d)\end{bmatrix}\begin{bmatrix}\tilde{J}_x^S(k_x,k_y)\\ \tilde{J}_y^S(k_x,k_y)\end{bmatrix}. \tag{2.49}$$

We can use Equation (2.49) to define the field obtained from several canonical surface current distributions, which is equivalent to defining the Green's function for those specified current distributions. For instance, a point source is given by

$$\bar{J}^S(x,y,z) = \delta(x-x_0)\delta(y-y_0)\delta(z-d)\,\hat{p}, \quad \text{where} \quad p = x \text{ or } y\,. \tag{2.50}$$

With Fourier transform using $\int f(x)\delta(x-a) = f(a)$, we can be expressed as

$$\tilde{J}^S(k_x, k_y, d) = e^{-jk_x x_0} e^{-jk_y y_0} \delta(z-d)\,\hat{p}. \tag{2.51}$$

Substitution of Equation (2.51) into (2.48) followed by inverse Fourier transformation yields

$$\bar{\bar{E}}^s(x, y, d / x_0, y_0) = \frac{1}{4\pi^2} \int_{-\infty}^{\infty} \int_{-\infty}^{\infty} \bar{\bar{G}}(k_x, k_y, d) e^{jk_x(x-x_0)} e^{jk_y(y-y_0)} dk_x dk_y . \tag{2.52}$$

This represents the scattered field at the point (x, y, d) from an infinitesimal current element at the point (x_0, y_0, d). Other canonical current distributions of interest include current sheets lying on the air/dielectric interface, for which the Fourier transformation is simply a Dirac delta function as well as infinite arrays of point sources. The later is central to the discussion of the scattering from an infinite array of microstrip elements and is subsequently derived. Now consider evaluating the electric field in the plane $z = d$ due to an arbitrary surface current distribution, $\bar{J}(x_0, y_0, d)$. This can be expressed as

$$\bar{E}^s(x, y, d) = \iint_{S_0} \bar{\bar{E}}^s(x, y, d / x_0, y_0) \cdot \bar{J}^S(x_0, y_0) dx_0 dy_0 , \tag{2.53}$$

which upon substitution of Equation (2.52) yields

$$\begin{aligned}\bar{E}^s(x,y,d) &= \frac{1}{4\pi^2}\int_{-\infty}^{\infty}\int_{-\infty}^{\infty}\bar{\bar{G}}(k_x,k_y,d)e^{jk_x x}e^{jk_y y}dk_x dk_y \\ &\cdot\iint_{S_0}\bar{J}^S(x_0,y_0)\,e^{-jk_x x_0}e^{-jk_y y_0}dx_0 dy_0 \\ &= \frac{1}{4\pi^2}\int_{-\infty}^{\infty}\int_{-\infty}^{\infty}\bar{\bar{G}}(k_x,k_y,d)\cdot\tilde{J}^S(k_x,k_y)e^{jk_x x}e^{jk_y y}dk_x dk_y.\end{aligned} \tag{2.54}$$

Applying a similar transformation to (2.46) yields

$$\bar{E}^i_{\tan}+\bar{E}^r_{\tan} = -\frac{1}{4\pi^2}\int_{-\infty}^{\infty}\int_{-\infty}^{\infty}\bar{\bar{G}}(k_x,k_y,d)\cdot\tilde{J}^S(k_x,k_y)e^{jk_x x}e^{jk_y y}dk_x dk_y, \tag{2.55}$$

which Equation (2.55) is the desired spectral domain representation of the electric field integral equation for the unknown surface current, $\bar{J}^S$.

2.6.5 Spectral Electric Field Dyadic Green's Function

The dyadic Green's function for the microstrip reflectarray is derived in the spectral domain with an infinitesimal electric current source on its surface. Considering the *y*-directed electric dipole as shown in Figure 2.9, we desire to find the E_x, E_y and E_z fields generated by this source. The magnetic vector potential in the regions I and II are solutions to the vector Helmholtz equations

$$\nabla^2\bar{A}^I+\varepsilon_r k_0^2\bar{A}^I=-\bar{J}, \tag{2.56}$$

$$\nabla^2\bar{A}^{II}+k_0^2\bar{A}^{II}=0, \tag{2.57}$$

where

$$\bar{J}=\delta(x-x_0)\delta(y-y_0)\delta(z-d)\hat{a}_y. \tag{2.58}$$

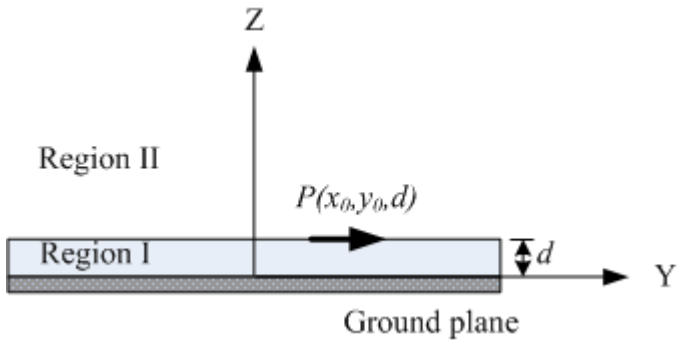

Figure 2.9 A *y*-directed infinitesimal current element on grounded dielectric slab.

A solution to Equations (2.56) and (2.57) requires both A_z and A_y components of the magnetic vector potential. Fourier transformation of $\bar{A}(x,y,z)$ to $\tilde{A}(k_x,k_y,z)$, as defined by Equation (2.47), recasts the partial differential Equations, (2.56) and (2.57), to ordinary differential equations given in region I by

$$\nabla^2 A_y^I + \varepsilon_r k_0^2 A_y^I = \frac{d^2 A_y^I}{dx^2} + \frac{d^2 A_y^I}{dy^2} + \frac{d^2 A_y^I}{dz^2} + \varepsilon_r k_0^2 A_y^I = -J\,, \tag{2.59}$$

$$\nabla^2 A_z^I + \varepsilon_r k_0^2 A_z^I = \frac{d^2 A_z^I}{dx^2} + \frac{d^2 A_z^I}{dy^2} + \frac{d^2 A_z^I}{dz^2} + \varepsilon_r k_0^2 A_z^I = 0\,, \tag{2.60}$$

or

$$\int_{-\infty}^{\infty}\int_{-\infty}^{\infty}\left[\frac{d^2\bar{A}_y^I}{dz^2}+\varepsilon_r k_0^2\bar{A}_y^I\right]e^{-jk_x x}e^{-jk_y y}dxdy=\int_{-\infty}^{\infty}\int_{-\infty}^{\infty}\bar{A}_y^I\frac{d^2e^{-jk_x x}}{dx^2}e^{-jk_y y}dxdy+\int_{-\infty}^{\infty}\int_{-\infty}^{\infty}\bar{A}_y^I e^{-jk_x x}\frac{d^2e^{-jk_y y}}{dy^2}dxdy$$
$$+\frac{d^2}{dz^2}\int_{-\infty}^{\infty}\int_{-\infty}^{\infty}\bar{A}_y^I e^{-jk_x x}e^{-jk_y y}dxdy+\int_{-\infty}^{\infty}\int_{-\infty}^{\infty}\varepsilon_r k_0^2\bar{A}_y^I\, e^{-jk_x x}e^{-jk_y y}dxdy$$
$$=\frac{d^2\tilde{A}_y^I}{dz^2}+(\varepsilon_r k_0^2-k_x^2-k_y^2)\tilde{A}_y^I$$
$$=\frac{d^2\tilde{A}_y^I}{dz^2}+k_1^2\tilde{A}_y^I,\tag{2.61}$$

and

$$\int_{-\infty}^{\infty}\int_{-\infty}^{\infty}\bar{J}\,e^{-jk_x x}e^{-jk_y y}dxdy=\int_{-\infty}^{\infty}\int_{-\infty}^{\infty}\left[\delta(x-x_0)\delta(y-y_0)\delta(z-d)\right]e^{-jk_x x}e^{-jk_y y}dxdy$$
$$=\left[\int_{-\infty}^{\infty}\int_{-\infty}^{\infty}\delta(x-x_0)\,e^{-jk_x x}e^{-jk_y y}dxdy\right]\tag{2.62}$$
$$\cdot\left[\int_{-\infty}^{\infty}\int_{-\infty}^{\infty}\delta(y-y_0)\,e^{-jk_x x}e^{-jk_y y}dxdy\right]\delta(z-d).$$
$$=\delta(z-d)e^{-jk_x x_0}e^{-jk_y y_0}$$

Thus, Equations (2.56) can be rewritten as

$$\frac{d^2\tilde{A}_y^I}{dz^2}+k_1^2\tilde{A}_y^I=\delta(z-d)e^{-jk_x x_0}e^{-jk_y y_0}\tag{2.63}$$

$$\frac{d^2\tilde{A}_z^I}{dz^2}+k_1^2\tilde{A}_z^I=0\,,\tag{2.64}$$

and in region II by

$$\frac{d^2\tilde{A}_y^{II}}{dz^2}+k_2^2\tilde{A}_y^{II}=0\tag{2.65}$$

$$\frac{d^2\tilde{A}_z^{II}}{dz^2} + k_2^2\tilde{A}_z^{II} = 0\,, \tag{2.66}$$

where

$$\begin{aligned} k_1^2 &= \varepsilon_r k_0^2 - k_x^2 - k_y^2 \\ k_2^2 &= k_0^2 - k_x^2 - k_y^2. \end{aligned} \tag{2.67}$$

General solutions to the ordinary differential equations (2.63) - (2.66) are given by

$$\tilde{A}_y^I = Ae^{jk_1 z} + Be^{-jk_1 z} \tag{2.68}$$

$$\tilde{A}_z^I = Ce^{jk_1 z} + De^{-jk_1 z} \tag{2.69}$$

$$\tilde{A}_y^{II} = Ee^{-jk_2 z} \tag{2.70}$$

$$\tilde{A}_z^{II} = Fe^{-jk_2 z}\,, \tag{2.71}$$

next, applying the boundary conditions

$$\bar{E}_{\tan}^I = 0 \qquad at \quad z = 0 \tag{2.72}$$

$$\bar{E}_{\tan}^I = \bar{E}_{\tan}^{II} \qquad at \quad z = d \tag{2.73}$$

$$\hat{n} \times (\bar{H}_{\tan}^{II} - \bar{H}_{\tan}^I) = \bar{J} \qquad at \quad z = d\,, \tag{2.74}$$

and using the relationships

$$E_x(x,y,z) = \frac{1}{j\omega\varepsilon}\left[\frac{d^2A_y}{dxdy} + \frac{d^2A_z}{dxdz}\right] \tag{2.75}$$

$$E_y(x,y,z) = -j\omega A_y + \frac{1}{j\omega\varepsilon}\left[\frac{d^2A_y}{dy^2} + \frac{d^2A_z}{dydz}\right] \tag{2.76}$$

$$E_z(x,y,z) = -j\omega A_z + \frac{1}{j\omega\varepsilon}\left[\frac{d^2A_y}{dydz} + \frac{d^2A_z}{dz^2}\right] \tag{2.77}$$

$$H_x(x,y,z) = \frac{dA_z}{dy} - \frac{dA_y}{dz} \tag{2.78}$$

$$H_y(x,y,z) = -\frac{dA_z}{dx} \tag{2.79}$$

$$H_z(x,y,z) = \frac{dA_y}{dx}. \tag{2.80}$$

For spectrum domain

$$\tilde{E}_x(k_x,k_y,z) = \frac{1}{j\omega\varepsilon}\left[-k_xk_y\tilde{A}_y + jk_x\frac{d\tilde{A}_z}{dz}\right] \tag{2.81}$$

$$\tilde{E}_y(k_x,k_y,z) = \frac{1}{j\omega\varepsilon}\left[(k^2-k_y^2)\tilde{A}_y + jk_y\frac{d\tilde{A}_z}{dz}\right] \tag{2.82}$$

$$\tilde{E}_z(k_x,k_y,z)=\frac{1}{j\omega\varepsilon}\left[\, jk_y\frac{d\tilde{A}_y}{dz}+(k^2+\frac{d^2}{dz^2})\tilde{A}_z \,\right] \tag{2.83}$$

$$\tilde{H}_x(x,y,z)=-jk_y\tilde{A}_z-\frac{d\tilde{A}_y}{dz} \tag{2.84}$$

$$\tilde{H}_y(x,y,z)=jk_x\tilde{A}_z \tag{2.85}$$

$$\tilde{H}_z(x,y,z)=-jk_x\tilde{A}_y\,, \tag{2.86}$$

allows the unknown coefficients A, B, C, D, F and H to be determined. In region I, $k=\sqrt{\varepsilon_r}k_0$, and in region II, $k=k_0$,. The solution for the magnetic vector potentials are

$$\tilde{A}_y^I(k_x,k_y,z)=\frac{\sin(k_1z)}{T_e}e^{-j(k_xx_0+k_yy_0)} \tag{2.87}$$

$$\tilde{A}_z^I(k_x,k_y,z)=\frac{k_y(\varepsilon_r-1)\sin(k_1d)}{T_eT_m}\cos(k_1z)e^{-j(k_xx_0+k_yy_0)} \tag{2.88}$$

$$\tilde{A}_y^{II}(k_x,k_y,z)=\frac{\sin(k_1d)}{T_e}e^{-jk_2(z-d)}e^{-j(k_xx_0+k_yy_0)} \tag{2.89}$$

$$\tilde{A}_z^{II}(k_x,k_y,z)=\frac{k_y(\varepsilon_r-1)\sin(k_1d)}{T_eT_m}\cos(k_1d)e^{-jk_2(z-d)}e^{-j(k_xx_0+k_yy_0)}\,, \tag{2.90}$$

where

$$\begin{aligned} T_e &= k_1 \cos(k_1 d) + jk_2 \sin(k_1 d) \\ T_m &= \varepsilon_r k_2 \cos(k_1 d) + jk_1 \sin(k_1 d). \end{aligned} \tag{2.100}$$

Substitution of Equations (2.87) and (2.88) into (2.81) and (2.82) followed by evaluation at $z = d$, yields the tangential components of the electric field due to an infinitesimal *y*-directed current element. This defines the spectral domain Green's function components G_{xy}, and G_{yy}, which are given by

$$\begin{aligned} \tilde{E}_x(k_x, k_y, z) &= -k_x k_y \frac{1}{j\omega\varepsilon} \frac{\sin(k_1 z)}{T_e} e^{-j(k_x x_0 + k_y y_0)} \\ &\quad + jk_x \frac{1}{j\omega\varepsilon} \frac{d\left[\dfrac{k_y(\varepsilon_r - 1)\sin(k_1 d)}{T_e T_m} \cos(k_1 z) e^{-j(k_x x_0 + k_y y_0)} \right]}{dz} \\ &= -k_x k_y \frac{1}{j\omega\varepsilon} \frac{\sin(k_1 z)}{T_e} e^{-j(k_x x_0 + k_y y_0)} \\ &\quad - jk_x k_1 \frac{1}{j\omega\varepsilon} \frac{k_y(\varepsilon_r - 1)\sin(k_1 d)}{T_e T_m} \sin(k_1 z) e^{-j(k_x x_0 + k_y y_0)}, \end{aligned} \tag{2.101}$$

also

$$\begin{aligned} G_{xy}(k_x, k_y, d) &= -k_x k_y \frac{1}{j\omega\varepsilon} \frac{\sin(k_1 d)}{T_e} e^{-j(k_x x_0 + k_y y_0)} \\ &\quad - jk_x k_1 \frac{1}{j\omega\varepsilon} \frac{k_y(\varepsilon_r - 1)\sin(k_1 d)}{T_e T_m} \sin(k_1 d) e^{-j(k_x x_0 + k_y y_0)} \\ &= \frac{1}{j\omega\varepsilon} \left[-k_x k_y \frac{T_m}{T_e T_m} - jk_x k_1 \frac{k_y(\varepsilon_r - 1)\sin(k_1 d)}{T_e T_m} \right] \\ &\quad \cdot \sin(k_1 d) e^{-j(k_x x_0 + k_y y_0)} \\ &= -\frac{1}{j\omega\varepsilon} \left[\frac{k_x k_y \varepsilon_r (k_2 \cos(k_1 d) + jk_1 \sin(k_1 d))}{T_e T_m} \right] \\ &\quad \cdot \sin(k_1 d) e^{-j(k_x x_0 + k_y y_0)}, \end{aligned} \tag{2.102}$$

and

$$\begin{aligned}\tilde{E}_y(k_x,k_y,z) &= (k^2-k_y^2)\frac{1}{j\omega\varepsilon}\frac{\sin(k_1 z)}{T_e}e^{-j(k_x x_0+k_y y_0)} \\ &\quad + jk_y\frac{1}{j\omega\varepsilon}\frac{d\left[\dfrac{k_y(\varepsilon_r-1)\sin(k_1 d)}{T_e T_m}\cos(k_1 z)e^{-j(k_x x_0+k_y y_0)}\right]}{dz} \\ &= \frac{1}{j\omega\varepsilon}(\varepsilon_r k_0{}^2-k_y^2)\frac{\sin(k_1 z)}{T_e}e^{-j(k_x x_0+k_y y_0)} \\ &\quad -\frac{1}{j\omega\varepsilon}jk_y k_1\frac{k_y(\varepsilon_r-1)\sin(k_1 d)}{T_e T_m}\sin(k_1 z)e^{-j(k_x x_0+k_y y_0)}\end{aligned} \tag{2.103}$$

then

$$\begin{aligned}G_{yy}(k_x,k_y,d) &= \frac{1}{j\omega\varepsilon}(\varepsilon_r k_0{}^2-k_y^2)\frac{\sin(k_1 d)}{T_e}e^{-j(k_x x_0+k_y y_0)} \\ &\quad -\frac{1}{j\omega\varepsilon}jk_y k_1\frac{k_y(\varepsilon_r-1)\sin(k_1 d)}{T_e T_m}\sin(k_1 d)e^{-j(k_x x_0+k_y y_0)} \\ &= \frac{1}{j\omega\varepsilon}\left[(\varepsilon_r k_0{}^2-k_y^2)\frac{T_m}{T_e T_m}-jk_y k_1\frac{k_y(\varepsilon_r-1)\sin(k_1 d)}{T_e T_m}\right]\sin(k_1 d)e^{-j(k_x x_0+k_y y_0)} \\ &= \frac{1}{j\omega\varepsilon}\left[\frac{(\varepsilon_r k_0{}^2-k_y^2)\varepsilon_r k_2\cos(k_1 d)+jk_1\varepsilon_r(k_0{}^2-k_y{}^2)\sin(k_1 d)}{T_e T_m}\right]\sin(k_1 d)e^{-j(k_x x_0+k_y y_0)}.\end{aligned} \tag{2.104}$$

Similarly, the spectral domain Green's function components for an x-directed infinitesimal dipole can be similarly found in terms of A_x, and A_z, vector potentials and are given by

$$\begin{aligned}G_{xx}(k_x,k_y,d) &= \frac{1}{j\omega\varepsilon}\left[\frac{(\varepsilon_r k_0{}^2-k_x^2)\varepsilon_r k_2\cos(k_1 d)+jk_1\varepsilon_r(k_0{}^2-k_x{}^2)\sin(k_1 d)}{T_e T_m}\right] \\ &\quad\cdot\sin(k_1 d)e^{-j(k_x x_0+k_y y_0)}\end{aligned} \tag{2.105}$$

and

$$G_{yx}(k_x, k_y, d) = G_{xy}(k_x, k_y, d)\,. \tag{2.106}$$

2.6.6 Periodic Spatial Electric Field Dyadic Green's Function

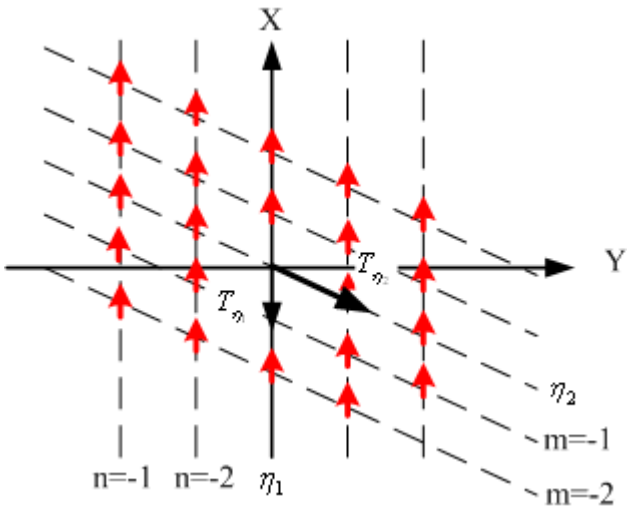

Figure 2.10 Geometry of the infinite array of infinitesimal dipoles.

Figure 2.10 shows the geometry of an infinite planar array of infinitesimal electric dipoles lying on a grounded dielectric slab. The dipoles are placed on the skewed coordinate system η_1, η_2, with periodicities T_{η_1}, and T_{η_2}, respectively. Consider a plane wave incident on the infinite array at an angle θ_i and ϕ_i as given by Equations (2.17). Clearly, due to the nature of the infinite periodic structure the currents induced on each dipole by the incident plane wave must have identical amplitudes with a progressive phase shift equivalent to that of the incident plane wave. In the (x,y) coordinate system, the induced currents in the array of Figure 2.10 may be expressed as

$$J_x^{\infty} = \sum_{m=-\infty}^{\infty} \delta(x - x') e^{jk_0 u_i x} \sum_{n=-\infty}^{\infty} \delta(y - y') e^{jk_0 v_i y}, \tag{2.107}$$

where

$$y' = nT_{\eta_2} \sin\alpha \tag{2.108}$$

$$\begin{aligned} x' &= mT_{\eta_1} + nT_{\eta_2} \cos\alpha \\ &= mT_{\eta_1} + \frac{y'}{\sin\alpha} \cos\alpha \\ &= mT_{\eta_1} + y' \cot\alpha \end{aligned} \tag{2.109}$$

then

$$J_x^{\infty} = \sum_{m=-\infty}^{\infty} \delta(x - y\cot\alpha - mT_{\eta_1}) e^{jk_0 u_i x} \sum_{n=-\infty}^{\infty} \delta(y - nT_{\eta_2} \sin\alpha) e^{jk_0 v_i y}. \tag{2.110}$$

Now consider the infinite array offset by (x_0, y_0) from the origin. The offset current distribution is expressed as the convolution

$$\begin{aligned} J_x^{\infty}(x,y) &= \delta(x - x_0)\delta(y - y_0) \\ &\quad * \left[\sum_{m=-\infty}^{m=\infty} \delta(x - y\cot\alpha - mT_{\eta_1}) e^{jk_0 u_i x} \sum_{n=-\infty}^{n=\infty} \delta(y - nT_{\eta_2} \sin\alpha) e^{jk_0 v_i y} \right]. \end{aligned} \tag{2.111}$$

Using the Fourier transform defined by Equation (2.47), the corresponding spectral domain expression for of the current element can be written as

$$\tilde{J}_x^{\infty}(k_x, k_y) = \frac{4\pi^2 e^{jk_x x_0} e^{jk_y y_0}}{T_{\eta_1} T_{\eta_2} \sin\alpha} \sum_{m=-\infty}^{m=\infty} \sum_{n=-\infty}^{n=\infty} \delta(k_x - k_x') \delta(k_y - k_y'), \tag{2.112}$$

where

$$k_x' = \frac{2\pi m}{T_{\eta_1}} + k_0 u_i \,, \tag{2.113}$$

$$k_y' = \frac{2\pi n}{T_{\eta_2} \sin\alpha} - \frac{2\pi m}{T_{\eta_1} \tan\alpha} + k_0 v_i \,. \tag{2.114}$$

The parameters u_i and v_i are the cosine directions of the incident plane wave with respect to the *x*- and *y*-axes as given by Equation (2.16). Substitution of Equation (2.112) for the *x*-directed infinite dipole array as well as a similar spectral representation for a *y*-directed array into Equation (2.48), followed by inverse Fourier transformation yields the dyadic representation

$$\bar{\bar{E}}^{\infty}(x, y, d / x_0, y_0) = \frac{1}{T_{\eta_1} T_{\eta_2} \sin\alpha} \sum_{m=-\infty}^{m=\infty} \sum_{n=-\infty}^{n=\infty} \bar{\bar{G}}(k_x', k_y') e^{jk_x'(x-x_0)} e^{jk_y'(y-y_0)} \,. \tag{2.115}$$

In the general case, the array will consist of an infinite set of two dimensional scattering elements as shown in Figure 2.11. The electric field due to induced currents on this array is found by convolving the infinite array Green's function as given by Equation (2 .115) with the surface current density on a single element, $\bar{J}_0(x_0, y_0)$.

$$\begin{aligned} \bar{E}^s(x, y, d) = \begin{bmatrix} \bar{E}_x \\ \bar{E}_y \end{bmatrix} &= \iint_{S_0} \bar{\bar{E}}^{\infty}(x, y, d / x_0, y_0) \cdot \bar{J}_0(x_0, y_0) dx_0 dy_0 \\ &= \frac{1}{T_{\eta_1} T_{\eta_2} \sin\alpha} \sum_{m=-\infty}^{m=\infty} \sum_{n=-\infty}^{n=\infty} \bar{\bar{G}}(k_x', k_y') \cdot \tilde{J}_0(k_x', k_y') e^{jk_x' x} e^{jk_y' y} \end{aligned} \tag{2.116}$$

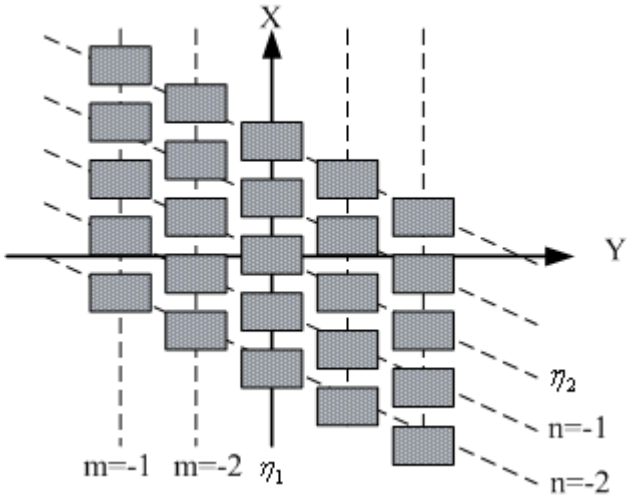

Figure 2.11 Infinite array of two dimensional scattering elements.

Here, the tangential electric field at the surface of the dielectric is expressed as a weighted summation of the discrete plane waves supported by the infinite periodic structure.

As in the single element case, by enforcing the condition that the total electric field on the surface of the scattering elements must be zero, an equation for the unknown current may be formulated. However, due to the replicative nature of the periodic Green's function, it is only necessary to enforce this condition over a single element or "unit cell " , i.e.;

$$\bar{E}^{i}_{\tan} + \bar{E}^{r}_{\tan} = -\frac{1}{T_{\eta_1} T_{\eta_2} \sin\alpha} \sum_{m=-\infty}^{m=\infty} \sum_{n=-\infty}^{n=\infty} \bar{\bar{G}}(k'_x, k'_y) \cdot \tilde{J}_0(k'_x, k'_y) e^{jk'_x x} e^{jk'_y y} \ . \qquad (2.117)$$

The fundamental unknown in Equation (2.117) is the surface current density on the unit cell, $\bar{J}_0(x, y)$.

2.6.7 Method of Moments Solution of the Electric Field Integral Equation

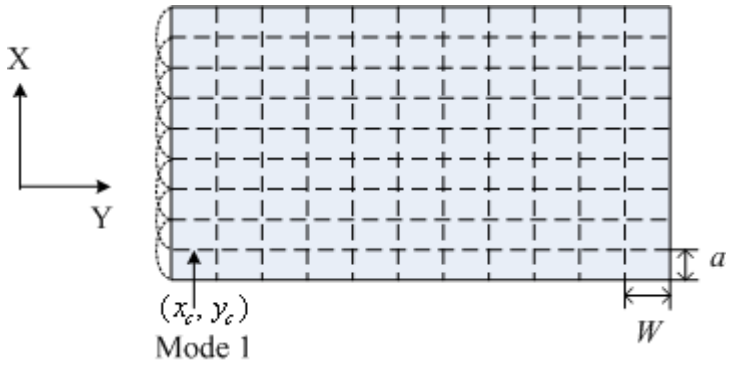

Figure 2.12 Rectangular tessellation of the conducting elements of an infinite microstrip array.

Figure 2.12 depicts a single zero thickness perfectly electric conducting element of an infinite array, tessellated into small rectangles of area $\Delta_x \Delta_y$. Since the periodic dyadic Green's function derived in the previous section already takes into account the fact that the elements form an infinite array, only a single element need to be considered here. The electric surface current density $\bar{J}_0(x, y)$ following on this element, can be described using two sets of basis functions T_j^x and T_j^y, one for each vector component, hence

$$\bar{J}_0(x, y) = \sum_{j=1}^{N_{J_x}} I_j^x T_j^x(x, y)\hat{a}_x + \sum_{j=1}^{N_{J_y}} I_j^y T_j^y(x, y)\hat{a}_y, \tag{2.118}$$

where I_j^x and I_j^y are unknown complex coefficients to be determined by the method of moment. N_{J_x} and N_{J_y} are the number of basis functions in the $\hat{x}$- and

$\hat{y}$-directions, respectively. In this thesis the overlapping piecewise sinusoidal basis functions as shown in Figure 2.12, have been selected to describe $\overline{J}_0(x,y)$.

Overlapping *x*- and *y*- directed piecewise sinusoidal (PWS) modes are used on the patch. Analytically *x*- and *y*- directed PWS mode are given by

$$T_j^x(x,y) = J_j^x(x)J_j^y(y) = \frac{\sin(k_{eff}(\Delta_x - |x-x_c|))}{\sin(k_{eff}\Delta_x)}\frac{1}{\Delta_y}\hat{a}_x, \quad for \quad |x-x_c| < \Delta_x, \; |y-y_c| < \frac{\Delta_y}{2}. \tag{2.119}$$

$$T_j^y(x,y) = J_j^y(x)J_j^y(y) = \frac{\sin(k_{eff}(\Delta_y - |y-y_c|))}{\sin(k_{eff}\Delta_y)}\frac{1}{\Delta_x}\hat{a}_y, \quad for \quad |x-x_c| < \frac{\Delta_x}{2}, \; |y-y_c| < \Delta_y, \tag{2.120}$$

where Equations (2.119) and (2.120) has been explicitly written to show the separability in *x* and *y*. As shown in Figure 2.12, the parameters x_c and y_c are the coordinates for the center of the PWS mode. k_{eff} is chosen be the wavenumber.

Using the Fourier transform, the corresponding spectral domain electric current density can be written as

$$\tilde{J}_0(k_x,k_y) = \sum_{j=1}^{N_{J_x}} I_j^x \tilde{T}_j^x(x,y)\hat{a}_x + \sum_{j=1}^{N_{J_y}} I_j^y \tilde{T}_j^y(x,y)\hat{a}_y, \tag{2.121}$$

with the spectral-domain basis function given by

$$\tilde{T}_j^x(k_x,k_y)=\tilde{J}_j^x(k_x)\tilde{J}_j^x(k_y), \tag{2.122}$$

$$\tilde{T}_j^y(k_x,k_y)=\tilde{J}_j^y(k_x)\tilde{J}_j^y(k_y), \tag{2.123}$$

where

$$\tilde{J}_j^x(k_x)=\frac{2k_{eff}(\cos(k_x\Delta_x)-\cos(k_{eff}\Delta_x))}{\sin(k_{eff}\Delta_x)(k_{eff}^2-k_x^2)}e^{-jk_xx_c}, \tag{2.124}$$

$$\tilde{J}_j^x(k_y)=\frac{\sin(k_y\frac{\Delta_y}{2})}{k_y\frac{\Delta_y}{2}}e^{-jk_yy_c}, \tag{2.125}$$

$$\tilde{J}_j^y(k_x)=\frac{\sin(k_x\frac{\Delta_x}{2})}{k_x\frac{\Delta_x}{2}}e^{-jk_xx_c}, \tag{2.126}$$

$$\tilde{J}_j^y(k_y)=\frac{2k_{eff}(\cos(k_y\Delta_y)-\cos(k_{eff}\Delta_y))}{\sin(k_{eff}\Delta_y)(k_{eff}^2-k_y^2)}e^{-jk_yy_c}. \tag{2.127}$$

For convenience in formulating the matrix equation, the electric current density and its spectral-domain image can be rewritten as

$$\overline{J}_0(x,y)=\sum_{j=1}^{N}I_j\overline{J}_j(x,y), \tag{2.128}$$

$$\tilde{J}_0(k_x,k_y)=\sum_{j=1}^{N}I_j\tilde{J}_j(k_x,k_y), \tag{2.129}$$

respectively, where

$$\left[\overline{J}_j, \tilde{J}_j, I_j\right] = \begin{cases} \left[\hat{a}_x \overline{T}_j^x, \hat{a}_x \tilde{T}_j^x, I_j^x\right] & \text{for } j \le N_{J_x} \\ \left[\hat{a}_y \overline{T}_{j-N_{J_x}}^y, \hat{a}_y \tilde{T}_{j-N_{J_x}}^y, I_{j-N_{J_x}}^y\right] & \text{for } j > N_{J_x} \end{cases}, \tag{2.130}$$

and N is the total number of basis functions, i.e.,

$$N = N_{J_x} + N_{J_y} \quad . \tag{2.131}$$

Substituting Equation (2.129) into the electric field integral equation, i.e., Equation (2.117), one obtains

$$\begin{aligned} \overline{E}_{\tan}^i + \overline{E}_{\tan}^r &= -\frac{1}{T_{\eta_1} T_{\eta_2} \sin\alpha} \sum_{j=1}^{N} I_j \left[\sum_{m=-\infty}^{m=\infty} \sum_{n=-\infty}^{n=\infty} \overline{\overline{G}}(k_x', k_y') \cdot \tilde{J}_j(k_x', k_y') e^{jk_x' x} e^{jk_y' y} \right] \\ &= -\frac{1}{T_{\eta_1} T_{\eta_2} \sin\alpha} \sum_{j=1}^{N} I_j L(\overline{J}_j). \end{aligned} \tag{2.132}$$

In this work, this equation is solved using Galerkin's method (Wang, 1991). In this method, the testing functions $\overline{w}_i$ are chosen as the complex conjugate $\overline{J}_i$. However, because $\overline{J}_i$ is real, the complex conjugate of $\overline{J}_i$ is itself. Multiplying then the above equation by the testing function $\overline{J}_i$, where i = 1, 2,..., N, and integrating over the element surface S yields the linear system of equations

$$\iint_S \overline{J}_i \cdot (\overline{E}_{\tan}^i + \overline{E}_{\tan}^r)\, dS = \sum_{j=1}^{N} I_j \left[-\frac{1}{T_{\eta_1} T_{\eta_2} \sin\alpha} \iint_S \overline{J}_i \cdot L(\overline{J}_j)\, dS \right]. \tag{2.133}$$

This system of equations can also be written as

$$V_i = \sum_{j=1}^{N} Z_{ij} I_j, \qquad \text{where} \quad i = 1, 2, 3, ..., N \tag{2.134}$$

or as

$$\begin{bmatrix} V_1 \\ \vdots \\ V_i \\ \vdots \\ V_N \end{bmatrix} = \begin{bmatrix} Z_{11} & \cdots & Z_{1j} & \cdots & Z_{1N} \\ \vdots & & \vdots & & \vdots \\ Z_{i1} & \cdots & Z_{ij} & \cdots & Z_{iN} \\ \vdots & & \vdots & & \vdots \\ Z_{N1} & \cdots & Z_{Nj} & \cdots & Z_{NN} \end{bmatrix} \begin{bmatrix} I_1 \\ \vdots \\ I_j \\ \vdots \\ I_N \end{bmatrix}, \tag{2.135}$$

where the Z_{ij} is the impedance element given by

$$Z_{ij} = -\frac{1}{T_{\eta_1} T_{\eta_2} \sin\alpha} \sum_{m=-\infty}^{m=\infty} \sum_{n=-\infty}^{n=\infty} \tilde{J}_i(k'_x, k'_y) \cdot \bar{\bar{G}}(k'_x, k'_y) \cdot \tilde{J}_j(k'_x, k'_y), \tag{2.136}$$

and V_i is the voltage element that can be expressed using the reciprocity theorem as

$$V_i = \int_x \int_y \bar{J}_i \cdot (\bar{E}^i + \bar{E}^r) dxdy = \int_x \int_y \bar{E}_i \cdot \bar{J}_s^e dxdy\,, \tag{2.137}$$

where $\bar{J}_i$ is the *i*th expansion mode current, $\bar{E}_i$ is the electric field radiated by that mode in the presence of the grounded dielectric substrate, and $\bar{J}_e^S$ is an equivalent surface current density that radiates the field $\bar{E}^i + \bar{E}^r$ in the absence of patches. It can be shown that one choice for this current is

$$\bar{J}_s^i(x,y)\big|_{z=0} = \bar{J}_{sx}^i(x,y)\big|_{z=0}\, \hat{a}_x + \bar{J}_{sy}^i(x,y)\big|_{z=0}\, \hat{a}_y = -2\hat{z} \times \bar{H}_i\big|_{z=0}. \tag{2.138}$$

Using Equations (2.12), (2.14) and (2.17), Equation. (2.138) can be rewritten, with $z = 0$, as

$$\bar{J}_s^e = \bar{J}_{s0} e^{jk_0(xu_i + yv_i)}, \tag{2.139}$$

where the complex vector $\bar{J}_{s0}$ is equal to

$$\begin{aligned} \bar{J}_{s0} = \frac{-2}{\eta_0} \Big[& \hat{a}_x (E_{0\theta} \cos\phi_i - E_{0\phi} \cos\theta_i \sin\phi_i) \\ & + \hat{a}_y (E_{0\theta} \sin\phi_i - E_{0\phi} \cos\theta_i \cos\phi_i) \Big] \end{aligned}. \tag{2.140}$$

Using this expression in Equation (2.137) results in delta functions from the space integrations, which allows the voltage vector elements to be simplified to

$$V_i = \bar{J}_{s0} \cdot \bar{\bar{G}}(-k_0 u_i, -k_0 v_i) \cdot \bar{J}_i(-k_0 u_i, -k_0 v_i) e^{jkd\cos\theta_i}. \tag{2.141}$$

With these impedance and voltage matrix elements, given by Equations (2.136) and (2.141), respectively, the unknown complex current coefficients I_j of Equation (2.129) can be determined by solving the linear system of equations given by Equation (2.135). The surface current density flowing in the array elements is then determined.

The surface current density determined by the above method is referred in the literature as a full-wave Method of Moments solution (Lee and Chen, 1997). In the next section this surface current density is used to determine the array elements' dyadic reflection coefficient, $\bar{\bar{S}}$.

2.6.8 Scattering Coefficients of Array

In order to calculate the array elements' dyadic reflection coefficients, first the unknown electric current complex coefficients I_j of Equation (2.129) must be determined according to the Method of Moments procedure detailed in the previous section. Once the electric surface current density $\bar{J}_0(x_0, y_0)$ of Equation (2.129) is known, its scattered field at z = 0 can be evaluated using Equation (2.116). Substituting $\bar{\bar{G}}$ and $\bar{J}_0(x_0, y_0)$, defined by Equation. (2.102), (2.104), (2.105), (2.106), and (2.129), respectively, into the above equation yields

$$\begin{aligned}\bar{E}^s(x,y,d) &= \begin{bmatrix} \bar{E}_x^s(x,y,d) \\ \bar{E}_y^s(x,y,d) \end{bmatrix} \\ &= \frac{1}{T_{\eta_1} T_{\eta_2} \sin\alpha} \sum_{m=-\infty}^{\infty} \sum_{n=-\infty}^{\infty} \bar{\bar{G}}(k_x', k_y') \tilde{J}_0(k_x', k_y') e^{jk_x' x} e^{jk_y' y},\end{aligned} \tag{2.142}$$

or

$$\bar{E}^s = \frac{1}{T_{\eta_1} T_{\eta_2} \sin\alpha} \sum_{j=1}^{N} \sum_{m=-\infty}^{m=\infty} \sum_{n=-\infty}^{n=\infty} e^{jk_x' x} e^{jk_y' y} \bar{\bar{G}}(k_x', k_y') \cdot \tilde{J}_j(k_x', k_y') I_j . \tag{2.143}$$

The fields above the dielectric can be expressed in terms of the fields at the surface of then dielectric as

$$E_x(x,y,z>d) = E_x(x,y,d) e^{-jk_z(z-d)}, \tag{2.144}$$

$$E_y(x,y,z>d) = E_y(x,y,d) e^{-jk_z(z-d)}, \tag{2.145}$$

$$E_z(x,y,z>d)=\frac{k'_x E_x(x,y,d)+k'_y E_y(x,y,d)}{k_z}e^{-jk_z(z-d)}, \tag{2.146}$$

with the dispersion relation

$$k_z=\sqrt{k_0^2-k_x'^2-k_y'^2}, \tag{2.147}$$

where

$$k'_x=\frac{2\pi m}{T_{\eta_1}}+k_0u_i, \tag{2.148}$$

$$k'_y=\frac{2\pi n}{T_{\eta_2}\sin\alpha}-\frac{2\pi m}{T_{\eta_1}\tan\alpha}+k_0v_i. \tag{2.149}$$

Although the reflected field at z = 0 is composed of an infinite number of Floquet modes, in a far-zone region only a few of them are propagating. These are the modes with a real wavenumber k_z. From the wavenumber k_z, given by Equation (2.144), all propagating modes must satisfy the condition

$$\frac{k_z}{k_0}=\sqrt{1-\left(\frac{k'_x}{k_0}\right)^2-\left(\frac{k'_y}{k_0}\right)^2}, \tag{2.150}$$

or

$$\left(\frac{k'_x}{k_0}\right)^2+\left(\frac{k'_y}{k_0}\right)^2<1. \tag{2.151}$$

Substituting the *x*- and *y*-wavenumbers, defined by Equations. (2.148) and (2.149), into the above equation, and recalling that $k_0 = 2\pi / \lambda_0$, one obtains

$$\left(\frac{m}{a/\lambda_0} + \sin\theta_i \cos\phi_i \right)^2 + \left(\frac{n}{b/\lambda_0} + \cos\theta_i \cos\phi_i \right)^2 < 1. \tag{2.152}$$

Since $\sin\theta_i$ is always less or equal to 1, this equation indicates that the fundamental mode (i.e., mode with $m = n = 0$), is always a propagating mode.

For proper operation, space-fed arrays should have only one propagating mode (i.e., $m = 0$ and $n = 0$) to avoid losing power in undesired directions. All other modes must be made evanescent. A condition that guarantees this can be obtained requiring Equation (2.152) be violated for any mode other than $m = n = 0$. Recalling that ϕ_i can be any angle, the lowest order modes $m = \pm 1$, $n = 0$ and $m = 0$, $n = \pm 1$ will not propagate if

$$\frac{1}{a/\lambda_0} - \sin\theta_i > 1, \tag{2.153}$$

$$\frac{1}{b/\lambda_0} - \sin\theta_i > 1, \tag{2.154}$$

Hence, no higher order modes will propagate if

$$\frac{a}{\lambda_0} < \frac{1}{1+\sin\theta_i}, \tag{2.155}$$

$$\frac{b}{\lambda_0} < \frac{1}{1+\sin\theta_i}. \tag{2.156}$$

Therefore, if the values of the grid spacings a/λ_0 and b/λ_0 are both less than $1/(1+\sin\theta_i)$, the only propagating mode is the one with *m* = *n* = 0. These last two conditions are identical to the grating-lobe condition of antenna arrays (Amitay, Galindo, and Wu, 1972). From now on it will be assumed that this condition is always satisfied. The reflected field at *z* = 0 is given by Equation (2.143), with *m* = *n* = 0, as

$$\begin{aligned}\bar{E}^s(x,y,d) &= \begin{bmatrix}\bar{E}_x^s(x,y,d)\\ \bar{E}_y^s(x,y,d)\end{bmatrix} = \begin{bmatrix}\bar{E}_x^q\\ \bar{E}_y^q\end{bmatrix} e^{jk_0u_ix}e^{jk_0v_iy} \\ &= \frac{1}{T_{\eta_1}T_{\eta_2}\sin\alpha}\overline{\overline{G}}(k_0u_i,k_0v_i)\cdot\bar{J}_0^q(k_0u_i,k_0v_i)e^{jk_0u_ix}e^{jk_0v_iy},\end{aligned} \tag{2.157}$$

where the superscript *q* refers to the polarization of the incident plane wave. That is $q=\theta$ or ϕ for TM or TE to *z*-incident plane waves respectively. This is a statement that the current is dependent on the incident wave polarization and separate current vectors $[I]$ must be calculated for TM or TE incident plane waves. Equation (2.157) can rewrite as

$$\bar{E}^s(x,y,d) = e^{jk_0u_ix}e^{jk_0v_iy}\frac{1}{T_{\eta_1}T_{\eta_2}\sin\alpha}\sum_{j=1}^{N}\overline{\overline{G}}(k_0u_i,k_0v_i)\cdot\bar{J}_j(k_0u_i,k_0v_i)I_j\ . \tag{2.158}$$

The closed form expressions for the far-field, $\bar{E}^s$, due to current $\bar{J}^S$ can be determined. The parameter usually used to characterize scattering by an arbitrary finite body is the radar cross section (RCS) defined as

$$S_{pq} = \frac{E_p^s(z=0)}{E_q^i(z=0)}. \tag{2.159}$$

In general, we choose the incident field to have unit magnitude and we are interested in the $\theta-$ or $\phi-$directed scattered field, i.e. $(p,q)=(\theta,\phi)$. Substitution of Equation (2.157) into Equations (2.144) and (2.145) yields the cartesian components of the scattered field from which the spherical components may be calculated following the same procedures outlined in section 2.6.2 for the reflected field. The result is

$$\begin{aligned} E_\theta^s &= -\left[\frac{\cos\phi_0 E_x^q + \sin\phi_0 E_y^q}{\cos\theta_0}\right] e^{jk_0(u_i x+v_i y)} e^{-jk_z(z-d)}, \\ E_\phi^s &= \left[\sin\phi_0 E_x^q - \cos\phi_0 E_y^q\right] e^{jk_0(u_i x+v_i y)} e^{-jk_z(z-d)}, \end{aligned} \tag{2.160}$$

which upon substitution into Equation (2.159) determines the scattering matrix elements;

$$\begin{aligned} S_{\theta q} &= \left[\frac{\cos\phi_0 E_x^q + \sin\phi_0 E_y^q}{\cos\theta_0}\right] e^{jk_z d}, \\ S_{\phi q} &= \left[\sin\phi_0 E_x^q - \cos\phi_0 E_y^q\right] e^{jk_z d}. \end{aligned} \tag{2.161}$$

For numerical consideration, the scattering coefficient is substituting Equation (2.17) into Equations (2.23) and (2.24), and then comparing the results with Equation (2.158) yields

$$\bar{\bar{S}} \cdot \bar{E}_0 = \frac{1}{T_{\eta_1} T_{\eta_2} \sin\alpha} \sum_{i=1}^{N} \bar{\bar{G}}(k_0 u_i, k_0 v_i) \cdot \tilde{J}_i(k_0 u_i, k_0 v_i) I_i \,. \tag{2.162}$$

Therefore, using Equation (2.162), the components of the array elements' dyadic reflection coefficients $S_{\theta\theta}$ and $S_{\phi\theta}$ can be obtained, when the incident field $\bar{E}_0$ is assumed equal to $\hat{a}_\theta^i$. Similarly, when $\bar{E}_0$ is assumed equal to $\hat{a}_\phi^i$, the components of the dyadic reflection coefficients $S_{\theta\phi}$ and $S_{\phi\phi}$ can be determined.

2.6.9 Total Scattering Coefficients

Now all the details are necessary for determining the total dyadic scattering coefficients $\bar{\bar{R}}^{tot}$, which is available that the ground dielectric slab' and array elements' dyadic scattering coefficients ($\bar{\bar{R}}$ and $\bar{\bar{S}}$) can be obtained using the results of section 2.6.2 and 2.6.8, respectively, and the total dyadic scattering coefficients $\bar{\bar{R}}^{tot}$ is determined by summing the ground dielectric slab' and the array elements' dyadic scattering coefficients as expressed in Equation. (2.26).

$$\bar{\bar{R}}^{tot} = R_{\theta\theta}^{tot}\hat{a}_{\theta}^{r}\hat{a}_{\theta}^{i} + R_{\phi\theta}^{tot}\hat{a}_{\phi}^{r}\hat{a}_{\theta}^{i} + R_{\theta\phi}^{tot}\hat{a}_{\theta}^{r}\hat{a}_{\phi}^{i} + R_{\phi\phi}^{tot}\hat{a}_{\phi}^{r}\hat{a}_{\phi}^{i} \tag{2.163}$$

Based on this procedure, a numerical tool for evaluating the total scattering coefficients $\bar{\bar{R}}^{tot}$ was implemented. Its simulation results and experimental validation is presented in the Chapters 3 and 4, respectively.

2.7 Chapter Summary

This chapter gives a more detailed discussion and literature surveys of up-to-date of the development history and key design methodologies for microstrip reflectarray antenna. In addition, this chapter presents a full wave moment method treatment of the field scattered by an infinite uniform array of conducting elements on a single layer dielectric substrate, and this tool will be used to generate the required element design data for implementing microstrip reflectarray. The effective and accurate step-by-step design methodology was developed for the broad-beam microstrip reflectarray considered. Using these tools, the reflectarray was designed, manufactured, and tested in following chapter.

CHAPTER III

DESIGN AND SIMULATION RESULTS

3.1 Introduction

As discussed in the previous chapter of this thesis, a reflectarray consists of an array of conducting elements etched on a flat dielectric substrate backed by a perfect conductor. Reflectarrays can offer a competitive alternative to reflectors in many narrow-band, pencil-beam, and shaped-beam antenna applications. While reflector antennas control electromagnetic radiation by changing the phase of the reflected wave through their surface shape, reflectarrays rely on etched patch elements of varying geometry to achieve the same goal. When compared to reflectors, the advantage of reflectarrays is their lower cost, as the patch elements can be produced using photolithography. However, reflectarrays have inherent bandwidth and loss limitations that are not present in reflectors.

Figure 3.1 shows a typical reflectarray geometry designed to produce collimated radiation, including its reflector and feed. The purpose of the reflectarray is to emulate the reflector, which has focal length f and dimension D. The feed, located at the focus, illuminates the reflectarray. Because the reflectarray surface is flat, it has to provide a phase correction to achieve the same collimation. For this the reflectarray uses an array of conducting elements of variable dimensions, etched on top of the metal-backed dielectric. By adjusting the dimensions of each element appropriately, the incident diverging field can then be transformed into a collimated reflected field.

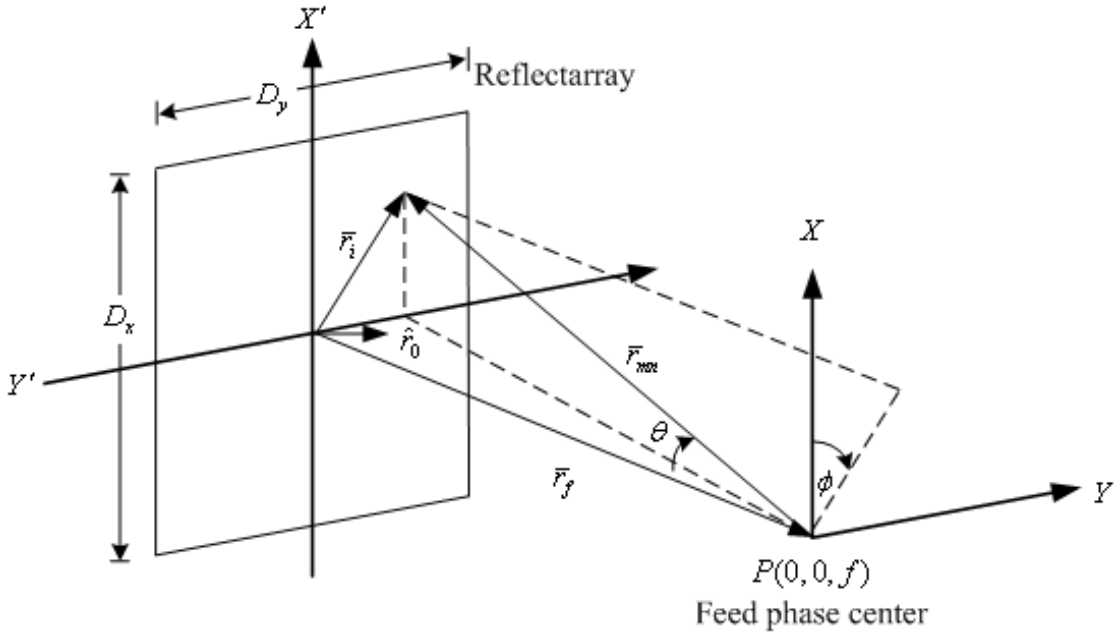

Figure 3.1 Reflectarray geometry.

This chapter first discusses a design procedure for a finite reflectarrays, then goes into the phase reflection characteristics of a few representative reflectarray elements, and finally concludes with a reflectarray element case study. Experimental verification of the design approach is presented in Chapter 4. More specifically, in Section 3.2, a reflectarray design procedure is presented. Since the purpose of the reflectarrays of interest in this work is to emulate a broad-beam reflector, the basic dimensioning procedure for their aperture, focal length, and feed are identical to the one followed as shown in Sections 3.3-3.5. Once the basic reflectarray dimensions are established, the required reflection coefficient phase of each element can be calculated (Section 3.6).

The design approach which is based on the infinite array analysis of scattering from a microstrip element as outlined in the previous chapter is discussed in Section

3.7. The numerical tools, which are developed in Chapter 2 by using MATLAB tool, are used to study a limited number of representative reflectarray element geometries. The results of this study lead to a microstrip patch element geometry with reduced sensitivity to etching errors. A comparison between the etching-error sensitivities of this proposed square patch element, and the commonly used cross dipole and square loop elements, is provided to demonstrate the advantage of the former element.

Section 3.8 presents the calculation of the radiation. An electrically small square-aperture ($N \times N$ elements) case-study reflectarray is designed and rigorously modeled to verify some of the design assumptions. A small array is used for this task to keep the computational task, associated with modeling the reflectarray rigorously, at a manageable level.

3.2 Design Procedure

Once appropriate element geometry has been selected to implement the reflectarray phase transformation, the microtrip reflectarray can be designed by using a step-by-step procedure. In this section all the relevant details of this procedure are presented; it basically consists of six steps:

1. Feed horn antenna: The radiation pattern of pyramidal horn antenna and the incident field of each reflectarray element are investigated. The parameters of the backscatter (i.e., diameter D and focal length f) are determined from the optimum incident field.

2. Shaped backscatter design: The shaped reflector in this thesis is designed by using discretization of elementary geometrical functions to form a wide beam antenna.

3. Grid spacing determination: The impact of the elements' grid spacing and

dimension on the reflected field can then be studied. Based on these results, optimum dimensions can be determined.

4. Determination of the unit cell required phase delay ($\Delta\Phi_{mn}$): Each unit cell must have an appropriate reflection coefficient phase $\angle\Gamma$ that will transform the incident spherical wave into a reflected plane wave. Using the shaped backscatter parameters, the required phase delay of each reflectarray element can be derived.

5. Determination of the element characterization: The reflection coefficient phase $\angle\Gamma$, which is induced on the array, has to compensate for phase delay between patch elements and surface of backscatter. Using the numerical tools developed in Chapter 2, an infinite array of uniform elements is simulated. Once the periodicity of the elements has been established, the corresponding reflection coefficient phase $\angle\Gamma$ versus trimming length curve is obtained. From this result, the dimensions of each reflectarray element can be established.

6. Rigorous small reflectarray simulation: To validate the antenna design produced in the previous items, an electrically small finite square aperture reflectarray is then designed. Using the numerical tools developed in Chapter 2, the radiated far-zone fields of this reflectarray are then rigorously simulated. This step is used to verify all design parameters. If any problem is found on the operation, the design parameters must be revisited by returning to the first step of the design procedure. Note that ideally one would like to simulate the actual (large) reflectarray. However, the capability of the available computers at present is insufficient to carry-out all, but sufficient for the smaller practical array.

3.3 Pyramidal Feed Horn Antenna

The pyramidal horn is a waveguide aperture antenna as shown in Figure 3.2. It has a phase curvature at the aperture due to the flared horn wall. The aperture fields and the internal fields in the flared region are separable in two rectangular coordinates. The radiation pattern of a pyramidal horn is given by (Balanis, 1997)

$$E_\theta = j\frac{k_0 E_0 e^{-jk_0 r}}{4\pi r}\sin\phi\left|F(\theta,\phi)\right| e^{j\psi(\theta,\phi)}, \tag{3.1}$$

$$E_\phi = j\frac{k_0 E_0 e^{-jk_0 r}}{4\pi r}\cos\phi\left|F(\theta,\phi)\right| e^{j\psi(\theta,\phi)}. \tag{3.2}$$

Closed form, but lengthy, expressions for the factors $\left|F(\theta,\phi)\right|$ and $\psi(\theta,\phi)$ are given in (Balanis, 1997) in terms of cosine and sine Fresnel integrals. The feed horn is designed to provide the optimum incident field illumination in terms of aperture efficiency and spillover loss.

Consider the reflectarray geometry illustrated in Figure 3.1. Here, an electromagnetic horn located along the z-axis at point $P(0,0,f)$ illuminates a microstrip reflectarray of dimensions $D_x \times D_y$. The E-plane of the feed horn lies in the *xz*-plane. In this thesis, the reflectarray of 30 cm dimension is designed and fed with a standard X-band pyramidal horn. The feed dimensions were chosen to obtain the theoretical E- and H-planes radiation patterns as shown in Figure 3.3. Also, the horn dimensions are $\rho_1 = \rho_2 = 2.3\lambda$ (6.9 cm), $a_1 = 1.5\lambda$ (4.5 cm), $b_1 = 1.6\lambda$ (4.8 cm), $a = 0.76\lambda$ (2.28 cm) and $b = 0.34\lambda$ (1.02 cm).

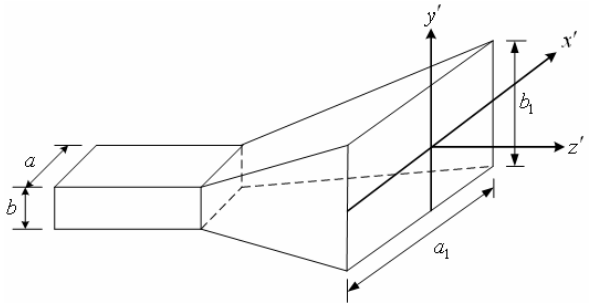

(a) Pyramidal horn

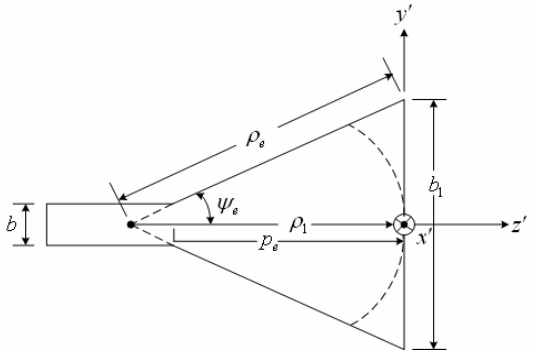

(b) E-plane view

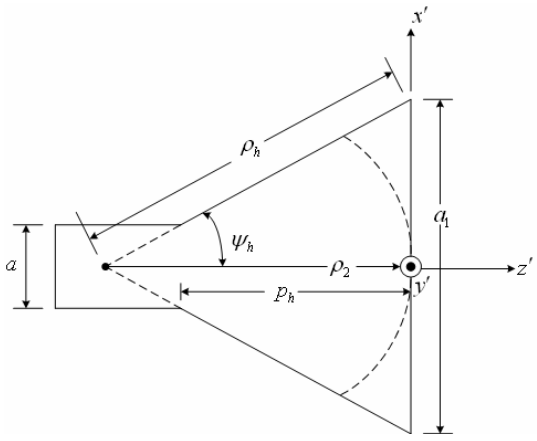

(c) H-plane view

Figure 3.2 Pyramidal horn and coordinate system.

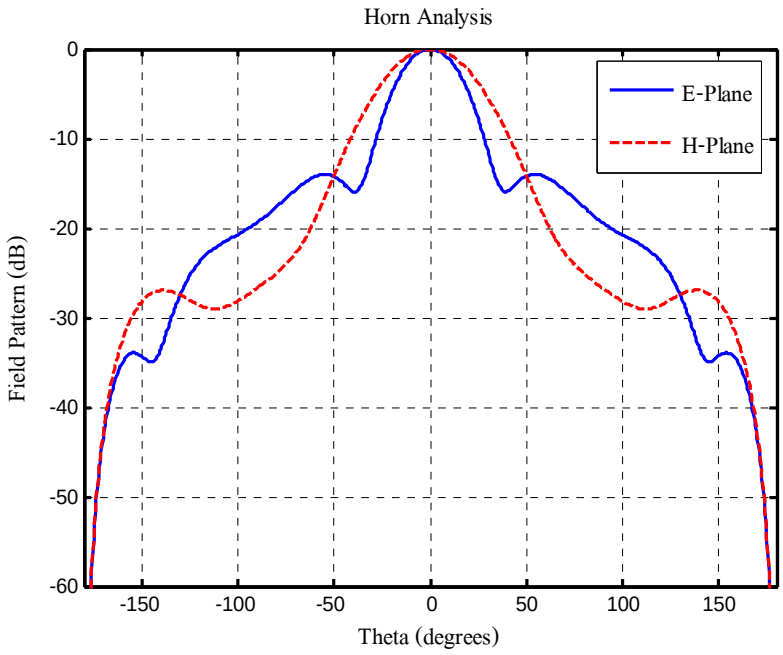

Figure 3.3 Radiation pattern of pyramidal feed horn.

The phase factor $\psi(\theta,\phi)$ is referenced to the horn aperture and can be made nearly independent of θ and ϕ by displacing the phase reference point. In other words, with respect to the new reference point that is called the phase center, the radiating field appears to be nearly a spherical wavefront. Due to the differences of curvature of the phase front in the E- and H-planes, the different phase centers exist for two principal planes. The E- and H-planes phase centers were determined from $\psi(\theta,\phi)$ and found to be displaced by 2.5 cm and 3.9 cm from the horn aperture toward the horn apex. A compromise position of 3.2 cm was selected and placed at the focal point of the reflectarray. The tangential incident field along the X' and Y' axes of the reflectarray can be shown to have only an X' electric field component. A significant cross polarized tangential component of the incident field occurs only along the diagonals $\phi = (45°, -45°)$ and for the *f/D* ratio of interest, the cross polarized

component is insignificant in comparison to the X' component. This permits the incident field at each element to be locally approximated by a TM-polarized plane wave with incidence angle $(\theta_i, \phi_i) = (0°, 0°)$.

Normalization of the incident field at element *i*th by the field at the center element yields

$$\overline{E}_i^i = \frac{\left|\overline{r}_f\right|}{\left|\overline{r}_i - \overline{r}_f\right|} \frac{F(\theta_i, \phi_i)}{F(\theta = 0, \phi = 0)} e^{-jk_0\left(\left|\overline{r}_i - \overline{r}_f\right| - \left|\overline{r}_f\right|\right)} \cdot \left[\cos\phi\, \hat{a}_\theta + \sin\phi\, \hat{a}_\phi\right], \tag{3.3}$$

where $\overline{r}_i$ is the element position vector and $\overline{r}_f$ is the feed phase center position vector as shown in Figure 3.1.

As shown in Figure 3.3, feed horn provides less energy at the edge of reflector than at the center. At starting reflectarray design, the antenna feed illuminates the reflector edge with -10 dB when compared with the illumination at the center of the reflector. The figure of -10 dB edge illumination may be considered as a compromise between the amount of spillover, on the one hand, and efficient illumination of the reflector surface on the other. Also, feed distance is chosen to be of 15 cm. Subsequently, the selection of the optimum feed distance to diameter ratio (*f/D*) for the reflectarray is a compromise between several performance factors. The advantage of a large ratio *f/D* is that a local area of the reflectarray surface sees the incident spherical wavefront as nearly planar and as a result plane wave approximations are valid locally within the array. In addition, a large ratio minimizes cross polarization of reflectarray. However, for larger *f/D* ratio, a larger primary feed aperture is required to reduce spillover loss and for extremely large *f/D* ratio, pattern distortions due to the feed aperture blockage are unacceptable. In contrast, a small *f/D* mitigates aperture

blockage, but introduces aperture matching problems associated with the rapidly varying incident spherical wavefront for which plane wave approximations are clearly not valid, even locally.

With the given radiation pattern of feed horn as shown in Figure 3.3, the appropriate distance between the horn and the center of reflectarray can be estimated by considering the spillover and taper efficiencies relations given in (Balanis, 1997; Pozar, Targonski, and Syrigos, 1997). At optimum value of aperture efficiency, a *f/D* ratio provides spillover and taper efficiencies of 76% and 84% respectively. Thus feed distance is chosen to be of 19.91 cm at 10λ reflector diameter. Note that this design provides an amplitude taper of 4.773 dB at the edge of the reflectarray in the E-plane and approximately 5.33 dB in the H-plane.

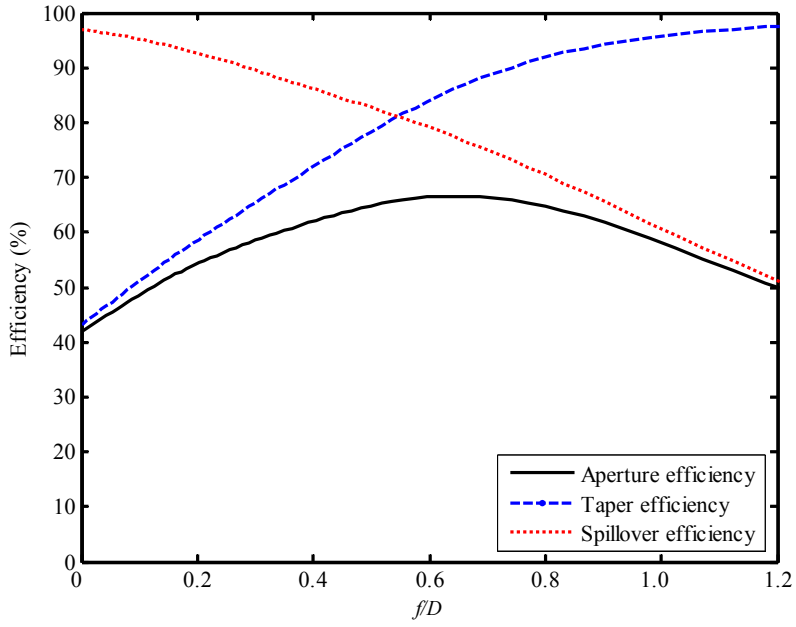

Figure 3.4 Reflectarray efficiency.

For the design discussed above, a *f/D* ratio of 0.66 referenced to the D_x dimension was selected with $D_x = D_y$ equal to 30 cm, where the feed distance *f* is located at a point that maximizes aperture efficiency (67%). This corresponds to a maximum incidence angle of 30 degrees in the xz- and yz-planes. The design is optimized for operation over the frequency 10 GHz.

3.4 Shaped Reflector Design

The relation of various shaped reflectors versus the desired beamwidth was reported in the literature (Wongsan et al., 2006). Due to this, only the basic details necessary to generate a well-designed backscatter will be discussed here. This section describes geometrical functions such as, triangular, quadratic, circular, Gaussian, cosine, squared cosine, and parabolic distributions where *D* is assumed to be the diameter and *A* is the depth of the shaped backscatter, respectively. Figure 3.5 shows several types of geometrical functions distribution where $-D/2 \le z' \le D/2$ and $z' = \sqrt{x^2 + y^2}$.

1. Triangular backscatter

$$f(z') = A\left(1 - \frac{2}{D}|z'|\right) \tag{3.4}$$

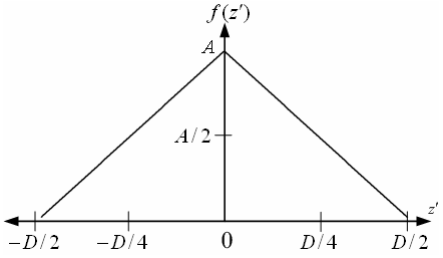

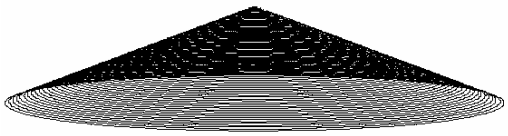

2. Quadratic backscatter

$$f(z') = A\left[1-\left(\frac{2}{D}z'\right)^2\right] \tag{3.5}$$

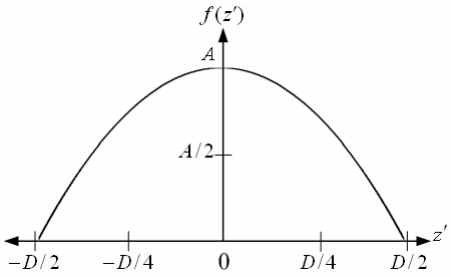

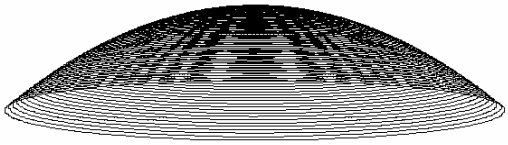

3. Circular backscatter

$$f(z') = A\sqrt{1-\left(\frac{2}{D}z'\right)^2} \tag{3.6}$$

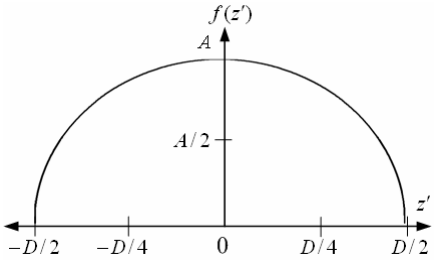

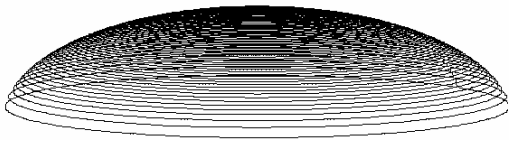

4. Gaussian backscatter

$$f(z') = Ae^{-(\frac{2}{D}z')^2} \tag{3.7}$$

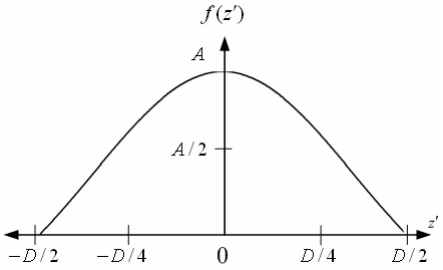

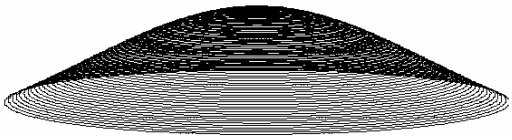

5. Cosine backscatter

$$f(z') = A\cos\left(\frac{\pi}{D}z'\right) \tag{3.8}$$

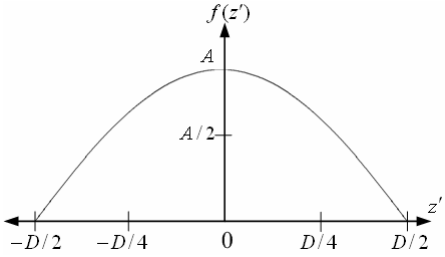

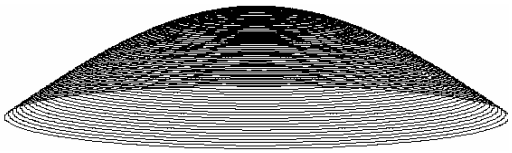

6. Squared cosine backscatter

$$f(z') = A\cos^2\left(\frac{\pi}{D}z'\right) \tag{3.9}$$

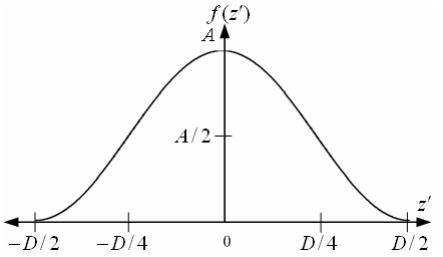

7. Parabolic backscatter

$$f(z') = (z')^2 / 4f \tag{3.10}$$

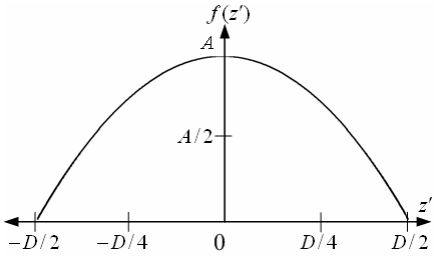

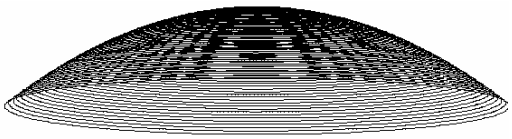

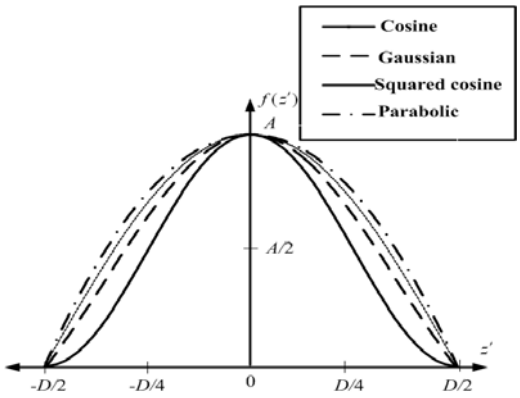

(a)

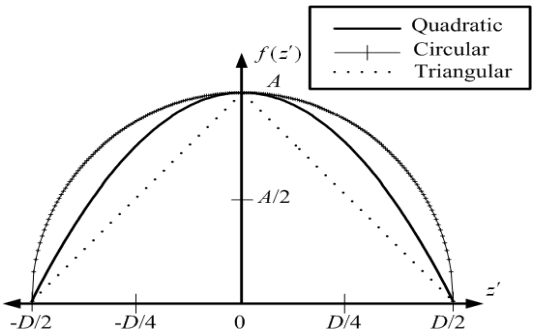

(b)

Figure 3.5 Geometrical function distributions.

3.5 Element Spacing Determination

Figure 3.6 shows the geometry of an infinite reflectarray element. As indicated, s is the center-to-center elements spacing in the x and y directions and L is the element size. To avoid the physical contacts among the adjacent elements, the grid spacing must be larger than the element size L,

$$\min\{\text{unit cell size}\} = L. \tag{3.11}$$

The numerical tools developed in Chapter 2 can then used to study the effect of the size L of any particular element on its reflection coefficient that we will discuss in Section 3.7. These numerical simulations have suggested that, imposing a minimum bound around $\lambda_0/2$ for the elements spacing s, will correct both problems.

The dependence of the reflection coefficient phase with the incidence angle θ_i was also studied using the infinite array environment. It was found that, if the spacing between elements was made as small as possible, the reflection coefficient phase of the infinite array can be made practically independent of the incident angle. Hence, in a practical design the grid spacing s should be designed as small as possible.

The effective method for decreasing the grid spacing is to print the reflectarray elements on substrate, which reduces the size of reflectarray elements (Kin-Lu Wong, 2002).

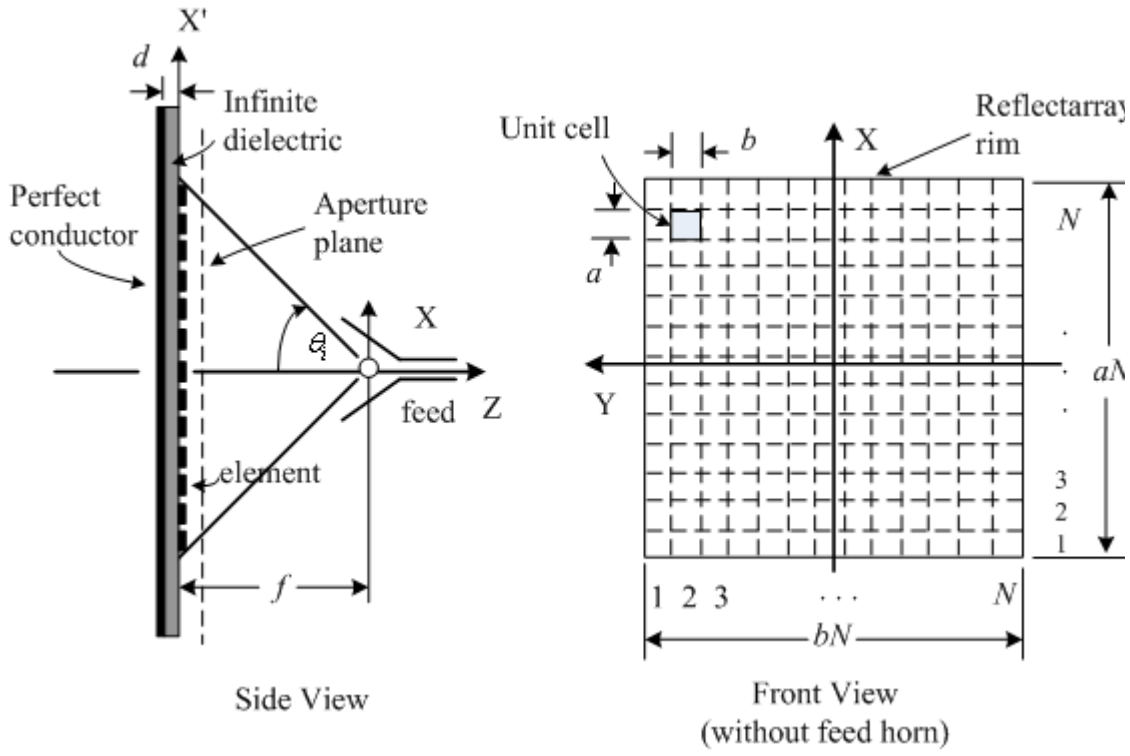

(a)

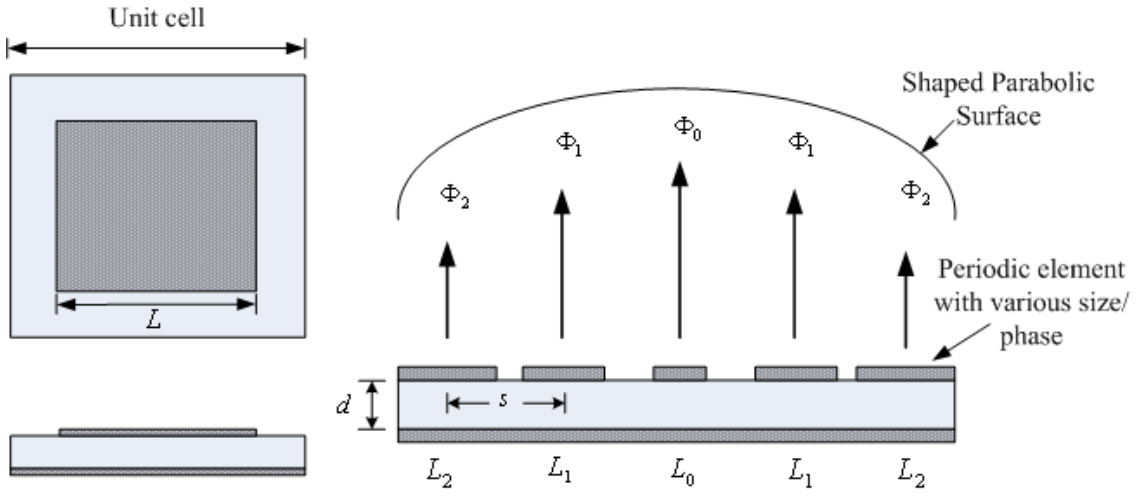

(b)

Figure 3.6 Geometry of an infinite reflectarray element.

3.6 Determination of the Unit Cell Required Phase Delay of Broad-Beam Microstrip Reflectarray Antenna

By using backscattering technique as shown in section 2.5.4, Figure 3.7 illustrates the incidence of wave on the surface of an analysis model of printed microstrip reflectarray, which parameters used in this figure are described below:

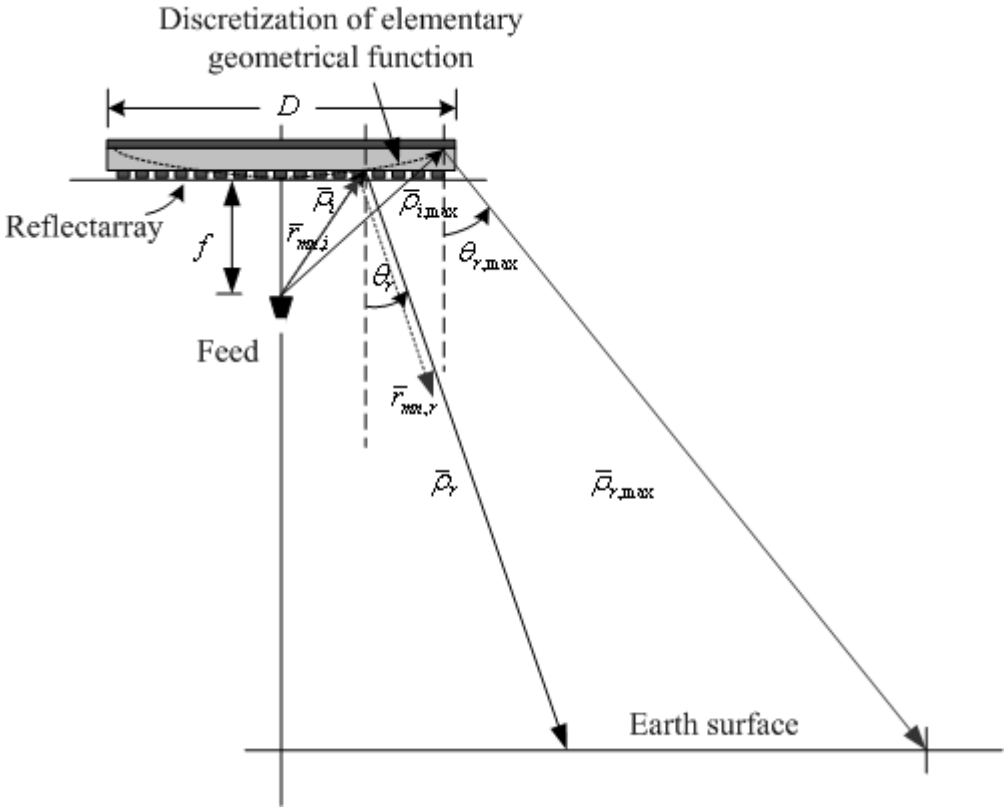

Figure 3.7 Analysis model of broad-beam microstrip reflectarray.

$\vec{r}_{mn,i}$ the vector from the feed to the *mn*-th reflectarray element, which can be obtained by using flat geometry,

$\vec{r}_{mn,r}$ the reflected vector from the reflectarray surface to far-field,

$\vec{\rho}_i$ the vector from the feed to the shaped reflector surface, which can be obtained

by using curvature geometry,

$\vec{\rho}_r$ the reflected vector from the shaped reflector surface to far-field,

θ_i incidence angle,

θ_r reflection angle,

D dimension of the reflector,

f distance between the feed and the center of the reflectarray.

In general, the feed may be positioned at distance from the reflectarray. The path lengths from the feed to all reflectarray elements are all different, which lead to different phase delays. In this thesis, the desired phase delay is determined on the construction of the curvature of a shaped backscatter surface with the help of Snell's law. The relations of the microstrip reflectarray surface to the shape of backscatter are two coordinate systems in this figure: one describes the coordinates (x_r, y_r, z_r) of the reflectarray and the other one describes the coordinate (x_b, y_b, z_b) of the backscatter. The selected shaped reflector is determined by using functions of elementary geometric ($f(z')$) that aperture cross sections of all backscatters are confined to be circular, same diameter, and radius of point source is very small. Since the reflectarray is designed, the following coordinate is used to find the point on the backscatter surface at a given patch element position on the reflectarray as given by

$$x_b = x_r + \left| f(z') - z_r \right| \tan\theta_i \cos\phi_i, \tag{3.12}$$

$$y_b = y_r + \left| f(z') - z_r \right| \tan\theta_i \sin\phi_i, \tag{3.13}$$

where the phase center of the feed is located at $(0,0,0)$ and the incidence angle can be

described in terms of geometrical dimensions

$$\theta_i = \tan^{-1}\left[\frac{\sqrt{x_r^2 + y_r^2}}{f}\right], \tag{3.14}$$

$$\phi_i = \tan^{-1}\left[\frac{y_r}{x_r}\right]. \tag{3.15}$$

The total path length from the feed to the reflectarray aperture is the sum of the distance from the feed to a point on the backscatter surface and the distance from that point to the corresponding point on the reflectarray with the rays satisfying Snell's law on the backscatter surface. In the analysis of backscatter, it is desirable to find a unit vector that is normal to the local tangent at the surface reflection point

$$\hat{n} = \frac{\nabla\left[z - f(z')\right]}{\left|\nabla\left[z - f(z')\right]\right|}. \tag{3.16}$$

With the help of Snell's law of reflection, the reflected angle for the backscatter can be expressed in Equation (3.17).

$$\theta_r = 2\cos^{-1}\left[-\frac{\bar{\rho}_i}{|\bar{\rho}_i|}\cdot\hat{n}\right] - \theta_i. \tag{3.17}$$

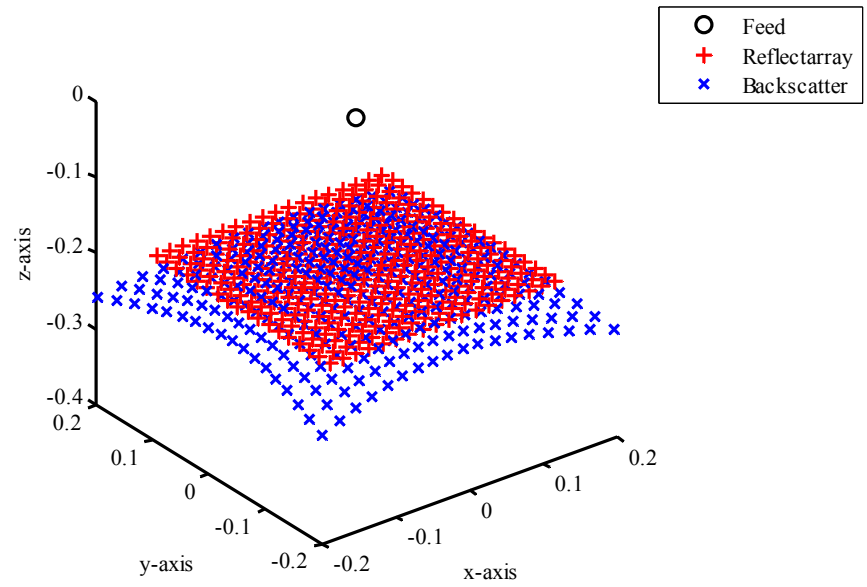

(a)

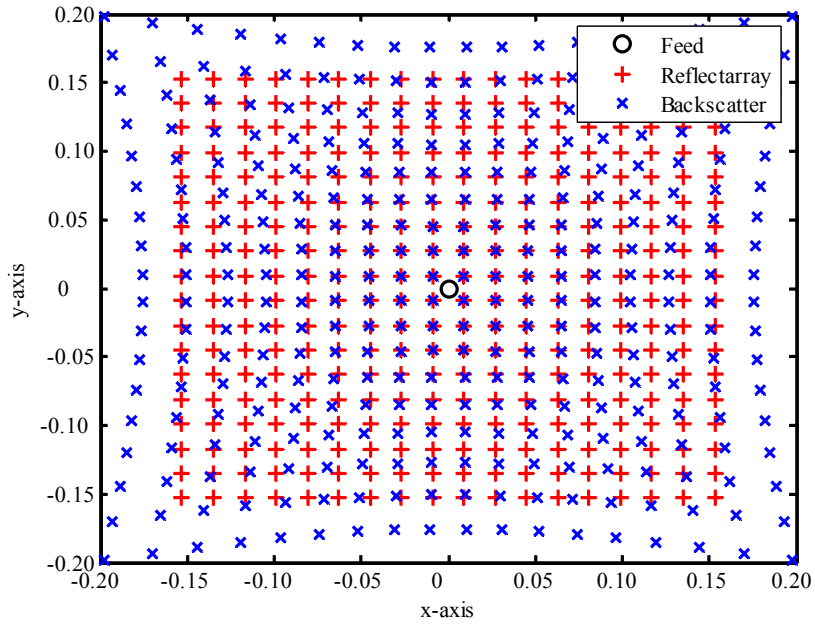

(b)

Figure 3.8 Unit cell position versus backscatter surface in the same incident field direction.

The differential path length (ΔL_{mn}) and the phase delay ($\Delta\Phi_{mn}$) for the *mn*-th reflectarray element are given by

$$\Delta L_{mn} = \left|\bar{\rho}_i\right| + \frac{z_b - f}{\sin\theta_r} - \left|\bar{r}_{mn,i}\right|, \tag{3.18}$$

$$\Delta\Phi_{mn} \text{ in degree} = \left[\left(1-N\right)k_0\Delta L_{mn}\right]\frac{360}{2\pi}, \tag{3.19}$$

where N is integer. The above indicates that the compensating phase can be repeated every 360 degree, and the portion that is an integer multiple of 360 degree can be deleted.

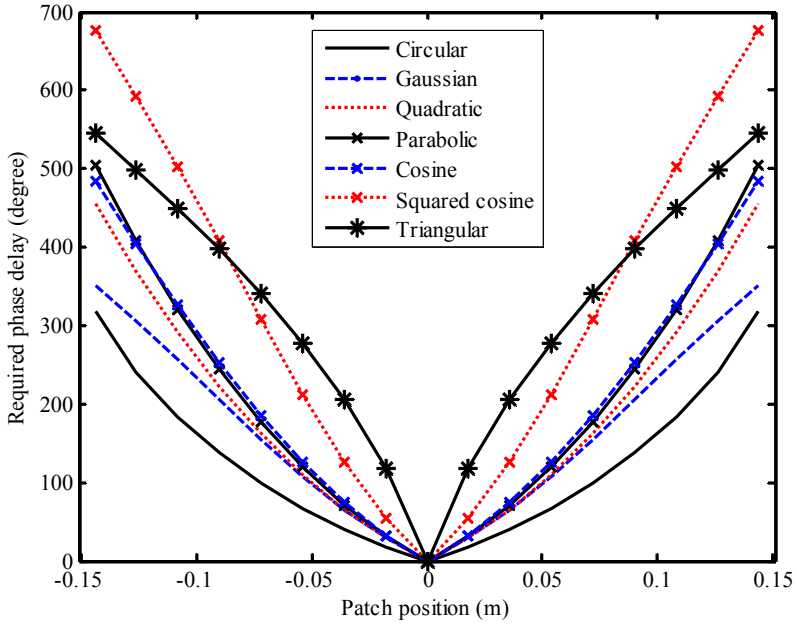

Figure 3.9 Desired unit cell phase delay versus unit cell position for various geometrical functions.

Figure 3.8 shows unit cell center position versus backscatter surface in the same incident field direction. From Equation 3.19, the required phase delays of all elements are calculated at center frequencies (f_0 = 10 GHz)as shown in Figure 3.9 and will be used to design the dimension of the reflectarray elements. These phase delays are duplicated the same radiating aperture as backscatter, which its geometrical function can be written in Section 3.4.

3.7 Determination of the Element Characterization

The most important and critical segment of the reflectarray design are its element characterization. If the element design is not optimized, feed will not effectively scatter the signal to elements for an efficient far-field beam forming. Its beamwidth must correlate correctly with the reflectarray's *f/D* ratio to accommodate all incident angles from the feed. Its phase change versus element change (patch size, delay line length, etc.) must be calibrated correctly. To obtain a constant planar wavefront at the z = 0 plane when the antenna is transmitting (the condition for maximum gain), the phase $\angle\Gamma_i$ of the reflection coefficient of the ith unit cell (area s^2) must be selected according to

$$\angle\Gamma_i = k_0(r_{mn} - \overline{r}_{mn} \cdot z) \pm 2\pi N + \varphi_0 , \tag{3.20}$$

where the vectors $\overline{r}_{mn}$ is defined in Figure 3.1, N is an integer number (selected to make $\angle\Gamma_i$ fall inside the range that can be implemented by the reflectarray element), and φ_0 is an arbitrary phase constant. Note that $\overline{r}_{mn}$ corresponds to the center point of each reflectarray element.

3.7.1 Reflection Coefficient Analysis Using Computer Program

It was seen in section 2.6.9 that the total dyadic reflection of an infinite space-fed array have in general four terms each [see Equation (2.163)]. However, depending on the element geometry and the incident plane wave arrival direction and polarization, several of these terms reduce to zero. Taking advantage of this fact to validate the theory and associated numerical tool developed, a convenient array test geometries have been selected and measured under normal illumination. Using a microwave network analyzer, reflection coefficient measurements were performed on a reflection mode array (i.e., an array backed by a ground plane). The corresponding experimental and numerical results are presented below.

The patch element depicted in Figure 3.6(b) was selected for the reflection coefficient test. This particular geometry was developed to desensitize the resonance frequency to etching errors. The patch-element characteristics are fully discussed in Sections 3.7.3 – 3.7.4.

Due to the nature of the symmetry involved in the patch element, it has been assumed that $R_{\phi\theta}^{tot} = R_{\theta\phi}^{tot} = 0$. Also, since the reflectarray is backed by a good electric conductor, its transmission coefficient is zero. Furthermore, since the geometries of interest in this work have quadrant symmetry $\overline{\overline{R}}^{tot}\Big|_{\phi=0^\circ} = \overline{\overline{R}}^{tot}\Big|_{\phi=90^\circ}$, it was observed that the dependence of $\overline{\overline{R}}^{tot}$ with ϕ_i could be neglected. Therefore, the reflection coefficient,

$$\Gamma = R_{\theta\theta}^{tot} = R_{\phi\phi}^{tot}, \tag{3.21}$$

completely characterizes the array.

For the reflection coefficient computations, the reflection reference plane is chosen as $z = 0$. Three reasonable assumptions can be made in the design of reflectarrays:

1. The incident field on each unit cell can be locally approximated by a plane wave,

2. The dimensional differences between elements do not affect their mutual coupling,

3. The reflection coefficient phase of the infinite array is dependent of the element spacing, substrate thickness, and incidence angle θ_i.

Assumptions 1 and 2 allow the simulations performed for infinite arrays to be used in the design of reflectarrays and are, in principle, only valid when the reflectarray is sufficiently far from the feed horn, so that the incident field is locally well approximated by a plane wave. However, they have been verified to work well in the *f/D* ranges used in high aperture efficiency (i.e., $f/D \geq 0.5$). Assumption 2 is supported by the fact that the mutual coupling between microstrip elements is very small for thin microstrip substrates (Pozar et al., 1997). Assumption 3 is based on the fact that the dependence of the reflection coefficient phase with element spacing, substrate thickness, and incident angle can be reduced through the use of a small element spacing, and hence made tolerable for the *f/D* values of interest in this work.

A reflectarray is designed using single-layer square microstrip patches on Taconic TLY-3 substrate, $\varepsilon_r = 2.33$, with a thickness of $d = 0.787$ mm. Appropriate patch lengths are selected for a given incident angle θ_i, such that a constant phase is achieved, satisfying Equation (3.19) for a broadside beam. This

requires that the patch length L be deviated from its resonant length L_0, so that a corresponding phase is achieved. The resulting corrected patch length is L. The length deviation from the resonant length, designated as $\delta = L - L_0$, is employed as a normalized resonant patch length deviation δ / L_0. In an infinite periodic array, the resonant patch length at center frequency $f_0 = 10$ GHz for the thin substrate ($\varepsilon_r = 2.33$ and $d = 0.787$ mm) is $L_0 = 0.93$ cm.

In most cases of interest in this paper, we are concerned with one incident polarization and incidence angles which preclude coupling to the orthogonal polarization. In addition, as previously stated, the element configuration is chosen such that only the dominant (m,n) = (0,0) mode propagates. As pointed out in (Pozar et al., 1997), for this case the reflection, scattering and total field matrices reduce to the coefficients $R_{\theta\theta}$, $S_{\theta\theta}$, and $R_{\theta\theta}^{tot}$ Conservation of energy for a lossless dielectric slab requires $|R_{\theta\theta}| = 1$, $|R_{\theta\theta} + S_{\theta\theta}| = 1$, and $0 < |S_{\theta\theta}| < 2$. At resonance the magnitude of $S_{\theta\theta}$ equals two and $\angle S_{\theta\theta}$ is exactly 180º out of phase with $\angle R_{\theta\theta}$.

3.7.2 Reflection Coefficient Phase versus Element Dimension

As a consequence of the above three assumptions, a single curve depicting the infinite array reflection coefficient phase versus element dimension, at the incident angle $\theta_i = 0°$, suffices to determine elements' dimension. This type of curve is element and grid dependent, can be generated using the material of Chapter 2, and has the general appearance shown in Figure 3.10. Subject to the grid constrains the curve shows that any $\angle\Gamma$ value between $\angle\Gamma_{\min}$ and $\angle\Gamma_{\max}$ can be implemented by changing the element's dimension TL. Having $\angle\Gamma_{\max} - \angle\Gamma_{\min}$ smaller than the

required 360º range causes some performance degradation. Since at some reflectarray unit cells, an incorrect reflection coefficient will have to be carried out. To account for this possibility, from now on Γ_i will be the desired reflection coefficient [given by Equation (3.20)], and Γ_i^a will be the actual implemented reflection coefficient (interpolated in Figure 3.10). On the other hand, having $\angle\Gamma_{max} - \angle\Gamma_{min}$ larger than the required 360º range is a convenient characteristic since less regions of abrupt dimensional discontinuity (i.e., zoning over the array surface) can be used. Since large array, these discontinuities cannot be modeled accurately, minimizing their number can increases the performance of the antenna.

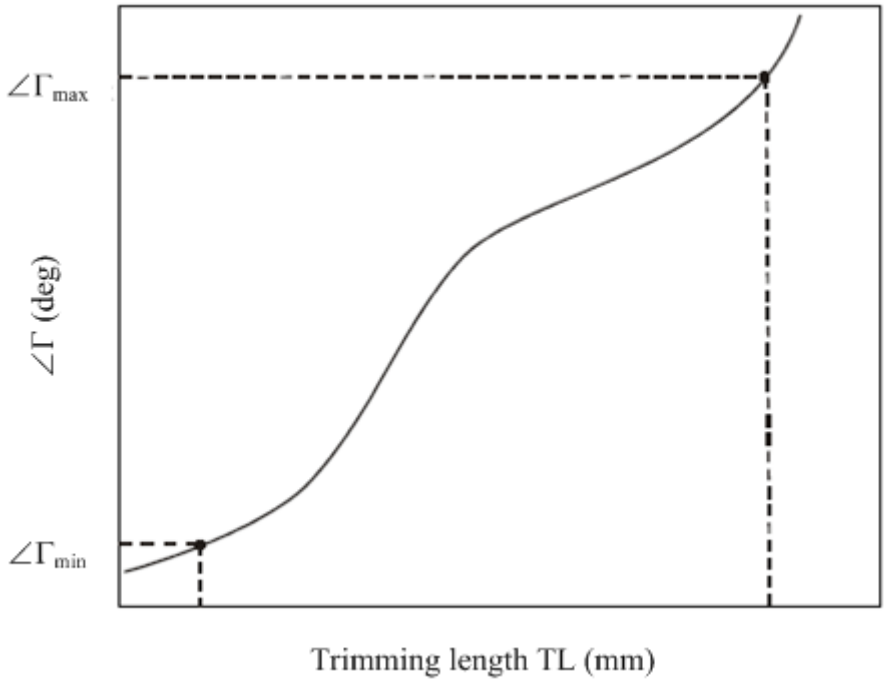

Figure 3.10 Reflection coefficient phase of an infinite array of elements versus trimming length.

To provide the largest possible region without abrupt element dimension changes in the center region of the reflectarray (region of larger illumination), the reflection coefficient phase $\angle\Gamma_i$ of the unit cell located at $\overline{r}_f = \overline{r}_{mn}$ is made equal to $\angle\Gamma_{\min}$. Hence, using Equation. (3.20) with $N = 0$ yields

$$\varphi_0 = \angle\Gamma_{\min} - k_0(r_f - \overline{r}_f \cdot z). \tag{3.22}$$

The required $\angle\Gamma_i$ of each unit cell center ($\overline{r}_{mn}$ points) can now be determined starting with $N = 0$ at the reflectarray center (point with $\Gamma_i = 0$), increasing Γ_i (moving towards the rim), and using Equation. (3.20) to calculate the corresponding Γ_i. N is kept equal to zero as Γ_i increases until $k_0(r_{mn} - \overline{r}_{mn} \cdot z) + \varphi_0 < \angle\Gamma_{\max}$. After that, N is selected as an integer number such that. Once all Γ_i have been obtained, interpolation on the curve of the reflection coefficient phase versus element dimension (i.e., Figure 3.10 for the particular element used) yields the trimming length of the *i*th unit cell element.

3.7.3 Characteristics of Square, Square Loop, and Cross Element Geometries

Several array element geometries have been proposed and used in reflectarrays. Regardless of the element employed, basically three approaches have been used to electrically control the reflected wave phase in reflectarrays: elements of variable size (Pozar, Targonski, and Syrigos, 1997), elements with stubs of variable lengths (Munson, Haddad, and Hanlen, 1987), and elements with variable rotation angles (Huang and Pogorzelski, 1998). Although each approach has its own advantages and drawbacks, they all depend on accurate photolithography to assure the

desired element geometry. Any error translates into a reflected-wave phase error that has a negative impact on the antenna performance. As such, for maximum performance, especially at millimeter-wave frequencies, it is best to use elements with reduced sensitivity to etching errors. The first order of business when implementing a reflectarray is then to select an appropriate array element.

To establish the electrical properties of any particular array element, the numerical tools developed in Chapter 2 can be used to calculate the reflection coefficient phase $\angle\Gamma$ of the element in the infinite-array environment. In this section, these tools are used to analyze the sensitivity to etching errors of three representative element geometries; square patch, square loop, and cross dipole.

The reflection coefficient phase $\angle\Gamma$ of the element geometries depicted in Figure 3.11 are basically controlled by the L dimension. Repeated use of the numerical tools of Chapter 2, with L varying, then yields the plots of Figure 3.12. Although all these elements in the figures resonate (i.e., produce $\angle\Gamma = 0°$) when $\Delta L = 0$, they do not have identical sizes at resonance. The square loop has the smallest resonant size (L_0=6.33 mm) and followed, in order, by square patch and cross dipole. Of particular relevance here is Figure 3.12(b), which shows the phase sensitivity of the elements with L. As this plot indicates, the square microstrip patch has the smallest phase sensitivity of all three elements. Therefore, the square microstrip patch is the most tolerant to etching error, and hence most suitable for use at higher frequencies. In practice, it is often desired to use an array element with even less phase sensitivity. To achieve this, one needs geometry in which the reflection coefficient phase does not depend so strongly on a single dimension. The square microstrip patch element is a possible geometry that accomplishes this.

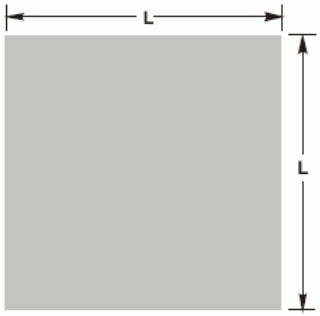

(a)

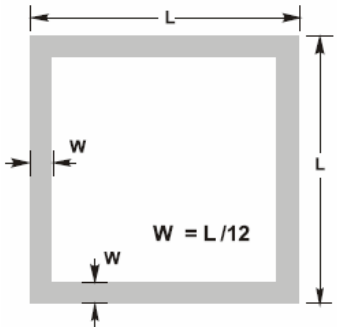

(b)

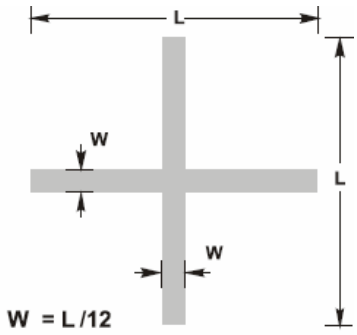

(c)

Figure 3.11 Element geometries: (a) square patch, (b) square loop, and (c) cross dipole.

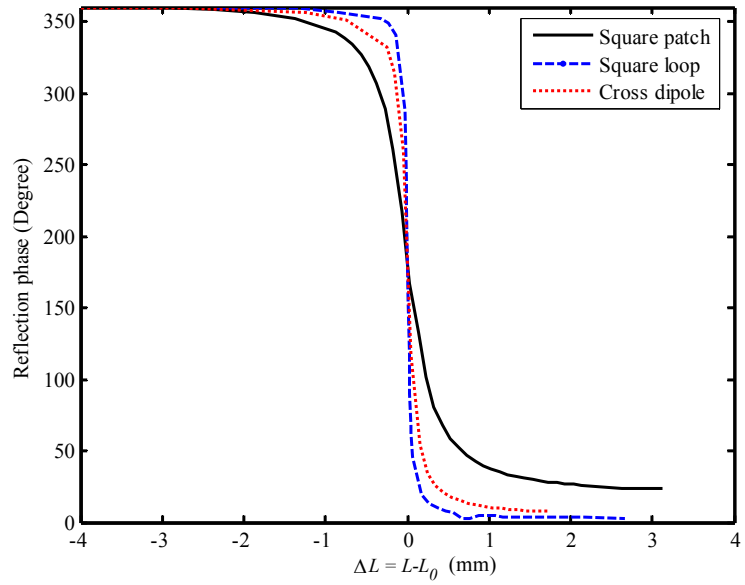

(a) phase

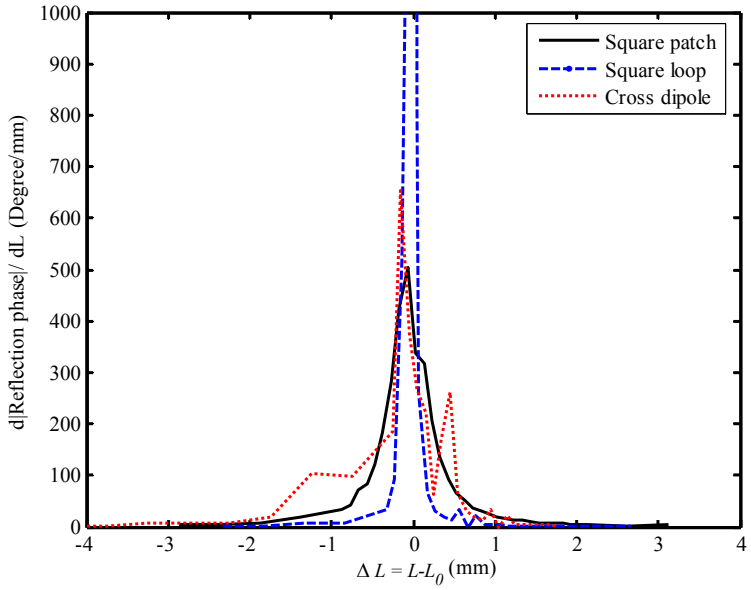

(b) phase sensitivity

Figure 3.12 Reflected wave phase of an infinite array of the square, square loop and cross microstrip elements versus the element size at $s = 0.6\lambda_0$

3.7.4 Characteristics of Square Microstrip Patch Element Geometry

Using the numerical tools developed in Chapter 2, the square microstrip patch element was developed to reduce the sensitivity of the reflection coefficient phase (controlled by adjusting the trimming length *TL*). In this process, the square element was tessellated in $N_L \times N_L$ rectangles. After the simulation at f_0 = 10 GHz, d = 0.787 mm, ε_r = 2.33, $s = 0.6\lambda_0$, and $\theta_i = \phi_i = 0°$, the curve depicted in Figure 3.13 was obtained. It shows the calculated reflection coefficient phase $\angle\Gamma$ for an infinite array of square microstrip patch elements. This element can be used near any of these *TL* values to implement any desired phase. This figure, it clearly shows a significantly reduced slope in the reflection coefficient phase with *L* (note that Figure 3.11 uses *L* as a variable, instead of *TL*)

Figures 3.13-3.16 show simulated results of reflection phase of infinite array. The obtained results indicated that, if the element size *L* is excessively small, either the reflection phase cannot be made to cover the full required 0° to 360° phase range or it changes excessively fast around the element resonance. The square patch can implement a range from 26.3° to 360°. This available phase shift rang is limited by the reflectarray antenna bandwidth (around 4%).

According to the trends discussed in Section 3.5, the reflection coefficient phase, $\angle\Gamma$, dependence with element spacing is desired. In Figure 3.14, the reductions of unit cell size of reflectarray can reduce the slope of the phase response. For achieving reflectarray element with a reduced size at a fixed operating frequency, the unit cell size is to print the element on substrate, which reduces the size of reflectarray element. In microstrip antenna, many techniques have been reported to

reduce the size of reflectarray element at a fixed operating frequency (Kin-Lu Wong, 2002). In general, reflectarray elements are half-wavelength structures at reflection phase 180° and operated at a resonant frequency.

Deterministic phase errors can also be introduced by several other mechanisms, leading to loss in directivity and degradation of the pattern. As seen from Figure 3.15, phase error can arise with patches on thick substrates, since the reflection phase for such cases does not approach to zero for large patch length. This occurs because for patches well below resonant size, reflection takes place from the ground plane, while larger patches tend to occupy most of the unit cell, causing reflection primarily from the patch surface. The difference in path length $2k_0d$ represents the range of reflection phase that is unattainable for elements that fill a large fraction of the unit cell. Actually, there is typically only a small percentage of patches with phases that would occur in this range, so the overall effect is not as severe as might be expected.

Figure 3.16 depict the reflection coefficient of the square patch arrays, for several values of the incidence angle θ_i. Observation of the Γ curves indicate that the excessive phase dependence with θ_i coincides. In particular, when $\theta_i = 45^o$ and all elements resonate, the high element currents generate a strong grating lobe that does not radiate towards $\theta_r = 45^o$, and hence cause the energy loss.

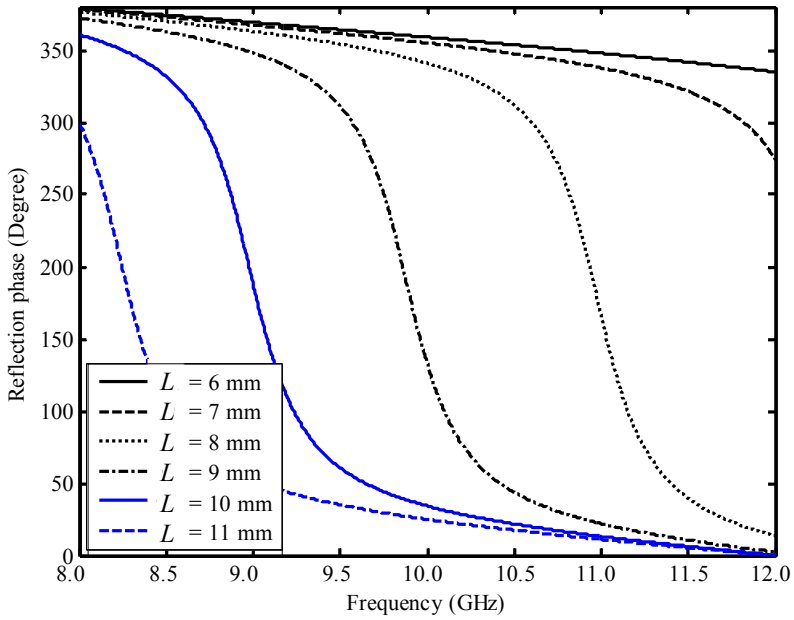

Figure 3.13 Reflection coefficient phase of an infinite array of square patch versus frequency for various element sizes.

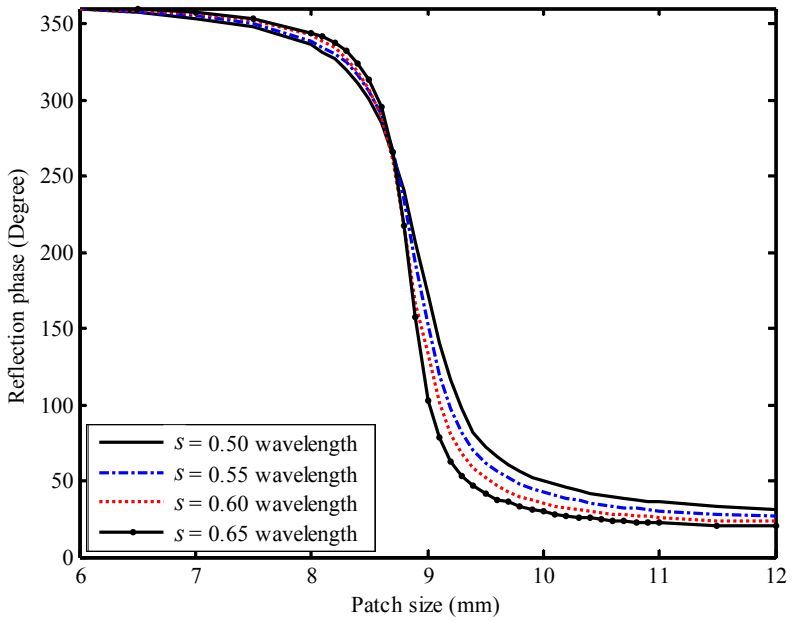

Figure 3.14 Reflection coefficient phase of an infinite array of square patch versus element size for various element spacing.

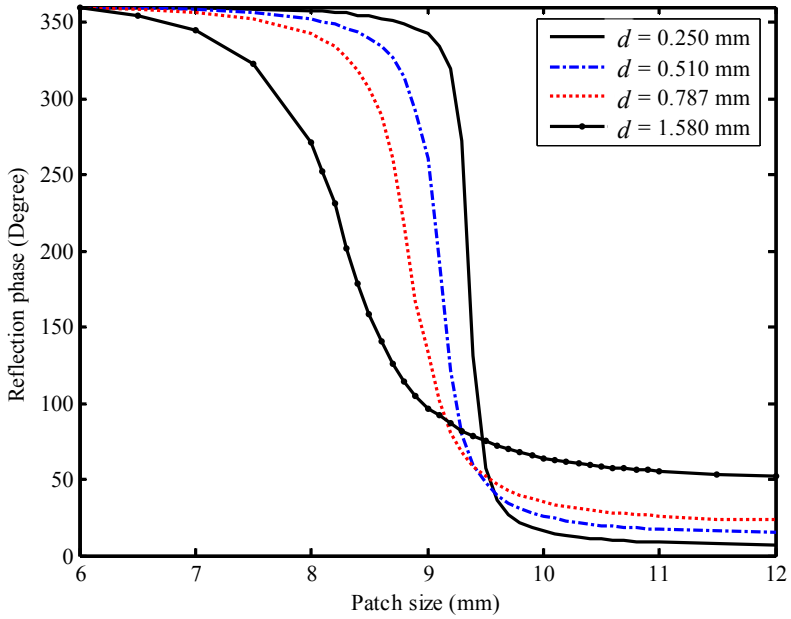

Figure 3.15 Reflection coefficient phase of an infinite array of square patch versus frequency for various substrate thicknesses.

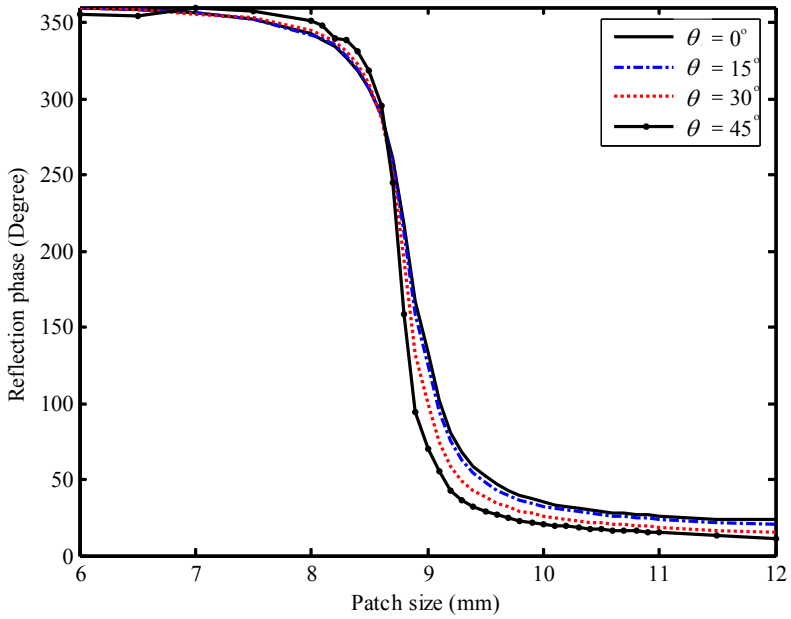

Figure 3.16 Reflection coefficient phase of an infinite array of square patch versus element size for various incident angles.

3.8 Far-Field Radiation

With the compensating phases of all elements known, the far-field radiation patterns can be calculated by the conventional array theory (Huang,1994), where the radiations of all elements are summed together. Considering a planar array consisting of $M \times N$ elements that are nonuniformly illuminated by a low-gain feed, the reradiated field from the patches in an arbitrary direction, $\hat{u}$, will be of the form:

$$E(\hat{u}) = \sum_{m=1}^{M} \sum_{n=1}^{N} F(\overline{r}_{mn} \cdot \hat{a}_z) \cdot A(\overline{r}_i \cdot \hat{u}_r) \cdot A(\hat{u} \cdot \hat{u}_r) \cdot \exp\left[-jk_0 \left(|\overline{r}_{mn}| + \overline{r}_i \cdot \hat{u} \right) - j\Delta\Phi_{mn} \right], \tag{3.22}$$

where F is the feed pattern function, A is the reflectarray element pattern function, $\overline{r}_i$ is the vector from the centre of reflectarray to mn-th element, $\hat{u}_r$ is the unit vector of reflected field, and $\Delta\Phi_{mn}$ is the required compensating phase of the mn-th element calculated by Equation (3.19).

3.8.1 Radiation Pattern of Pencil Beam Reflectarray

The far-zone radiation pattern of the pencil beam reflectarray, which is computed using Equation (3.22), is depicted in Figure 3.17. As seen from these plots, the calculated gain and -3 dB beamwidth in H-plane are 39.5 dB and 3º, respectively.

3.8.2 Synthesis of Ideal Illumination Pattern

The translation of power illumination pattern function with smooth transition to the far field in polar coordinates yields the $\sec^2$ pattern (Smulders et al., 2001). The required important feature is the transmitted power that has to be efficiently distributed over the actual coverage area whereas outside the coverage the

field strength has to fall off rapidly. The $\sec^2$ pattern is so called earth matched beam or broad-beam pattern antenna (Love, 1978). Figure 3.18 shows the uniform aperture illumination, which is obtained for $\theta = \pm 60°$.

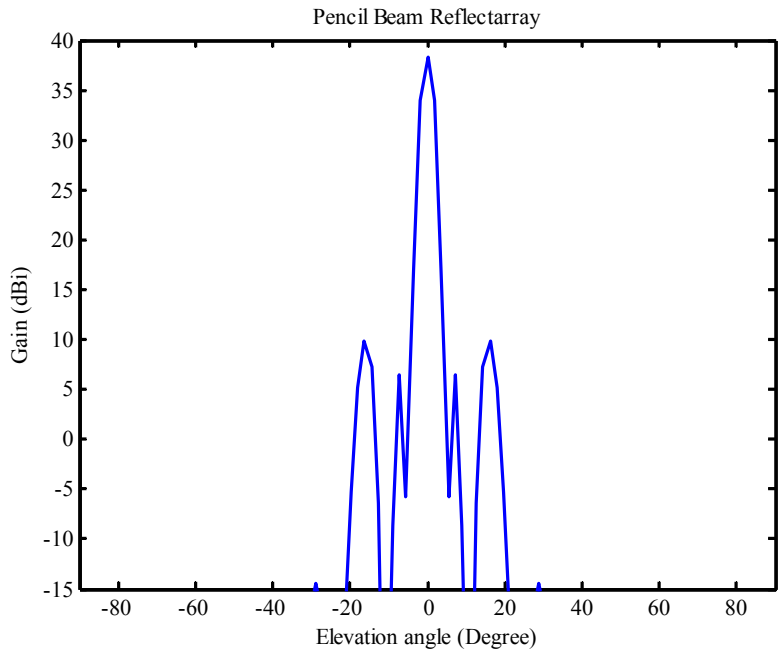

Figure 3.17 Radiation pattern in H-plane of pencil beam microstrip reflectarray using parabolic function at $f/D = 0.5$.

3.8.3 Synthesis Radiation Pattern of Broad-Beam Reflectarray Using Geometrical Function

In this Section, radiation patterns are synthesized by using geometrical functions and required phase delays in Sections 3.4 and 3.6, respectively. The calculated results indicate the different radiation patterns for various geometrical functions, which are shown in Figure 3.19. The prescribed field requirements have been satisfied by an appropriate choice of the radiating patches selected from the

complex design curves obtained in the analysis stage. The steepness of the pattern edges and the angular positions of these edges confirm that the antenna efficiently illuminates the target area to be covered (±65º). Radiation patterns are different due to phase of reflectarray elements, which are duplicated the same radiating aperture as backscatter. Because of phase change versus element change, each reflectarray type (as backscatter shapes) provides different characteristics such as -3 dB beamwidth (HPBW) and relative power, which are reported in Table 3.1.

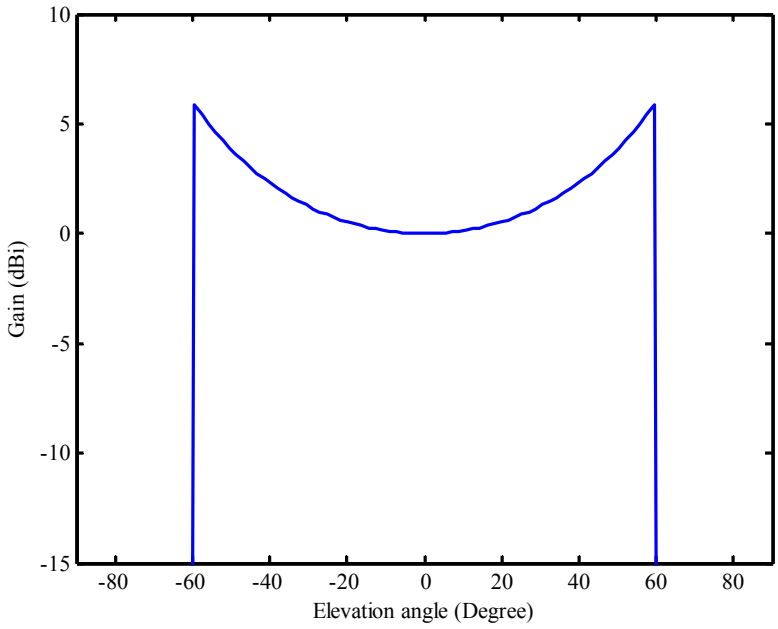

Figure 3.18 Uniform aperture illumination.

From Table 3.1, it is observed that the HPBW of seven backscatter reflectarray types are different. For average consideration, it is apparent that the squared cosine has the widest beamwidth and followed, in order, by Gaussian, cosine, quadratic, parabolic, and circular, which are 166º, 164º, 156º, 150º, 140º, and 133º, respectively, while HPBW of triangular is about 27º on each main beam. Since the

relative power is strongly coincided with the HPBW i.e., the narrower the beamwidth the higher the relative power and vice versa. However, reflection surface for reflectarray elements, which are synthesized in this paper, are placed position near centre of shaped backscatter. Thus, the circularly geometrical function yields the highest relative power and followed, in order, by parabolic, Gaussian, triangle, quadratic, cosine, and squared cosine, respectively. Figure 3.20 and Table 3.2 show predicted gain of reflectarray with various geometrical functions.

Table 3.1 Characteristics of various reflectarray types

Backscatter Shapes	HPBW (degree)	Maximum power (dB)
Circular	133	30.29
Gaussian	164	28.49
Quadratic	150	25.58
Parabolic	140	28.87
Cosine	156	24.27
Squared cosine	166	22.01
Triangular	27	28.06

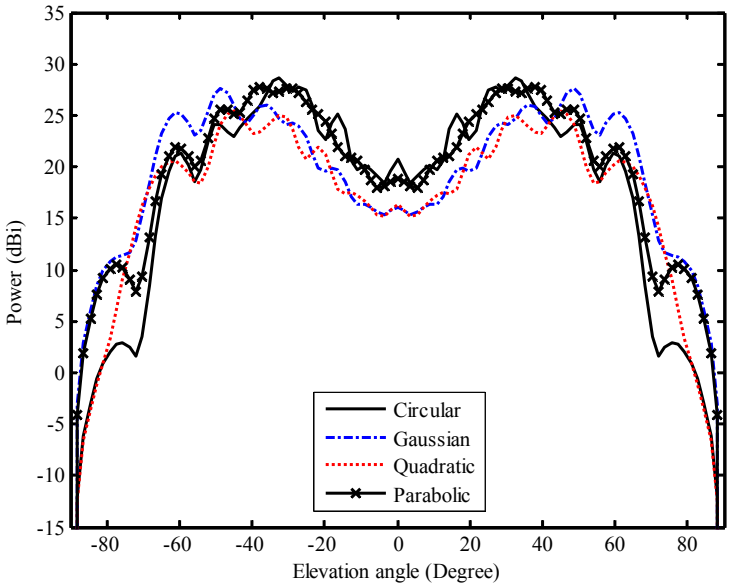

(a)

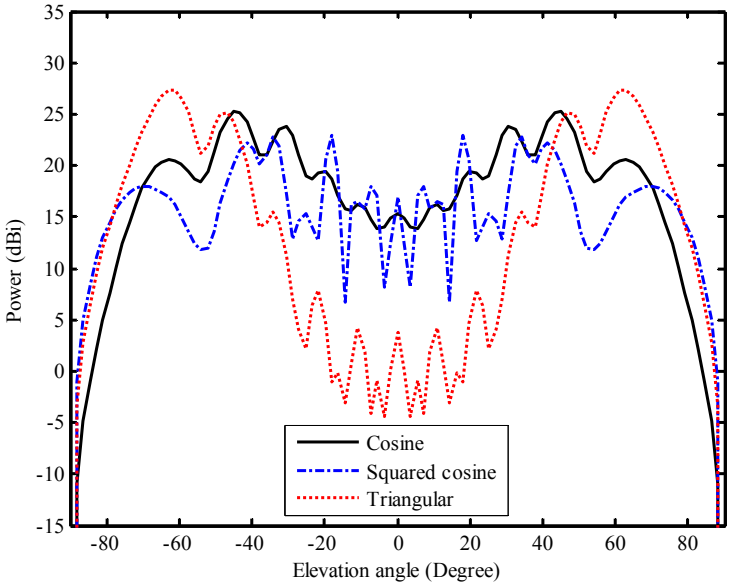

(b)

Figure 3.19 Radiation pattern in H-plane of microstrip reflectarray with various geometrical functions.

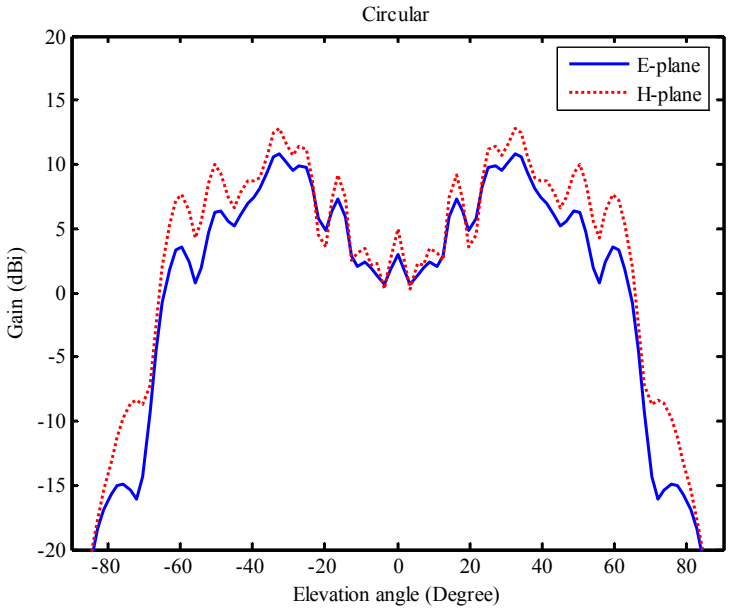

(a) Circular function

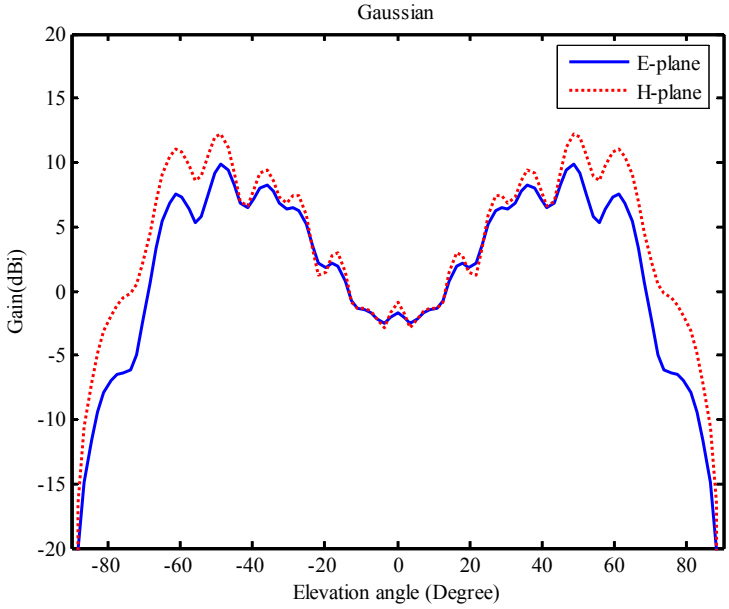

(b) Gaussian function

Figure 3.20 Predicted gain of microstrip reflectarray with various geometrical functions.

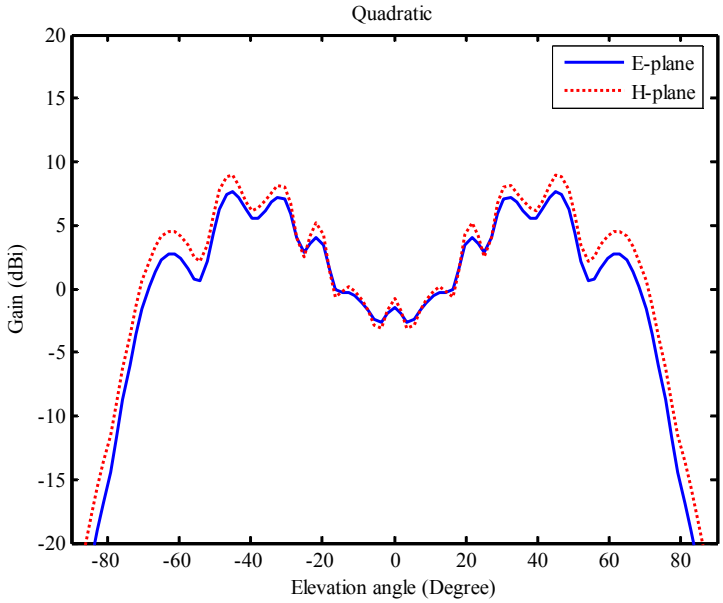

(c) Quadratic function

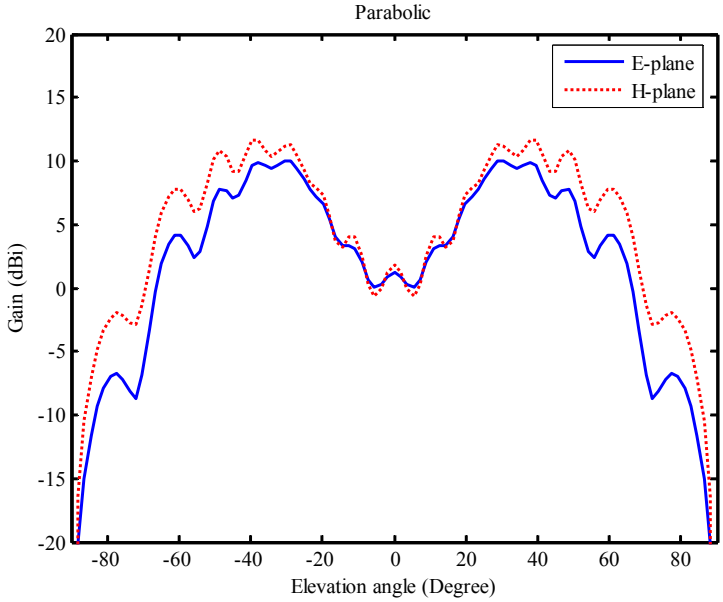

(d) Parabolic function

Figure 3.20 Predicted gain of microstrip reflectarray with various geometrical functions (Cont.).

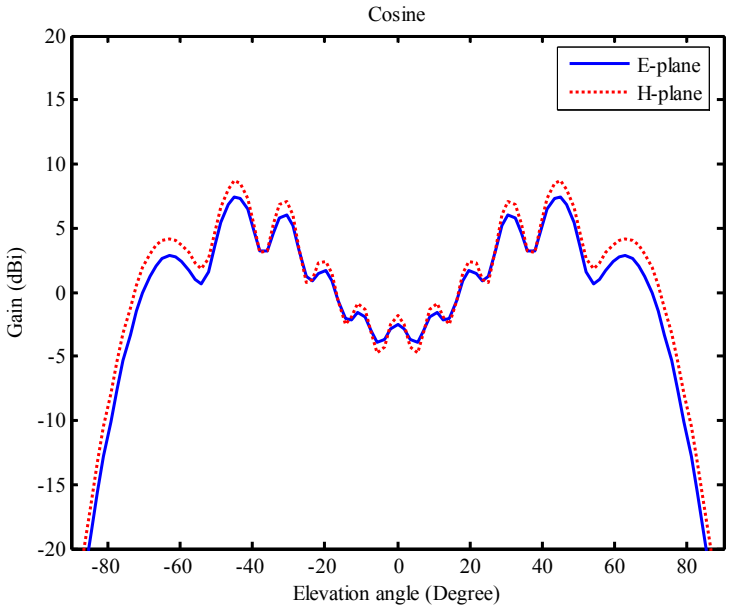

(e) Cosine function

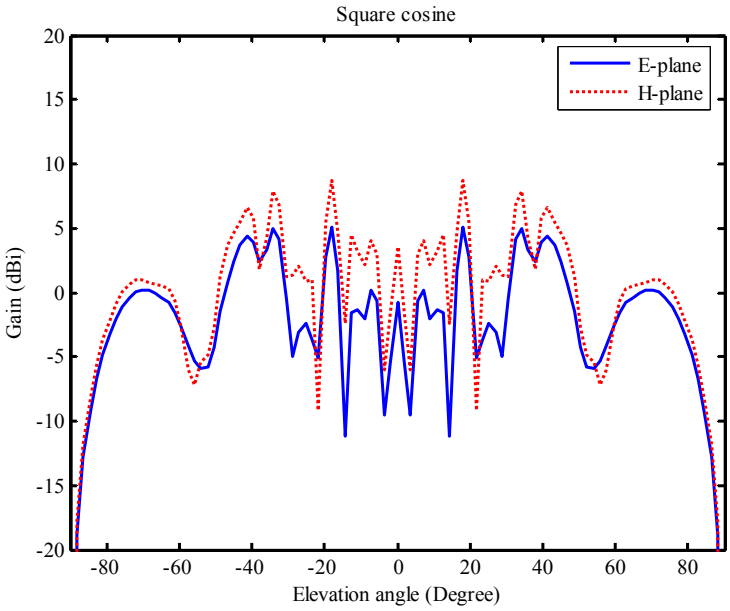

(f) Square cosine function

Figure 3.20 Predicted gain of microstrip reflectarray with various geometrical functions (Cont.).

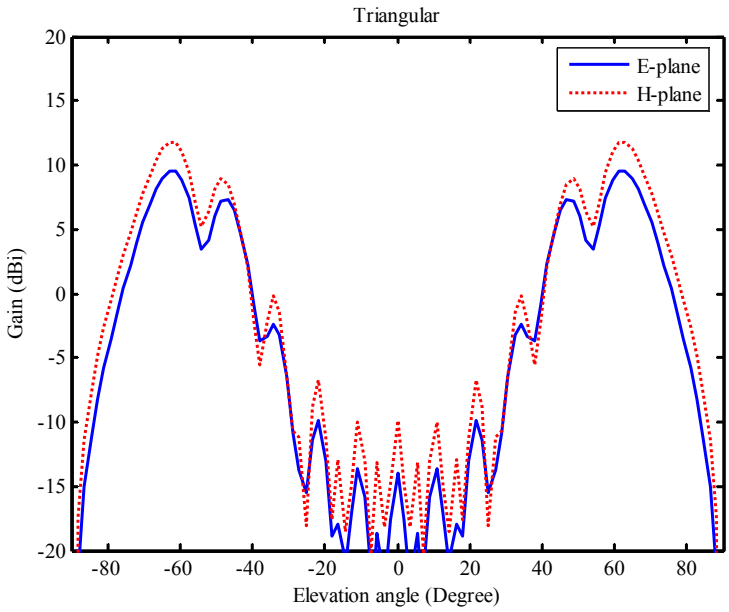

(g) Triangular function

Figure 3.20 Predicted gain of microstrip reflectarray with various geometrical functions (Cont.).

Table 3.2 Gain of various reflectarray types

Backscatter Shapes	Gain@$\theta = \pm 60^{o}$ (dBi)		Gain@$\theta = 0^{o}$ (dBi)	
	E-plane	H-plane	E-plane	H-plane
Circular	3.54	7.62	2.97	4.95
Gaussian	7.36	10.87	-1.64	-0.84
Quadratic	2.41	4.15	-1.48	-0.74
Parabolic	4.14	7.74	1.22	1.79
Cosine	2.37	3.65	-2.48	-1.82
Squared cosine	-2.67	-2.67	-0.79	3.55
Triangular	8.87	11.04	-13.93	-9.93

3.9 Chapter Summary

The design techniques of microstrip reflectarray antenna using discretization of elementary geometrical functions to synthesize the appropriated curvature for forming a wide-beam pattern of reflectarray are described. To achieve such broad-beamwidth, reflection phase of array elements of the reflectarray antenna is specifically designed to emulate the curvature of the backscatter by using patches of different sizes. The phase and radiation pattern synthesis method for microstrip reflectarray, which has to illuminate a predefined circular area, are presented by using variety of discretization of elementary geometrical functions such as, triangular, quadratic, circular, Gaussian, cosine, squared cosine, and parabolic distributions. These backscatter functions are discussed on merit and demerit to find appropriate radiation characteristics such as radiation pattern, -3 dB beamwidth, and maximum gain for utilization in WLAN application. To design propose antenna, the method of moment and the infinite-array are applied to calculate the scattering coefficients characteristic. Then phase of reflected fields are obtained and the actual size of microstrip patch elements are known.

From all the aforementioned of radiation characteristics calculated, it can be ascertained that a reflectarray can be chosen according to the characteristic requirements for practicable applications. For example, if the widest HPBW for large coverage area is required, then, the geometric function of squared cosine should be the best choice. However it must be noted that it also has the highest ripple level. If, on the other hand, we need a very high gain reflectarray antenna, the circularly geometrical function should be applied. From viewing the graphs of radiation patterns in Figure 3.19, it is easy to find the proper geometrical function which meets the

requirement of the characteristic specifications. To get more advantages in one characteristic while sacrificing the merit of another characteristic in the same backscatter function is difficult to avoid.

CHAPTER IV

MEASUREMENT AND DISCUSSION

4.1 Introduction

Having understood most of the general background and theory behind the microstrip reflectarray antenna, the development of a design procedure for the fabrication of a reflectarray that meets the requirements of a WLAN system will be conducted in this chapter, which dedicates to the overall development process of the 17×17 element reflectarray. The fabrication of a reflectarray prototype will be done and their performance will be measured and discussed. Table 4.1 depicts the required specifications of antenna, which will be followed achieve the element required to construct the reflectarray.

Table 4.1 Design specifications for antenna design

Parameters	Specification
Operating Frequency (f_0)	10 GHz
Direction of maximum gain of beam pattern	±65°
Gain (dBi)	≥5.8 dBi @ ±65°; ≥0 dBi @ 0°
Polarization	Linear
Antenna type	Broad-beam pattern
Diameter of reflector	30 cm (10λ)

In the last section of Chapter 3 (i.e., Section 3.9), a 10 GHz reflectarray using 289 elements was designed, and its predicted performance was discussed. The further calculations of key parameters such as radiation pattern, gain and half power beamwidth can also be evaluated. To verify the theoretical calculation, the radiation patterns were measured in an anechoic chamber using vector network analyzer HP 8722D and standard X-band horn. The measurement set up comprises two antennas, faced together at far field distance.

4.2 Single Patch Element Design and Fabrication

As microstrip radiators or printed antennas are ideal radiating elements for use in phased array antennas because of their advantages such as low cost, small size, light weight, and easy to fabricate into printed circuits boards using etching techniques. Microstrip radiators are built using thin dielectric substrate material as shown in Figure 4.1. The bottom surface is coated with conducting sheet that serves as ground plane while the upper surface is covered with element, which is etched into a desired shape. In the middle part, a substrate material usually made of alumina, quartz, and glass reinforced material is chosen.

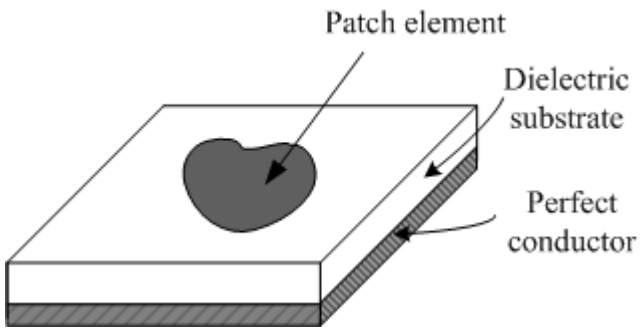

Figure 4.1 Physical structure of a microstrip patch antenna.

Whether a microstrip radiator is used as a single element or as a part of an array, a number of decisions have to be taken using a logical process in order to achieve a desired performance. This section summarizes some of these steps, which are applied to design a square microstrip patch, which is used in this thesis.

The first step in designing, a microstrip antenna is to choose an appropriate substrate. Key factors such as height (*d*), dielectric constant (ε_r) and loss tangent (tan δ) will have a significant impact on the overall performance of the antenna. These must be carefully chosen based on factors such as operating frequency and antenna type. For a given frequency, larger bandwidth of microtrip antenna can be successed by choosing a thicker substrate and low ε_r. However, the electrical characteristics of a substrate may also be affected by the environment (temperature, humidity, etc.), and ease of fabrication should be considered.

Secondly, design of the microstrip patch can be performed at the operating frequency by calculations the length of a square patch from Equation (4.1). However, this formula will result in an efficiency of radiator and a practical length of patch (Pozar, Schaubert, 1995). If the patch length is lower, then the antenna efficiency will be lower also. Nevertheless, if the patch has the larger length yielding more efficiency, then the scattering field from patch may be distorted in higher order modes.

$$L_0 = \frac{c}{2f_0}\sqrt{\frac{2}{\varepsilon_r + 1}} \tag{4.1}$$

As the exact value of *d* is determined by commercially available board thickness and the variation in dielectric constant to predict the actual dimensions, the reflection coefficient phase in development tool is useful for monitoring and

fine-tuning the design by sensitivity analysis. This provides the basis for the start of the design but finer adjustments have to be made to compensate and determine the best possible result. It can also be seen invariably from Equation (4.1) that the resonant frequency is affected by the patch length.

4.3 Reflectarray Design Methodology

Having gained confidence in the design process, design of broad-beam reflectarrays was done at 10 GHz with square patches as presented in Chapter 3. The following sections outline the design steps required to build a reflectarray. Essentially, 4 steps are required in the following order: selection of reflectarray material, derivation of the characteristics of the reflectarray, design and evaluation of the radiating elements, calculation of the variable length curves as a function of the reflected phase, and finally, calculation of the element lengths required at each of the cells.

As discussed in Chapter 3, numerical analysis methods are also used during the design process. These methods which are account for the dielectric substrate in a rigorous manner are often referred to as Method of Moments (MoM). In this thesis, the antenna design tools were used for the physical design of the individual microstrip radiator, optimum feed distance, synthesis of phase and radiation, and the key analysis of the phase response of the patches when used as an array. In the last part, the developed tool calculates antenna metrics such as far-field 2D plots, gain, and HPBW. Numerical methods where a full wave analysis is performed are requiring larger computing power (Windows XP PC was used in this study). In addition, these simulations took an excessive amount of time to be completed *(e.g.* 3 to 4 days).

4.3.1 Material Selection

As discussed in Sections 3.7 and 4.2, to minimize any error translates into a reflected-wave phase error of the design given the use of the square patches, Taconic TLY-3 was selected for all antennas because of its low ε_r and low loss factor (tan δ = 0.0009). Thick material was selected with recognition of the slight increased weight and cost. The dielectric constant (ε_r = 2.33) is uniform from panel to panel and is constant over a wide frequency range. Its low dissipation factor extends the usefulness to X-band and above, and this laminate is easily cut, sheared and machined to shape. It has excellent dimensional stability and is resistant to all solvents and reagents, hot or cold, normally used in etching printed circuits or in plating edges and holes. Normally supplied as a laminate with electrodeposited copper of 1/2 to 2 ounces per ft.^{2} on both sides, the Taconic TLY-3 composites can also be clad with rolled copper foil for more critical electrical applications.

Using this material, the 10 GHz antennas were built on 0.787 mm thick substrate with a copper layer of 1 oz per sq. ft (approximately 35 micron thick). The height of these substrates was comparable to those found in the reflectarray literature (ranging from λ/16 to λ/8)

4.3.2 Antenna Characteristics and Layout

Once the material characteristics were chosen, physical design of the antenna was made to obtain the following important parameters:

1. Size of the aperture ($D_x \times D_y$) to meet the gain and efficiency requirement,

2. Feed horn type to ensure maximum illumination of the array (Section 3.3), location (taking into account the impact of *f*/*D* over the bandwidth) and

selection of a support mechanism that will minimize the aperture blockage, and

3. Unit cell size or element separation and number of cells. These values must be chosen carefully to meet the beamwidth requirements (as discussed in Section 3.5). Also, to minimize mutual coupling between elements, the spacing between the edges of adjacent patches should be at least a quarter wavelengths.

For this chapter, an *f*/*D* of 0.66 was selected and the feed-horn was placed at the center of the arrays. For the 10 GHz reflectarray, the standard X-band horn with $\rho_1 = \rho_2 = 2.3\lambda$ (6.9 cm), $a_1 = 1.5\lambda$ (4.5 cm), $b_1 = 1.6\lambda$ (4.8 cm), $a = 0.76\lambda$ (2.28 cm) and $b = 0.34\lambda$ (1.02 cm) was used as the primary source. The antennas was square arrays that measured 30 cm by 30 cm. Cell separation was $0.6\lambda_0$ along the *x*- and *y*-axes.

A rectangular lattice was used throughout this thesis. Using the axis convention previously shown in Figure 3.1, the reflectarray lied along the $X'Y'$ plane, with the center located at (0,0,0) cm. All of the elements were located at the center of their cells as illustrated in Figure 4.2. The feed-horn phase center was located at (0,0,19.91) cm.

4.3.3 Radiating Element Design and Phase Response Simulation

Once the above two steps were completed, the important design of the radiating elements was performed. First, a theoretical calculation of the microstrip elements width and length (Equation 4.1) was done using the theory presented in Section 4.2. Secondly, numerical analysis of the individual elements was conducted with developed tool to confirm the resonance and bandwidth of the element.

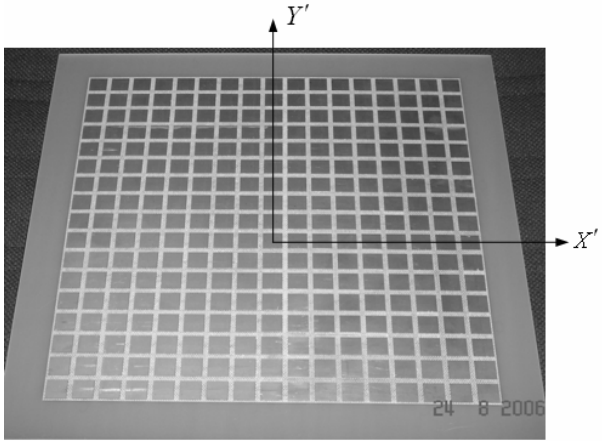

Figure 4.2 Typical reflectarray layout.

Subsequently, numerical analysis of the microstrip patch when used within an array was conducted. Conventional microstrip arrays analysis is performed using the full-wave numerical methods discussed in Section 3.7 in combination with techniques such as infinite array analysis and active element pattern. The microstrip element was illuminated by a TEM plane wave propagating perpendicularly to its surface and polarized along the length of the patch. Simulations were conducted for different element lengths and the derived reflection coefficients were recorded. In turn, these values were plotted with the resultant phase vs. length curve was expressed.

4.3.4 Element Length Calculations

After selection of the reflectarray's characteristics and the design of the radiating element, the next step consists in calculating the required phase delay for each element (as discussed in Section 3.6). This phase value required for each element was translated as a length using the phase vs. length curves. In the case where the required phase was unattainable, that element was not included in the array layout.

4.4 Broad-Beam Reflectarray Design and Fabrication

To validate the theory and methods presented in this thesis, a case-study linearly-polarized reflectarray, operating at 10 GHz and using square patch elements, was designed and tested. The broad-beam reflectarray was designed using the procedure in Section 4.3. Besides, its prototype was also constructed and tested. By testing the reflectarray, a differential measurement can be conducted, and the performance effects common to proposed antennas can then be readily calibrated out. This yields high-precision measurements of the impact of the effects of interest on the reflectarray performance. The relevant details of this antenna design including its predicted and measured characteristic are discussed in Section 4.5.

Before the reflectarray is fabricated and measured, it is prudent to simulate and validate the design. As discussed in Section 3.8, a small square reflectarray was created and simulated. It is comprised of 17×17 patch elements (N = 17) located on a 30×30 cm square area. The reflectarray is then designed to produce collimated radiation, and have identical dimensions (whenever applicable). As a practical example, we have chosen the parabolic backscatter function because it has appropriate characteristics i.e. low ripple level, high relative power (high gain), and wide HPBW (wide coverage area). To verify the theoretical calculation, the reflectarray prototype is fabricated at the operating frequency of 10 GHz due to corresponding to the available equipment.

In order to minimize the dielectric losses, a substrate of thickness d = 0.787 mm and relative permittivity ε_r = 2.33−j0.0009 were selected (Taconic TLY-3). The both sides of selected substrate are coated with thin copper sheets that the individual thickness (t) is 17 μm. The coated copper sheet on the back side was

served as the ground plane, while the copper on the front side was etched to form the reflectarray elements.

4.4.1 Phase Delay of Reflectarray using Parabolic Backscatter Function

The required phase delays that related to the patch position, are determined for beam shaping of reflectarray as shown in Figure 4.3 with various center frequencies (f_0 = 10 GHz). These phases are duplicated the same radiating aperture as shape of the parabolic backscatter. In the design, a standard X-band horn is functioned to be the primary feed and located at distance f = 19.91 cm.

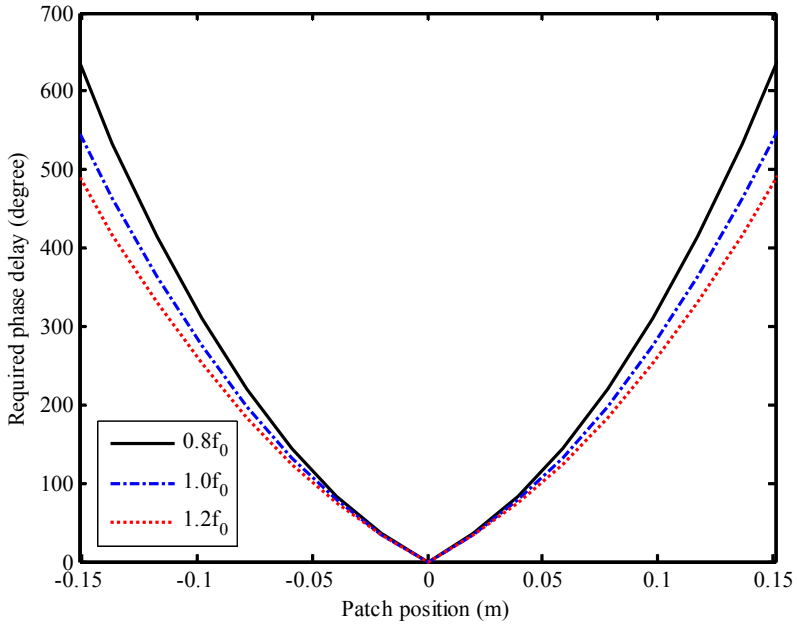

Figure 4.3 Calculated results of desired reflection phase properties

4.4.2 Reflection Coefficient Phase versus Patch Length

These element designs were subsequently simulated with the numerical tools developed in Chapter 2 which is used to study the effect of the size L of any particular element on its reflection coefficient. The parameters are set to

$f_0 = 10$ GHz, $\varepsilon_r = 2.33$, $d = 0.787$ mm, $s = 0.6\lambda_0$, and $\theta_i = 0°$. Also, the phase response by the infinite array is reported in Figure 4.4 as functions of the tuning patch length. Because of the rapid phase change around resonance, most reflectarray elements have lengths within ±5% of the nominal resonant length L_0 (L_0 is the length of patch elements of reflectarray at reflection phase 180°). In this case, a total achievable phase range of 320º was obtained which corresponds to the theoretical unachievable phase shift of 40º.

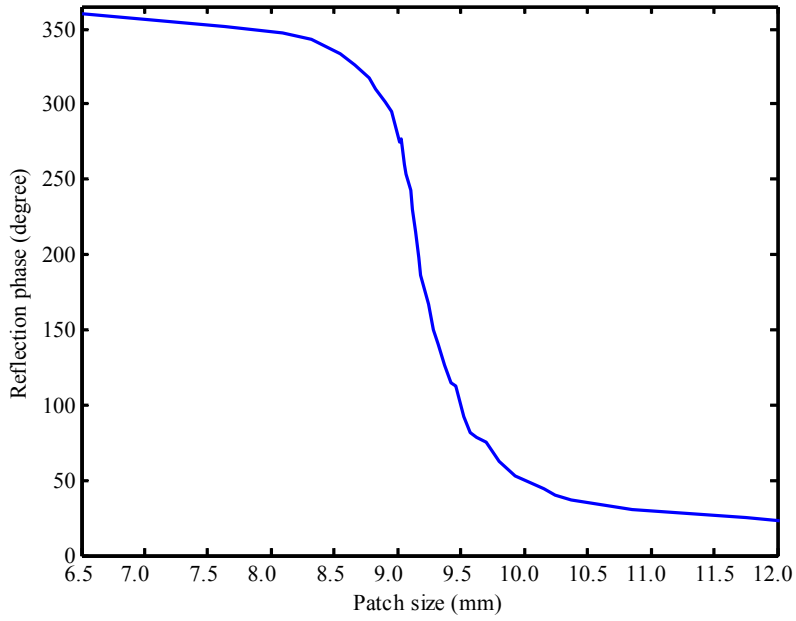

Figure 4.4 Reflection coefficient phase versus tuning length (L) at $\theta_i = 0$ and $\phi_i = 0$.

4.4.3 Broad-Beam Reflectarray Fabrication

After the shaped backscatter was designed, the reflectarray elements layout was determined. We started by considering a possible values of grid spacing, $s = 0.6\lambda_0$@10 GHz, and an infinite array of uniform square patch elements, etched on the substrate as previously described. In order to assure the required 0º−360º reflection

coefficient phase coverage the elements' characteristic, therefore the dimension L should be as large as possible. We have selected L_0 = 9.777 mm for the case of $s = 0.6\lambda_0$. This is the possibly largest values that still keep a reasonable space between adjacent elements.

The curve at $\theta_i = 0°$ depicted in Figure 4.4 indicates that any phase $\angle\Gamma$ value between $\angle\Gamma_{\min} = 34.02°$ and $\angle\Gamma_{\max} = 354°$ can be implemented by changing L from 6.5 to 12 mm, respectively. Then, the desired reflection coefficient phase, $\angle\Gamma_i$, and the required patch length L_i of each ith unit cell, can be evaluated. This yields the desired reflection coefficient phase $\angle\Gamma_i$, in their corresponding unit cells. It also yields the patch length L_i. Using these L_i values the layout mask for the 10 GHz reflectarray antenna was produced. Details of this mask are shown in Figure 4.5.

The prototype reflectarray is fabricated by PCB prototype machine as illustrated in Figure 4.6. Each patch element on the antenna has varying size for providing the desired field pattern. The aperture shape of a reflectarray is a square with 17×17 of unequal patch sizes, which are built on a 0.787 mm TACONIC TLY-3 substrate (ε_r=2.33). The centre-to-centre elements spacing is fixed at a value $s = 0.6\lambda_0$ in both x- and y-directions. The phase adjustment is controlled by the patch size. The primary feed used in the design, is a standard X-band pyramidal horn, which is placed at the selected distance f = 19.91 cm and an incident angle $\theta_i = 0$.

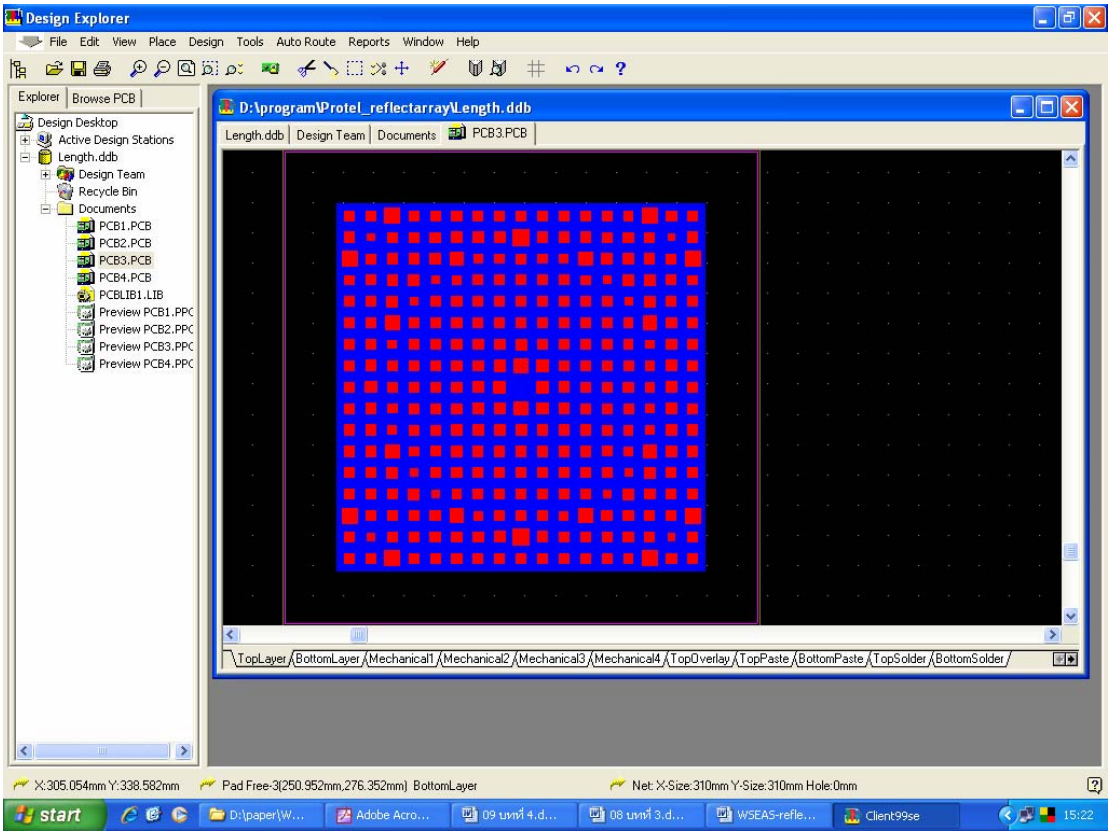

Figure 4.5 Layout mask for the 10 GHz reflectarray antenna.

Figure 4.6 PCB prototype machine.

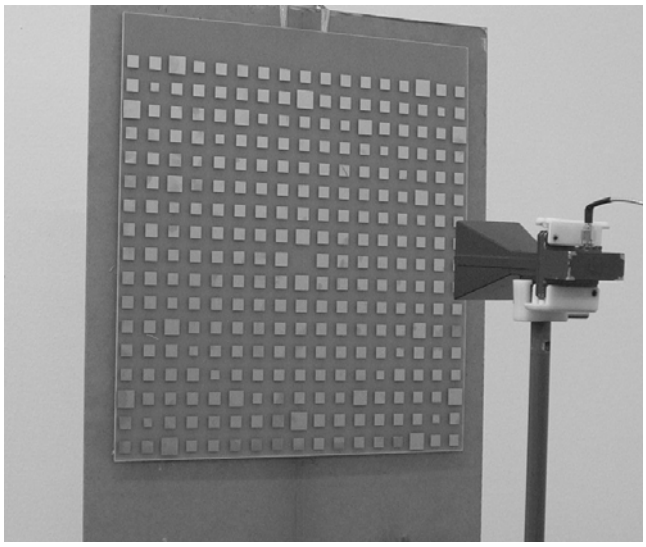

Figure 4.7 Reflectarray antenna prototype.

4.5 Antenna Measurement

4.5.1 Far-Field Distance

The evaluation of the key antenna parameters such as radiation pattern, directivity, and gain can be performed in an outdoor or indoor antenna ranges, in either the near-field or far-field of the Device Under Test (DUT) (Balanis, 1997). In the far-field measurements, the DUT is illuminated by a uniform plane wave. This requirement is achieved when the distance between the DUT and Tx, included distance *R*, meets the far-field criterion given by Equation (4.2). This is also called the Rayleigh distance, where *D* is the largest dimension of the DUT as viewed from the measurement point.

$$R \geq 2\frac{D^2}{\lambda} \tag{4.2}$$

In general, there are two basic types of far-field antenna ranges such as reflection and free space ranges (Wiley-Interscience, 1979). Of these, the most accurate far-field antenna range is an indoor anechoic chamber (Evans, 1990). The reflection errors are minimized by lining the walls of the chamber with radar absorbing material, and its shielding properties prevent external RF energy to enter the chamber. Nevertheless, the usage of this far-field chamber is limited by the physical size of the DUT and the lowest usable frequency.

To measure the performance of an antenna, we focused to three fundamental parameters such as the radiation pattern, the HPBW, and the gain of the antenna (DUT).

4.5.2 Radiation Pattern

The antenna radiation pattern is the display of the far-field radiation properties of the antenna in spherical coordinates at a constant radial distance and frequency. In general, this pattern is three-dimensional, however, because it is not practical to measure this, a number of two-dimensional patterns, or pattern cuts, are recorded by fixing one angle and varying the other (Balanis, 1997).

Testing of the reflectarrays was conducted using the far-field anechoic chamber, which is depicted in Figure 4.8. The maximum antenna dimension of the reflectarrays was within the chamber, thus ensuring that the far-field conditions are met as Equation (4.2). Within the chamber, a transmitting pyramidal horn antenna is fixed at a certain position, while the reflectarray (in receiving mode) is mounted with pyramidal horn antenna also. The reflectarray eith feed horn is installed on a turntable with the Raleigh distance R far from transmitting antenna. During the measurements, the reflectarrays were illuminated with a uniform plane wave and their receiving

characteristics were measured. Azimuth plane measurements, or H-plane patterns in this configuration, were taken as previously illustrated in Figure 4.8. Specifically, θ was fixed at 90° and ϕ was varied from 0° to 180°, or using the convention of the plotting software, ϕ was varied from -90° to +90°.

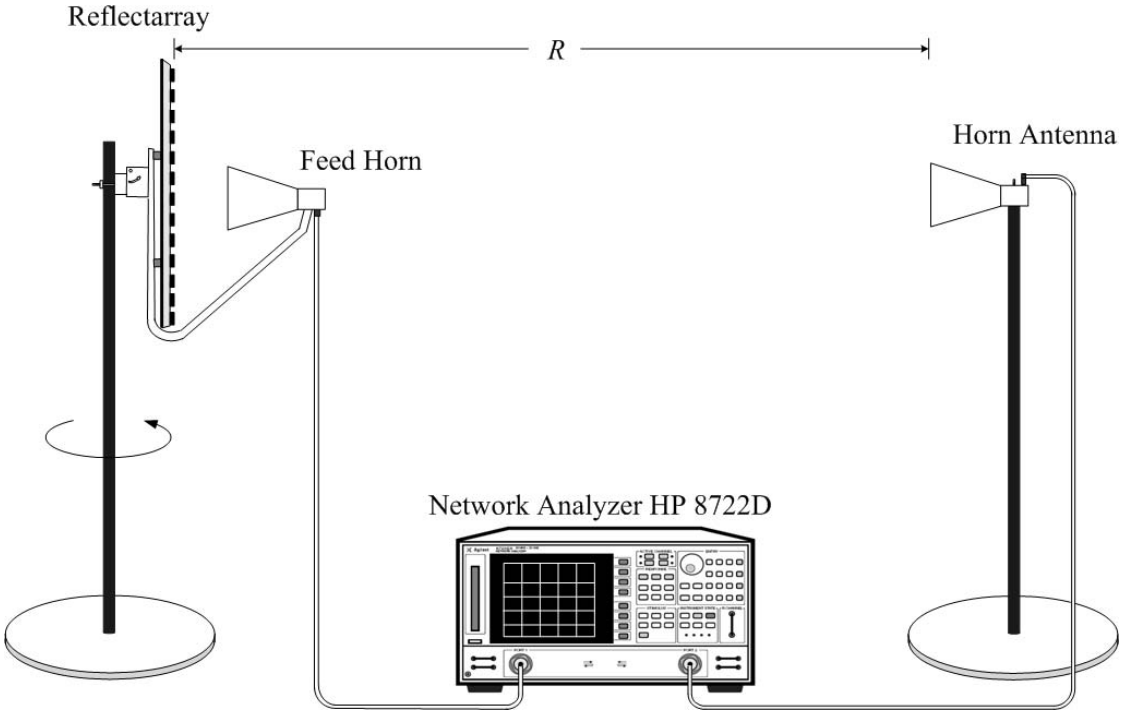

Figure 4.8 Measurement set up of the radiation pattern.

4.5.3 Gain

The power gain of an antenna in a given direction is the ratio of the power radiated by the antenna in that direction to the power which would be radiated by a lossless isotropic radiator with the same power accepted as input. There are two basic methods to measure the gain of an antenna: absolute gain and gain comparison technique (Balanis, 1997). For either method, the theory is based on the Friis

transmission formula Equation (4.3), which can be applied when two polarizations matched antennas aligned for the maximum directional radiation, and separated by a distance R that meet the far-field criteria, are used for the measurements.

$$G_{r_{dB}} + G_{t_{dB}} = 20\log\frac{4\pi R}{\lambda} + 10\log\frac{P_r}{P_t}, \tag{4.3}$$

where

P_r is the measured power received (W)

P_t is the measured power transmitted (W)

G_r is the gain of the receiving antenna

G_t is the gain of the transmitting antenna

The absolute gain method requires no a priori knowledge of the transmitting or receiving antenna gain. If the receiving and transmitting antennas are identical, only one measurement is required and Equation (4.3) can be simplified to Equation (4.4).

$$G_{r_{dB}} = G_{t_{dB}} = \frac{1}{2}\left[20\log\frac{4\pi R}{\lambda} + 10\log\frac{P_r}{P_t}\right] \tag{4.4}$$

The gain comparison method, or direct comparison method, commonly used in antenna ranges. Since ideal isotropic antennas is the most not exist, recalibrated standard gain antennas are used to determine the absolute gain of the DUT. With this method, two identical standard gain horns are used as transmitting and receiving antennas. Pyramidal horns are most often used (Balanis, 1997). The received signal level ($P_r = P_s$ where the subscript s is used to designate values measured by the

standard gain horn) is stored over the frequency of interest, and, since the two horns are identical, the result of Equation (4.4) is compared with the gain table of the manufacturer (G_s). This allows confirming the operation of the Tx horn as well as the entire receiving components. Secondly, the receiving standard gain is replaced by the DUT and the measurements resume using the same geometrical arrangement and power level. In those conditions (Wiley-Interscience, 1979), it can be shown that Equation (4.4) can be reduced to Equation (4.5). This implies that by using this method, one can find the gain of the DUT, G_r by simply adding or subtracting the difference in signal level to the gain value of the standard horn.

$$G_{r_{dB}} = G_{s_{dB}} + 10\log\frac{P_r}{P_s} \tag{4.5}$$

where P_s is the measured power previously received by the standard antenna (W) and G_s is the gain of the previously measured standard antenna, respectively.

4.5.4 Bandwidth

The bandwidth of an antenna is defined literally as the range of usable frequencies within which the performance of the antenna conforms to a specified standard and may be limited by impedance mismatch or pattern deterioration. However, there are new bandwidth enhancement techniques to overcome the limited operational bandwidth of the patch antenna. The bandwidth can be the range of frequencies on either side of a center frequency where the antenna characteristics like input impedance, pattern, beamwidth, polarization, side lobe level, gain, beam direction or radiation efficiency, are within an acceptable value of those at the center frequency (Balanis, 1997).

For narrowband antennas, the bandwidth is expressed as a percentage of the frequency difference (upper minus lower) over the center frequency of the bandwidth. Equation (4.6) is the fundamental formula to calculate the bandwidth of the antenna from the return loss versus the frequency plot.

$$\text{Bandwidth } (\%) = \left[(f_{upper} - f_{lower}) / f_0 \right] \times 100\% \tag{4.6}$$

The antenna in this thesis is computed by using pattern bandwidth, which is separately considered in E- and H-planes.

4.5.5 Antenna Efficiency

The antenna efficiency is defined as the ratio of total power radiated by the antenna to the input power of the antenna. Just like any other microwave components, an antenna may dissipate power due to conductor loss or dielectric loss.

4.6 Experimental Results

The measured far-field patterns in H- and E-planes for the test antenna at the resonant frequency of 10 GHz are illustrated in Figure 4.9. This figure shows the comparison with the respective theoretical patterns computed as the superimposition of the fields radiated by the array elements when the correct incident angles are considered. The prescribed field requirements have been satisfied by an appropriate choice of the radiating patches selected from the complex design curves obtained in the analysis stage. The coverage angle of the antenna is about 120°. Outside this range, the radiation power drastically fall off. The dip in the pattern boresight of about 8 dB is caused by feed blockage. From the measurement as shown in Table 4.2, the

proposed antenna has the HPBW, maximum gain, and bandwidth in H-plane of 165°, 9.84 dB, and 3.8%, respectively, and in E-plane of 132°, 8.54 dB, and 4.2%, respectively. However, the measured and computed radiation patterns that were taken along the strut show a relatively much larger ripple of almost 3 dB in amplitude. The antenna in this thesis is built at least a range of 4% pattern bandwidth around the center resonant frequency with the requirement acceptable looking at around the maximum gain of –3 dB cutoff magnitudes.

The curves shown in Figure 4.9(a)-(b) could be used to predict the area of uniform coverage. If an imaginary plane was placed at a distance h from the antenna, the uniform coverage length along the x- and y-axes is $D_{c,max} = 2h \tan((\theta_2-\theta_1)/2)$. Here θ_1 and θ_2 are the lower and upper bounds of the elevation angle (in degree) satisfying the condition of uniform coverage, which could be read from Figure 4.11. For example, if the distance h is 3 m, the maximum uniform coverage along the x and y axes will be about 11 and 7 m, respectively, with θ_1 = -60º and θ_2 = 60º, and θ_1 = -48º and θ_2 = 48º, respectively.

Table 4.2 Characteristics of reflectarray prototype with parabolic backscatter function

Antenna characteristic	Simulation		Measurement	
	E-plane	H-plane	E-plane	H-plane
HPBW (degree)	136.8	140.0	132	164
Maximum gain (dBi)	8.49	10.65	8.54	9.84
Pattern bandwidth (%)	4.1	3.6	4.2	3.8

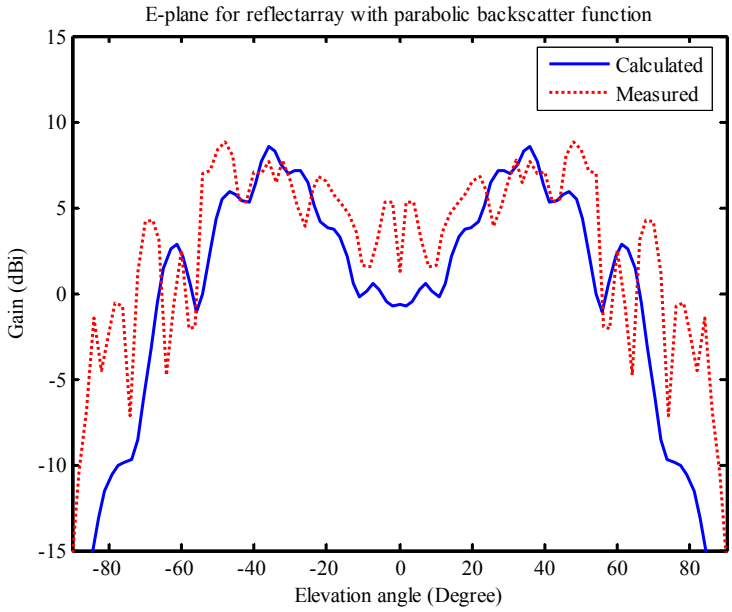

(a) E-plane

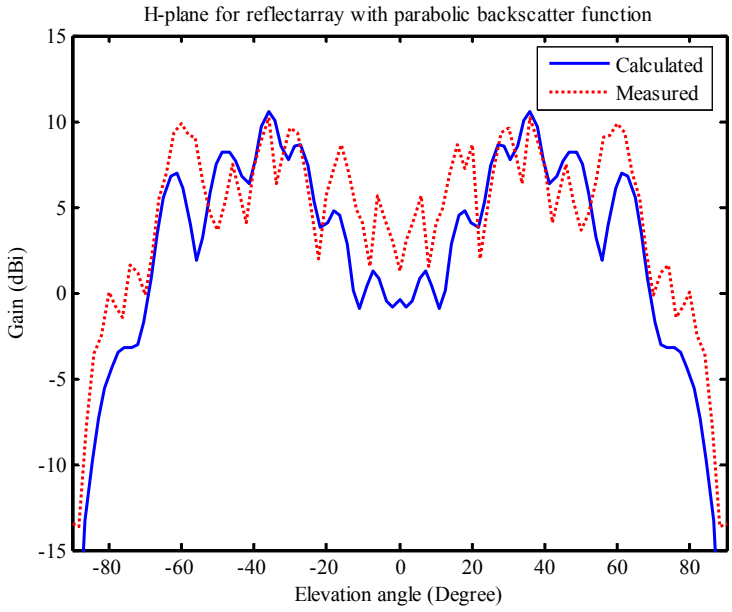

(b) H-plane

Figure 4.9 Measured and calculated gain patterns of the proposed antenna with parabolic backscatter function.

4.7 Chapter Summary

This thesis presents a method of moment treatment of the field scattered by an infinite uniform array of conducting elements on a single layer dielectric substrate, and this tool is used to generate the required element design data for implementing microstrip reflectarray. An effective and accurate step-by-step design methodology was developed for the broad-beam reflectarray considered. Using these tools, the reflectarray was designed, manufactured, and tested: a 10 GHz case-study reflectarray model using parabolic backscatter.

From experimental results on an X-band reflectarray prototype of 17×17 unequal square patches, the prescribed field requirements have been satisfied by an appropriate choice of the radiating patches array selected from the complex design curves obtained in the analysis stage. The coverage angle of the antenna is about 120°. Outside this range, the radiation power drastically fall off. This data show that flat reflectarrays can give as well a defined footprint as a conventional antenna but without the complicated tooling and other drawbacks inherent for the latter. All predicted gain results agree within less than 10.75 dB, except for the 10 GHz model. The predicted reflectarray efficiency was 60% (the theoretical limit). These results validate the design and analysis tools presented, as well as demonstrate their applicability for implementing broad-beam microstrip reflectarray antennas.

CHAPTER V

PERFORMANCE IMPROVEMENT OF BROAD-BEAM MICROSTRIP REFLECTARRAY

5.1 Introduction

This is a theoretical and experimental study of microstrip reflectarray useable in WLAN. This chapter proposes performance improvement for microstrip reflectarray antenna using parabolic backscatter function to form a wide beam antenna. The optimized feed distance is calculated from the aperture efficiency with considering feed blockage efficiency and has investigated the influence of the feed position on the -3 dB beamwidth and gain performance. Moreover, the effectiveness of reducing the unit cell size of microstrip reflectarray was investigated. A reflectarray with different element sizes and reduced grid spacing have been designed at 10 GHz. Having confirmed the validity of this approach, the X-band antenna prototype is designed and developed.

5.2 Optimum Feed Position of Broad-Beam Reflectarray

A parabolic backscatter function operating at 10 GHz and illuminated by a pyramidal feed horn was selected for the broad-beam reflectarray case study. The radiation pattern of this horn is given in Figure 3.2. It has been easy to calculate the aperture efficiency for a feed horn pattern and reflectarray due to taper illumination

and spillover efficiencies as given in section 3.3. However, there are several other factors that can significantly reduce efficiency. Because the feed horn and its supporting structures are in the beam direction of the reflectarray, therefore, some part of the radiation is blocked. Also, considering the aperture, taper, spillover, and feed blockage efficiencies relations versus distance between the feed and the reflectarray to a dimension (*f/D*) ratio are calculated and plotted in Figure 5.1. In case of front feed reflector, there is an optimum value of *f/D* that maximizes aperture efficiency for a given feed pattern. This maximum value is slightly lower than the optimum aperture efficiency for the parabolic case because of a slightly lower taper efficiency. When the feed blockage efficiency is considered, maximum aperture efficiency is reduced and feed distance is changed while a reflectarray dimension is fixed. In this section, we have investigated the influence of feed position on the -3 dB beamwidth (HPBW) and gain performance before the reflectarray will be fabricated, where the first feed distance *f* is located at point that maximizes aperture efficiency (at optimum value of aperture efficiency (61%), the feed distance is chosen to be of 21.25 cm at $10\lambda_0$ reflector diameter).

In order to optimize the feed position of broad-beam reflectarray, the calculated results as shown in Figure 5.2 indicate the different radiation patterns for the various feed positions. The total re-radiated field is computed as the summation of all contributions from each array element.

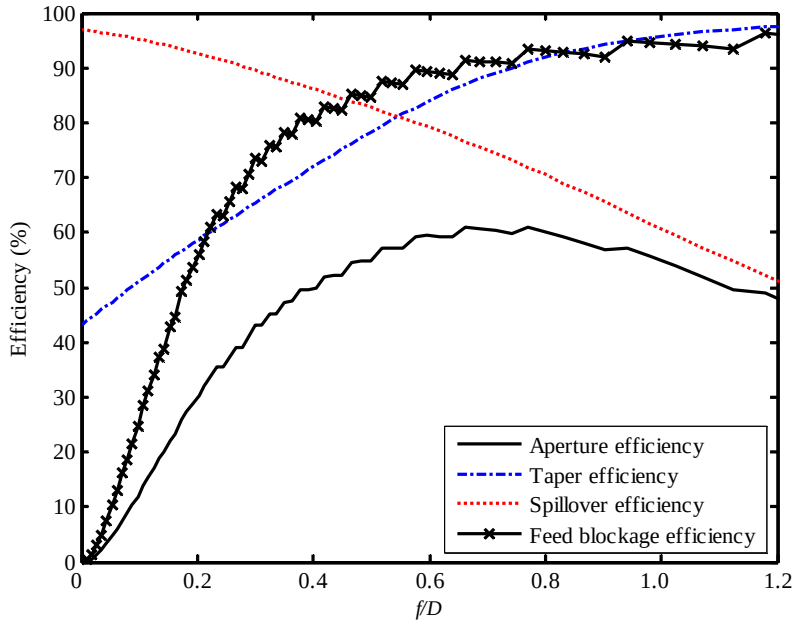

Figure 5.1 Reflectarray efficiencies versus *f/D* ratio.

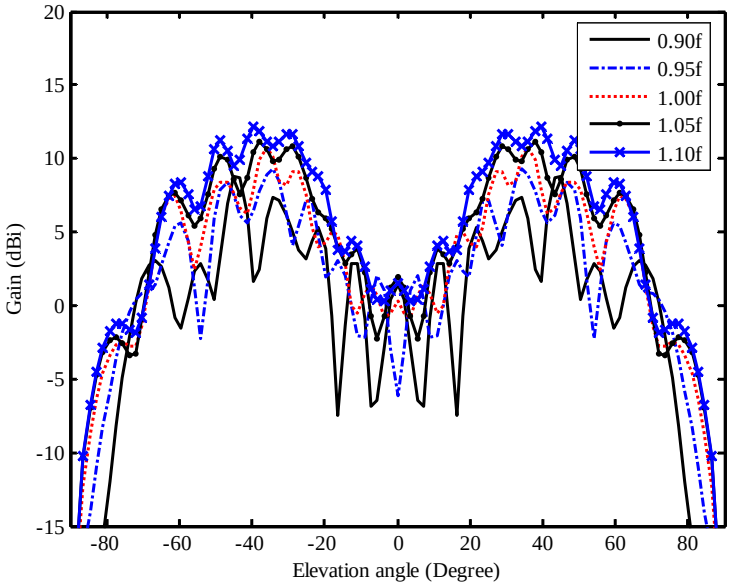

Figure 5.2 Radiation pattern in H-plane of broad-beam reflectarray for the various feed positions.

As reported in Table 5.1, the HPBW of reflectarrays are different when the feed distances are adjusted. For average consideration, it is apparent that the feed position not far away in distance from reflectarray provides the widest beamwidth. Since the maximum gain is strongly coincided with the HPBW i.e., the narrower the beamwidth the higher the maximum gain and vice versa. However, the reflection surface of reflectarray elements is placed at position near the centre of backscatter. Thus, the extension of the feed distance yields the lowest feed blockage efficiency and the highest gain at $\theta_i = 0°$.

Table 5.1 Simulation results of reflectarray with various feed positions

Feed distance	HPBW (degree)	Gain (dBi) at $\theta = 0°$	Maximum gain (dBi)
0.90f	158	1.43	8.81
0.95f	151	-6.13	9.35
1.00f	144	0.32	10.75
1.05f	144	1.99	11.10
1.10f	145	1.52	12.16

However, it is generally observed that when the antenna beam is enlarged, the antenna gain is reduced. With the optimum design requirement, the feed distance is chosen at 25 cm, which caused the maximum aperture efficiency to be reduced approximately 2% but its gain is increased. In Figure 5.3, the prototype of reflectarray antenna is realized following this approach and validated with measurment. From the measurement as shown in Figure 5.4, the HPBW and maximum gain of 145° and 13 dB, respectively, at the operating frequency 10 GHz. An additional cause of

asymmetry observed in the patterns is fabrication tolerance. The computed performances of this reflectarray are in good agreement with those of the measured prototype.

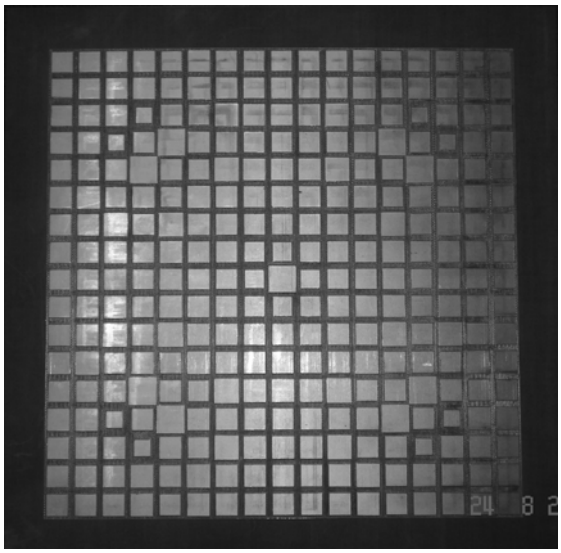

Figure 5.3 Reflectarray prototype at f = 25 cm.

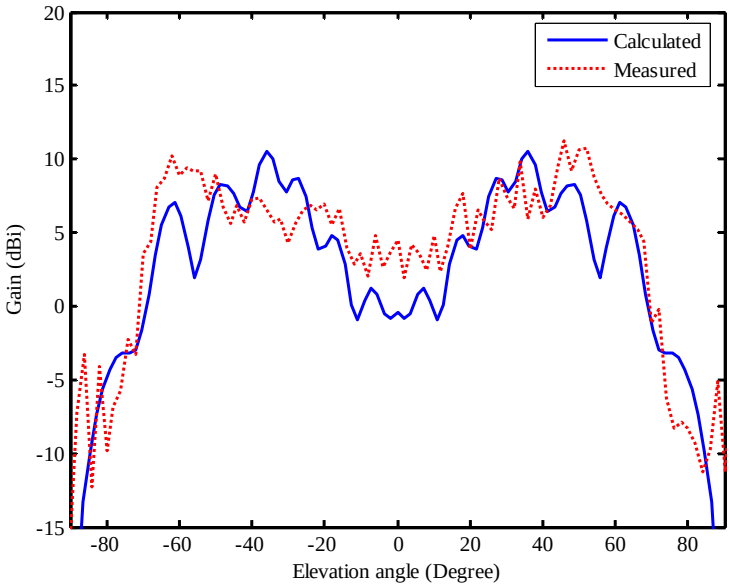

Figure 5.4 Calculated and measured radiation patterns of reflectarray at f = 25 cm.

5.3 Gain Improvement by Reduction of Elements Spacing

In the wireless communication applications such as the large-scale indoor base station for WLAN, it is desirable the wide-beam antenna for covering a broad area. In principle, we have an antenna, which is installed on the center point of ceiling in the very large room and can illuminate a predefined area for all client computers without substantial spatial variation. Consequently, the all client computers, which are in this room, will be connected to the access point of WLAN through the only one antenna. However, it is generally observed that when the antenna beam is enlarged, the antenna gain is reduced. In this section, we have investigated the influences of the unit cell size of reflectarray that affect to the gain performance.

5.3.1 Reduction of Elements Spacing

The effective method for decreasing the unit cell size is to print the element on substrate, which reduces the size of reflectarray element. In microstrip antenna, many techniques have been reported to reduce the size of reflectarray element at a fixed operating frequency (Kin-Lu Wong, 2002). In general, reflectarray elements are half-wavelength structures at reflection phase 180° and operated at a resonant frequency, which is given by

$$f_0 \cong \frac{c}{2L\sqrt{\varepsilon_r}}, \tag{5.1}$$

where c is the speed of light and ε_r is the relative permittivity of the grounded microwave substrate. From Equation (5.1), it is found that the physical unit cell size of reflectarray will be decreased at a fixed operating frequency due to the use of the microwave substrate with a higher permittivity.

5.3.2 Phase Characteristic Effect

As illustrated in Figure 4.3, because reduction of center-to-center element spacing changes the elements position, the phase delays are decreased. In Figure 3.13, the size reductions of unit cell elements on of reflectarray can reduce the slope of the phase response. For achieving reflectarray element with a reduced size at a fixed operating frequency, the use of a high-permittivity substrate is an effective method as shown in Figures 3.12 and 5.5.

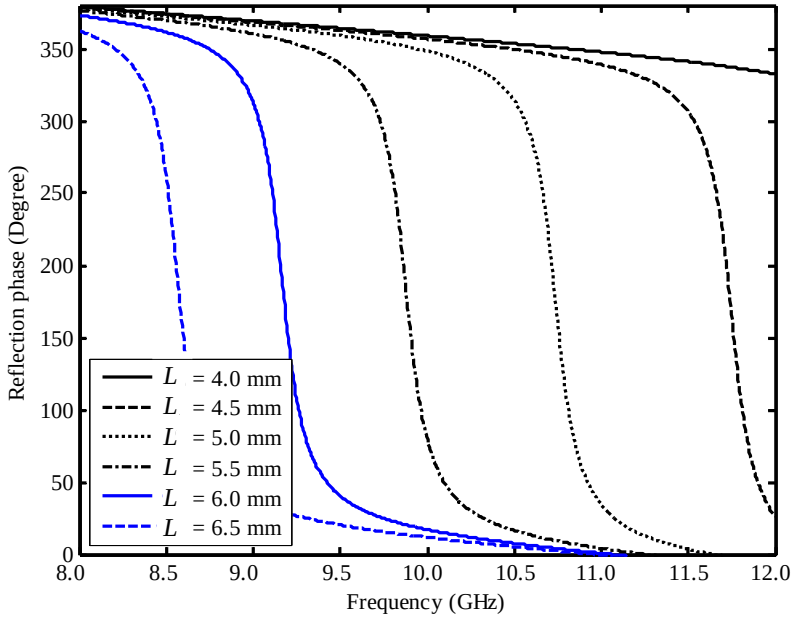

Figure 5.5 Simulated results of element characterization at $\varepsilon_r = 6.15$, $s = 0.6\ \lambda_0$.

5.3.3 Gain Improvement

The radiated fields of various unit cell sizes provide the radiation characteristics, which are represented in Table 5.2 and Figure 5.6. Because of phase change versus element change, each unit cell size provides different characteristics such as HPBW and gain performance. The maximum gain is increased due to

reduction of grid spacing. Thus, the HPBW is decreased and followed by the same order as the maximum gain. Figure 5.7 shows maximum gain and gain at elevation angle 0° with different unit cell sizes.

Table 5.2 Simulation results of reflectarray with various unit cell sizes

Unit cell size (wavelength)	HPBW (degree)	Maximum Gain (dBi)
0.3	122	22.61
0.4	126	19.27
0.5	142	15.54
0.6	146	11.88
0.7	152	11.33

To verify the theoretical calculation, the experiment was set up at the operating frequency of 10 GHz. The prototype antenna was fabricated and its photograph is shown in Figure 5.8. We have investigated and compared the measured performances of reflectarrays with $0.3\lambda_0$ and $0.6\lambda_0$ unit cell sizes, respectively. The selected substrate is TACONIC of 0.762mm thickness and dielectric constant 2.33 for $s = 0.6\lambda_0$ and 6.15 for $s = 0.3\lambda_0$, respectively. The compensations of phase range for unit cell size as shown in Figure 5.9 are of 348° for $0.6\lambda_0$ and 325° for $0.3\lambda_0$, respectively.

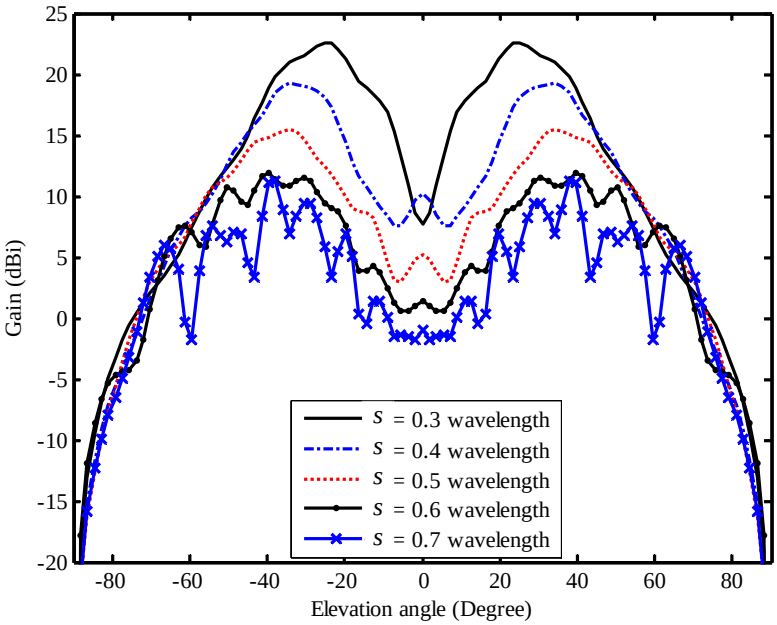

Figure 5.6 Radiation pattern with various unit cell sizes.

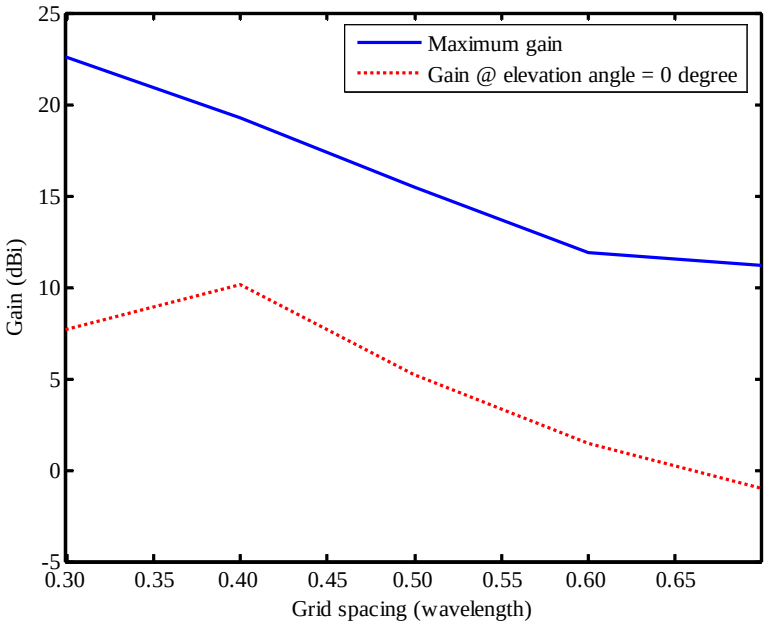

Figure 5.7 Gain versus unit cell size.

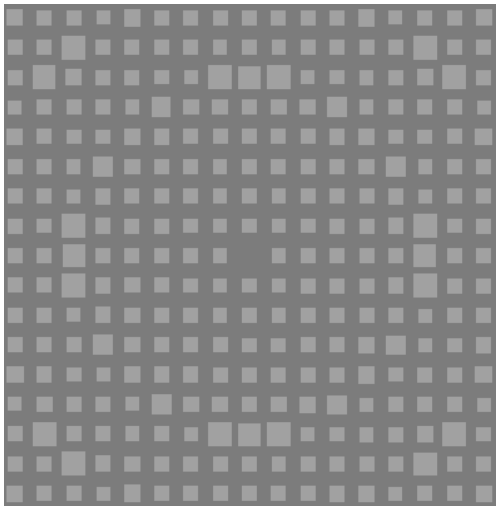

s = 0.6 λ_0, 17×17 elements

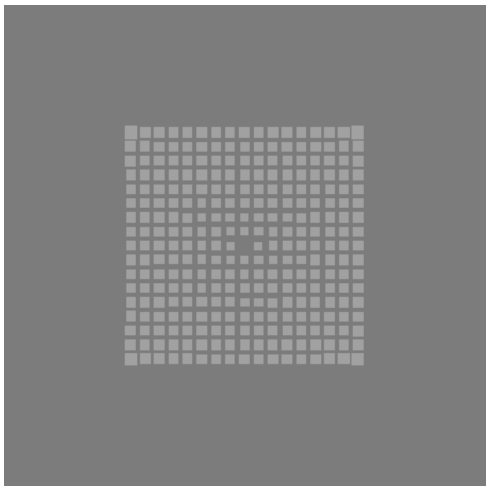

17×17 elements

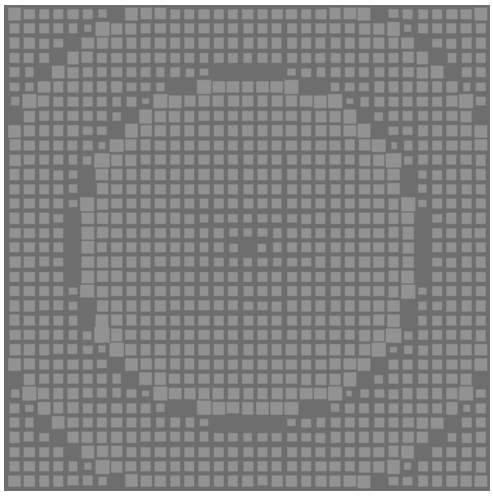

33×33 elements

(b) s = 0.3 λ_0

Figure 5.8 Photograph of the reflectarray antenna with various unit cell sizes and array sizes.

The measured far-field patterns in H- and E-planes for the testing antenna at the resonant frequency of 10 GHz are illustrated in Figure 5.10. These figure show the comparison with the respective theoretical patterns computed as the superimposition of the fields radiated by the array elements when the correct incidence angles are considered. Because of the feed blocking effect and the coupling between primary the source and the reflectarray by simulation are neglected, therefore, the dip in pattern boresight from measurement of around 4 dB are occurred. Nevertheless, we found that the ripple appears on the envelope of measured patterns, which are caused from some multipath effect that provided by construction of feed horn and metallic masts. Furthermore, if we compare the average levels on the all curves of each plane in far angle region, it will be observed that a difference from measured pattern on the order of 2 dB approximately for numerical result. However, the agreement between simulated and measured results is satisfactory.

On this reflectarray (17×17 elements) with different element dimensions are fixed. The effect on unit cell size reduction was considered with the same aperture dimension. Because the size of reflectarray is probably small, therefore, the number of rings (one ring is phase range of 360º) with missing phase values equal to only one ring, thus their effect is decreased. From the measurement reported in Tables 5.3 and 5.4, the verification between simulation and experiment has been presented in the parameters of maximum gain and HPBW. It is obvious that the effects from measurement in case of the broad-beam pattern improvement are the same as the effects from simulation. The improvement of maximal gain is of about 9 dB for the reduction of unit cell size from $0.6\lambda_0$ to $0.3\lambda_0$. The maximum gain of simulated results by using $0.6\lambda_0$ unit cell size in E-plane and H-plane patterns are

higher than measured results around 0.05 dB and 0.81 dB, respectively, while the maximum gain of simulation by using $0.3\lambda_0$ unit cell size are higher than measured results around 1.14 dB and 0.94 dB, respectively. Besides that the measured results of HPBW are wider than the simulated results around 5º in E-plane and 13º in H-plane for $0.6\lambda_0$ unit cell size and around 21º in E-plane and 12º in H-plane for $0.3\lambda_0$ unit cell size. Therefore, it can be summarized that the maximum gain and HPBW between simulated and measured results can show some minor differences both in E-plane and H-plane pattern.

The larger size of new reflectarray (33×33 elements) at $s = 0.3\lambda_0$ has been made and tested to confirm the improvement method of antenna performances. The number of uncorrected rings increases in comparison to the smaller array size as shown in Figure 5.8(b). The comparison results of radiation pattern of the improving antenna are plotted in Figure 5.11. It is obvious that improving HPBW by increasing the elements of reflectarray but still fixed its aperture dimention, thus it is caused the gain of antenna increasing about 2 dB.

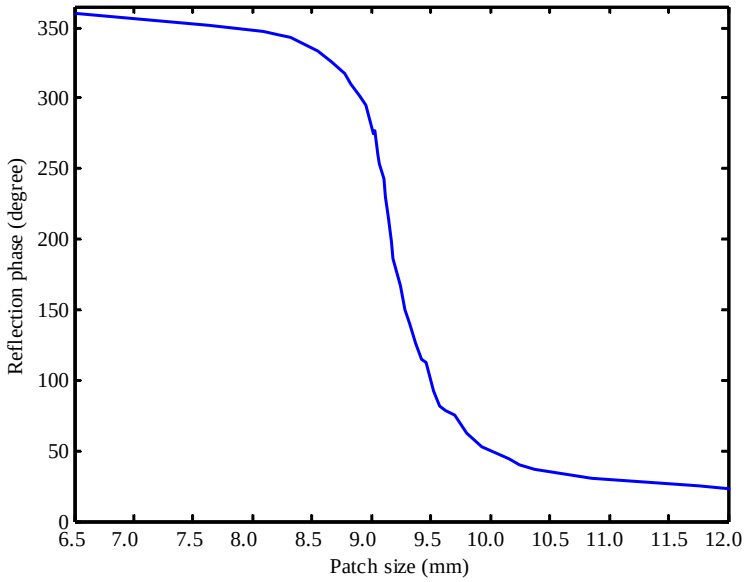

(a)

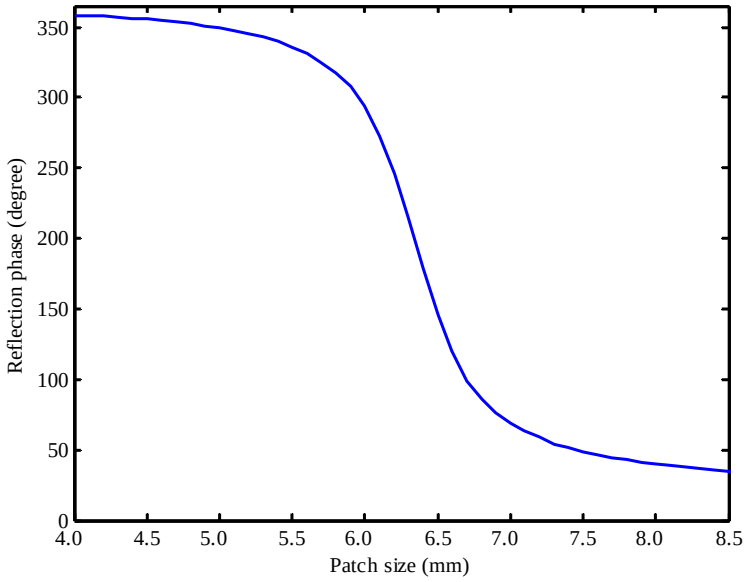

(b)

Figure 5.9 Reflection coefficient phase versus patch size (L):

(a) at $s = 0.6\ \lambda_0$, (b) at $s = 0.3\ \lambda_0$.

Table 5.3 Comparison of simulated and measured results for E-plane antenna characteristics with various unit cell sizes

Antenna characteristics	Simulated	Measured
Maximum Gain (dBi)		
$s = 0.6\lambda_0$, 17×17 elements	8.49	8.44
$s = 0.3\lambda_0$, 17×17 elements	19.04	17.90
$s = 0.3\lambda_0$, 33×33 elements	18.62	19.14
HPBW (degree)		
$s = 0.6\lambda_0$, 17×17 elements	137	132
$s = 0.3\lambda_0$, 17×17 elements	105	84
$s = 0.3\lambda_0$, 33×33 elements	108	116

Table 5.4 Comparison of simulated and measured results for H-plane antenna characteristics with various unit cell sizes

Antenna characteristics	Simulated	Measured
Maximum Gain (dBi)		
$s = 0.6\lambda_0$, 17×17 elements	10.65	9.84
$s = 0.3\lambda_0$, 17×17 elements	19.94	19.00
$s = 0.3\lambda_0$, 33×33 elements	20	20.54
HPBW (degree)		
$s = 0.6\lambda_0$, 17×17 elements	151	164
$s = 0.3\lambda_0$, 17×17 elements	112	100
$s = 0.3\lambda_0$, 33×33 elements	125	120

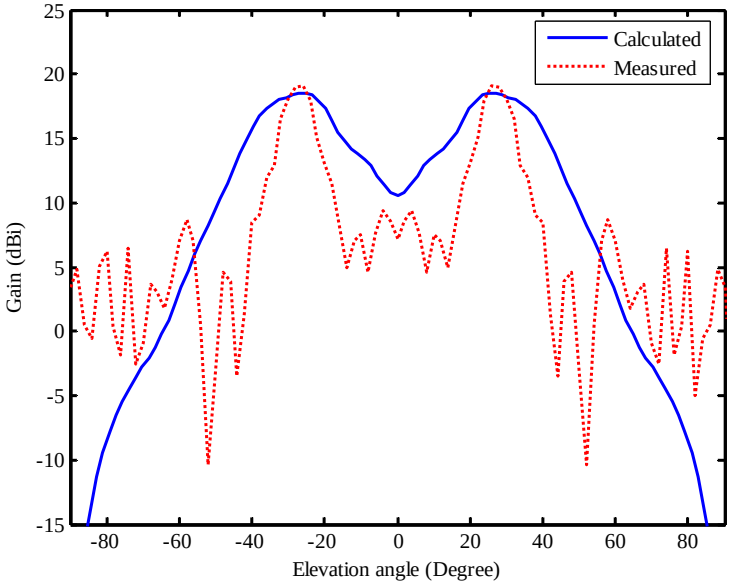

(a) E-plane

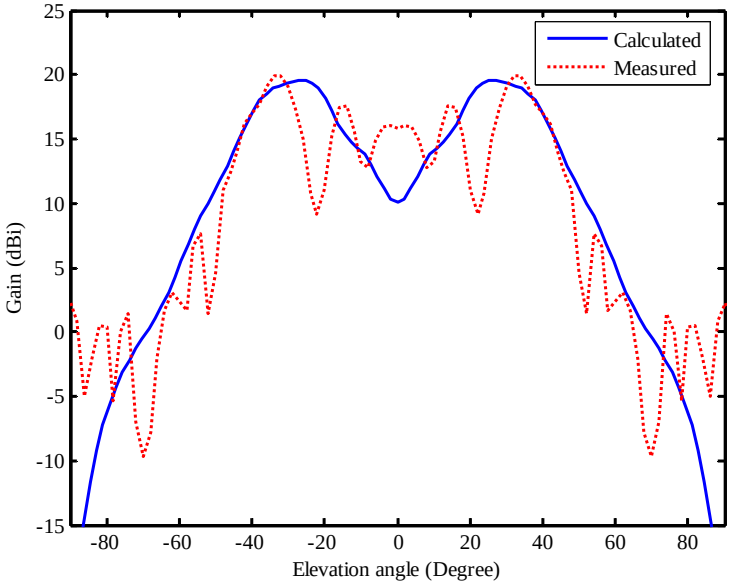

(b) H-plane

Figure 5.10 Gain patterns of the 17×17 elements with $s = 0.3\lambda_0$.

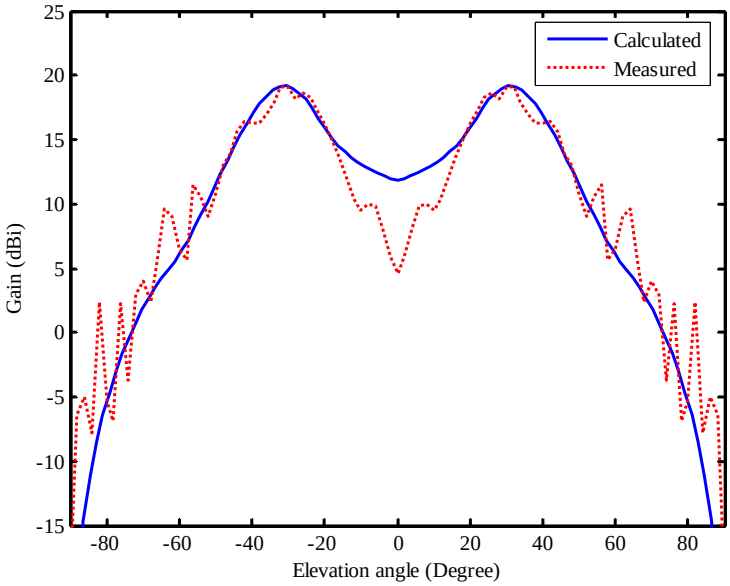

(a) E-plane

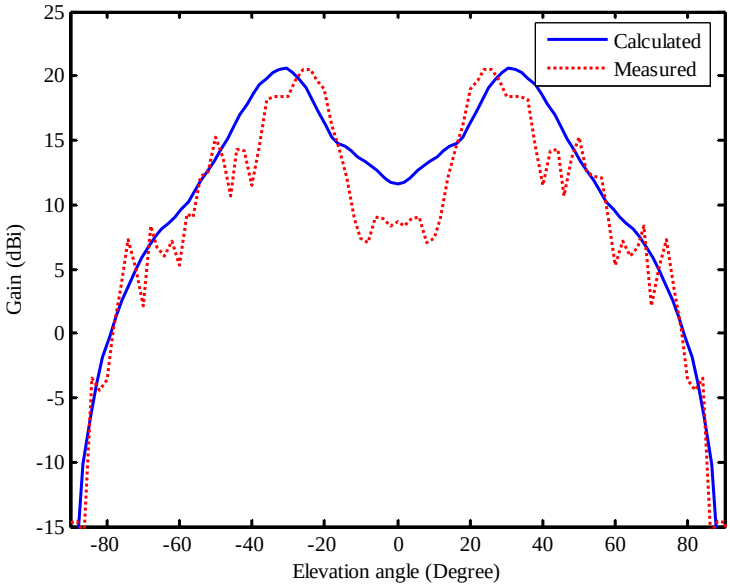

(b) H-plane

Figure 5.11 Gain patterns of the 33×33 elements with $s = 0.3\lambda_0$.

5.4 Chapter Summary

The performance improvement for a broad-beam microstrip reflectarray designed from square patches has been presented. An effective technique for optimum reflectarray design is to use the aperture efficiency with considering feed blockage efficiency and has investigated the influence of the feed position on the -3 dB beamwidth and gain performance. Simulation of this reflectarray demonstrates that increasing of feed distance can enhance maximum gain but its HPBW is reduced. From all the aforementioned of radiation characteristics, it can be summarized that if we need to improve gain performance for broad-beam reflectarray antenna, an optimum feed distance would provide a feed radiation pattern, which completely illuminates the reflectarray with minimal spillover.

Furthermore, the simulation demonstrates that reduction of unit cell size can enhance the bandwidth or reduce the slope of reflection phase. In addition, the maximum gain is improved with small change in HPBW. A testing antenna has been built according to our model is in good agreement with our expectations both in regards to coverage and maximum gain.

CHAPTER VI

CONCLUSIONS

6.1 Thesis Concluding Remarks

Analysis, modeling, and radiation characteristics of reflectarray antenna with application to WLAN and small LEO satellite have been addressed in this thesis. An approach for generating a broad-beam microstrip reflectarray with variable sizes of square microstrip elements fed by a linear feed-horn was presented, designed, fabricated and tested. Reflectarray antenna employs the flat main reflector that reduces any complication in the manufacture. Furthermore this antenna can be made of the light and compact materials.

First, the requirements that motivating this research were explained in Chapter 1 and a review of the antenna theory as it relates to this thesis was conducted in Chapter 2. In addition, we introduced a generalized scattering formulations based on method of moment. This foundation served to introduce the reflectarray theory and its design considerations were subsequently elaborated in Chapter 3. We have already shown broad-beam microstrip reflectarray design that the scattering implementation can be established. In particular, we have demonstrated that this implementation is very versatile in geometries where interactive radiation between scatterers takes place. We have applied scattering formulations to many backscatter geometries and selected the parabolic geometry to be a model of antenna.

Following this analytical work, the results of the experimental portion of this thesis were presented in the following chapter. Specifically, Chapter 4 presented a reflectarray design methodology, which was followed by detailed derivations of the design values for a reflectarray fabricated in this thesis. This entailed the design of the microstrip square patches, simulation of the response of these elements in an array using MoM and the derivation of the equations representing the phase versus length curves. In turn, the length of the printed elements, which is varied from patch to patch, was selected to produce a plane wave. The fabrication process was also briefly presented before discussing the experimental results. Finally, Section 4.6 presented the far-field measurements, which were conducted in an anechoic chamber. Various testing configurations were implemented and the gain measurements were recorded. Beside, an in depth discussion of these results has been done in this chapter. In addition, comparison of the achieved efficiency with other designs found in the literature was discussed and suggestions for the improvement of the performance were presented.

The work conducted in this thesis was aimed at fabricating broad-beam reflectarray with microstrip square patches, which were arranged in a non-overlapping configuration in the X-Band (10 GHz). To illuminate the reflectarray, a linear feed-horn was placed at the focal point and its orientation was set along the diagonal direction defined by the microstrip patches. The phase delay appearing on each patch of reflectarray was calculated using the phase equations.

Based on the results achieved in this thesis, it can be concluded that this reflectarrays concept is a viable option to meet the demanding customer antenna design requirements of WLAN and small LEO satellites constellations as it offers a

good design alternative for high-gain antenna while avoiding the high losses associated with microstrip arrays and the size of reflector antennas. In addition, flat reflectarrays can give as well a defined footprint as a conventional antenna but without the complicated tooling and other drawbacks inherent for the latter.

6.2 Remark for Future Studies

The reflectarray development and application had not been widely adapted until about the mid 1990s when the printable microstrip reflectarray was introduced. Except for its narrow bandwidth characteristic, the reflectarray has many advantages over a parabolic reflector antenna type. The main beam of a reflectarray can be designed to tilt to a large angle from its broadside direction. Phase shifters can be implanted into the elements for wide-angle electronic beam scanning. For WLAN large-scale indoor base station and small LEO satellite applications, the reflectarray's flat surface allows the antenna to be made into a flat structure, and it is easier to maintaining its surface tolerance than a curved parabolic surface. Its flat surface also can be made of multiple flat panels for ease in folding into a more compact structure for launch vehicle stowage. Very accurate beam shape can be achieved with phase synthesis for Earth-contour beam-coverage applications. Due to these many capabilities, the door has just opened for the development, research, and application of printed reflectarray antennas. Two major areas that need continuing improvement of the reflectarray performance are its bandwidth and its radiation efficiency.

Based on the knowledge learned and acquired over the course of this study, it was felt that some recommendations for future reflectarray design should be presented. First, it is recommended that further analysis of the developed tool be

conducted in order to solve for the higher than designed frequency error. Comparison with other software and/or simulation methods like the Method of Moment should also be conducted. In addition, new phase curves for the patch attempted in the design should be conducted to verify that these curves were corrected and that the failure was in fact attributed to the fabrication error experienced.

At the end of this research, it was realized that a reflectarray design (Pozar, Targonski, and Pokuls, 1999) did not include in the antenna elements, which required a phase shift higher than the achievable range. In this thesis, these elements were included and made with the possibly longest length of dimension. This introduced phase error, which may have reduced its overall performance. In conjunction with this technique, new reflectarray design could be implemented on thicker substrates as an attempt to increase the bandwidth (BW) while acknowledging a larger unattainable phase length. Larger BW would, for example, overcome the problem experienced in the design, makes them more amenable for use in interlaced dual frequency antennas.

In addition to the taking steps to improve on the fabrication precision, the following five physical improvements should be attempted in the reflectarray designs: (i) after fabrication of the antenna, perform a precision cut of the excess material instead of using a guillotine cutting process. This latter cutting technique raised the edges of the antenna thus making it more difficult to achieve a desired $\lambda/30$ flatness which is required in order to ensure good antenna efficiency (Huang and Pogorzelski, 1998); and (ii) use of an offset feed-horn to minimize aperture blockage thus reducing losses.

Once the above techniques have been implemented and the overall reflectarray performance has improved, design of more advanced reflectarray antennas could be

done using the following techniques: (i) use of multiple layers described in Encinar (1996) to obtain individual elements that offer smoother phase transition curves thus increasing the bandwidth and reducing the impact of manufacturing imprecision; and (ii) use of an active array as the primary feed of a cassegrain antenna design thus theoretically enabling beam steering of the reflectarray.

Other important development of the reflectarray is the achievement of a shaped contour beam by using a phase-synthesis technique. This reflectarray was developed for a commercial application to provide Earth contour-beam coverage. Since a reflectarray generally has many thousands of elements, it thus has many degrees of freedom in design to provide an accurate and uniquely required contour beam.

REFERENCES

Amitay, N., Galindo, V., and Wu, C.P. (1972). **Theory and Analysis of Phased Arrays**, Wiley Interscience, New York.

Arpin, F., Shaker, J., and McNamara, D.A. (2004). Multi-feed single-beam power combining reflectarray antenna. **IEE Electronics Letters**. 40(17): 1035–1037.

Balanis, C.A. (1989). **Advanced Engineering Electromagnetics.** John Wiley & Sons. New York.

Balanis, C.A. (1997). **Antenna Theory Analysis and Design.** John Wiley & Sons. New York.

Berry, D.G., Malech, R.G., and Kennedy, W.A. (1963). The Reflectarray Antenna. **IEEE Transactions on Antennas and Propagation**. AP-11(1): 645–651.

Bialkowski, M.E., Robinson, A.W., and Song, H.J. (2002). Design, Development, and Testing of X-Band Amplifying Reflectarrays. **IEEE Transactions on Antennas and Propagation**. 50(8): 1065–1076.

Bialkowski, M.E. and Song, H.J. (2001). Dual linearly polarized reflectarray using aperture coupled microstrip patches. **Proc. IEEE Antennas and Propagation Society International Symposium**. 1:486-489.

Bialkowski, M.E. and Song, H.J. (2002). Investigations into a power-combining structure using a reflectarray of dual-feed aperture-coupled microstrip patch antennas. **Proc. IEEE Antennas and Propagation Society International Symposium**. 50(6): 841 849.

Bird, T.S., Kot, J.S., Nikolic, N., James, G.L., and Barker, S.J. (1994). Millimeter-wave Antenna and Propagation Studies for Indoor Wireless LANs. **Proc. IEEE Antennas and Propagation Society International Symposium**. 1: 336–339.

Bozzi, M., Germani, S., and Peregrini, L. (2004). A figure of merit for losses in printed reflectarray elements. **IEEE Antennas and Wireless Propagation Letters**. 3(1): 257–260.

Cadoret, D., Laisne, A., Gillard, R., Le Coq, L., and Legay, H. (2005). Design and measurement of new reflectarray antenna using microstrip patches loaded with slot. **IEE Electronics Letters**. 41(11): 623–624.

Chaharmir, M.R., Shaker, J., Cuhaci, M., and Ittipiboon, A. (2006). Broadband reflectarray antenna with double cross loops. **IEE Electronics Letters.** 42(2): 65-66.

Chaharmir, M.R., Shaker, J., Cuhaci, M., and Sebak, A. (2003). Mechanically controlled reflectarray antenna for beam switching and beam shaping in millimetre-wave applications. **IEE Electronics Letters.** 39(7): 591–592.

Chang, D.C. and Huang, M.C. (1995). Multiple Polarization Microstrip Reflectarray Antenna with High Efficiency and Low Cross-Polarization. **IEEE Transactions on Antennas and Propagation**. 43(8): 829–834.

Chang, T.N., and Suchen, H. (2005). Microstrip reflectarray with QUAD-EMC element. **IEEE Transactions on Antenna and Propagation**. 53(6): 1993-1997.

Chang, T.N., and Wei, Y.C. (2004). Proximity-coupled microstrip reflectarray. **IEEE Transactions on Antenna and Propagation**. 52(2): 631-635.

Clark, R.W., Huff, G.H., and Bernhard, J.T. (2003). An integrated active microstrip reflectarray element with an internal amplifier. **IEEE Transactions on Antennas and Propagation**. 51(5): 993-999.

Colin, J.M. (1996). Phased Array Radars in France: Present and Future. **Proc. IEEE Symposium on Phased Array Systems and Technology**. 1: 458–462.

Collin, R. E. (1990). **Field Theory of Guided Waves**. IEEE Press, New York.

Costanzo, S.,Venneri, F., Di Massa, C., Angiulli, C. (2003). A synthesis algorithm for microstrip reflectarrays design. **Proc. IEEE Antennas and Propagation Society International Symposium**. 1: 796–799.

Costanzo, S.,Venneri, F., Di Massa, C., and Angiulli, C. (2005). Improved form of a synthesis algorithm for microstrip reflectarrays design. **Proc. IEEE Antennas and Propagation Society International Symposium**. 1B: 235–238.

Encinar, J.A. (1996). Design of a dual frequency reflectarray using microstrip stacked patches of variable size. **IEE Electronics Letters**. 32(12): 1049 1050.

Encinar, J.A. (2001). Design of Two-Layer Printed Reflectarray Using Patches of Variable Size. **IEEE Transactions on Antennas and Propagation**. 49(10): 1403–1410.

Encinar, J.A., Datashvili, L.Sh., Zornoza, J.A., Arrebola, M., Sierra-Castaner, M., Besada-Sanmartin, J.L. (2006). Dual-polarization dual-Coverage reflectarray for space applications. **IEEE Transactions on Antennas and Propagation**. 54(10): 2827–2837.

Encinar, J.A., and Zornoza, J.A. (2003). Broadband design of three-layer printed reflectarrays. **IEEE Transactions on Antennas and Propagation**. 51: 1662-1664.

Encinar, J.A., and Zornoza, J.A. (2004). Three-layer printed reflectarray for contoured beam space application. **IEEE Transactions on Antennas and Propagation**. 52(5): 1138-1148.

Evans, G.E. (1990). **Antenna Measurement Techniques**. Artech House, Norwood, MA.

Fang, H., Lou, M., Huang, J., Hsia, L.M., and Kerdanyan, G. (2001). An Inflatable/Self-Rigidizable Structure for the Reflectarray Antenna. **Proc. 10th European Electromagnetic Structure Conference** (Munich, Germany).

Fernandes, C.A. and Fernandes, J.G. (1999). Performance of Lens Antennas in Wireless Indoor Millimeter-wave Applications. **IEEE Transactions on Microwave Theory Technology.** 47(6):732-737.

Fusco, V. F. (2005). Mechanical beam scanning reflectarray. **IEEE Transactions on Antenna and Propagation**. 53(11): 3842-3844.

Gao, Y.T. and Barton, S.K. (1995). Phase Correcting Zonal Reflector Incorporating Rings. **IEEE Transactions on Antennas and Propagation**. 43(1): 350–355.

Ginn, J.C., Lail, B.A., and Boreman, G.D. (2007). Phase characterization of reflectarray elements at infrared. **IEEE Transactions on Antennas and Propagation**. 55(11): 2989-2993.

Girard, E., Moulinet, R., Gillard, R., and Legay H. (2002). An FDTD Optimization of a Circularly Polarized Reflectarray Unit Cell. **Proc. IEEE APS/URSI Symposium** (San Antonio, Texas). 1: III-136–III-139.

Han, C. and Chang, K. (2003). Ka-band reflectarray using ring elements. **IEE Electronics Letters.** 39(6): 491– 493.

Han, C., Huang, J., and Chang, K. (2005). A high offset-fed X/Ka-dual band reflectarray using thin membranes. **IEEE Transactions on Antennas and Propagation**. 53(9): 2792-2798.

Han, C., Rodenbeck, C., Huang, J., and Chang, K. (2004). A C/Ka dual frequency dual layer circularly polarized reflectarray antenna with microstrip ring elements. **IEEE Transactions. on Antenna and Propagation**. 52(11): 2871-2876.

Han, C., Strassner B., Chang K., and Huang J. (2003). A Dual-Frequency 7/32 GHz Reflectarray Antenna. **Digest Progress in Electromagnetics Research Symposium (PIERS)** (Honolulu, Hawaii). 1: 526.

Hay, S.G., Bateman, D.G., Bird, T.S., and Cooray, F.R. (1999). Simple Ka-band Earth Coverage Antennas for LEO Satellites. **Proc. IEEE International Symposium Antennas and Propagation**. 1: 11–16.

Hodges, R. and Zawadzki, M. (2005). Design of a Large Dual Polarized Ku-Band Reflectarray for Spaceborne Radar Altimeter. **Proc. IEEE International Symposium Antennas and Propagation** (Monterey, California). 1: 4356–4359.

Huang, J. (1990). Microstrip reflectarray antenna for SCANSCAT radar application. **JPL Publication 90-45**.

Huang, J. (1991). Microstrip Reflectarray. **Proc. 1991 IEEE Antennas and Propagation Symposium** (London, Ontario, Canada). 1: 612–615.

Huang, J. (1994). Analysis of a Microstrip Reflectarray Antenna for Microspacecraft Applications. **The Telecommunications and Data Acquisition Progress Report 42-120**. Jet Propulsion Laboratory, Pasadena, California. 1: 153–173.

Huang, J. (1995). Bandwidth Study of Microstrip Reflectarray and a Novel Phased Reflectarray Concept. **Proc. IEEE International Symposium Antennas and Propagation** (Newport Beach, California). 1: 582–585.

Huang, J. (1996). Capabilities of Printed Reflectarray Antennas. **Proc. IEEE Symposium on Phased Array Systems and Technology** (Boston, Massachusetts). 1: 131–134.

Huang, J. and Feria, A. (1999). A 1-m X-Band Inflatable Reflectarray Antenna. **Microwave and Optical Technology Letters.** 20: 97–99.

Huang, J.V., Feria, A. and Fang, H. (2001). Improvement of the Three-Meter Ka-Band Inflatable Reflectarray Antenna. **Proc. IEEE International Symposium Antennas and Propagation** (Boston, Massachusetts). 1: 122–125.

Huang, J. and Pogorzelski, R.J. (1998). A Ka-Band Microstrip Reflectarray with Elements Having Variable Rotation Angles. **IEEE Transactions on Antennas and Propagation**. 46(5): 650–656.

Hum, S.V., Okoniewski, M., and Davies, R. J. (2005). Realizing an electronically tunable reflectarray using varactor diode-tuned elements. **IEEE Microwave and Wireless Components Letters**. 15(6): 422–424.

Itoh, T. (1989). Numerical Techniques for Microwave and Millimeter-Wave Passive Structures. Wiley-Interscience, New York.

Javor, R.D., Wu, X.D., and Chang, K. (1994). Beam Steering of a Microstrip Flat Reflectarray Antenna. **Proc. 1994 IEEE International Antennas and Propagation Symposium** (AP-S/URSI, Seattle, Washington). 1: 956–959.

Javor, R.D., Wu, X.D., and Chang, K. (1995). Design and performance of a microstrip reflectarray antenna. **IEEE Transactions on Antenna and Propagation**. 43(9): 932-939.

Johansson, F.S. (1990). A New Planar Grating-Reflector Antenna. **IEEE Transactions on Antennas and Propagation**. 38: 1491–1495.

Kelkar, A. (1991). FLAPS: Conformal Phased Reflecting Surfaces. Proceedings of the 1991 **IEEE National Radar Conference** (Los Angeles, California). 1: 58–62.

Khayatian, B. and Rahmat-Samii, Y. (2003). Characterizing Reflectarray Antenna Radiation Performance. **IEEE International Symposium Antennas and Propagation** (Columbus, Ohio) 3: 298–301.

Kin-Lu Wong (2002) **Compact and Broadband Microstrip Antenna**. John Wiley & Sons: New York.

Kishk, A.A. (1989). Simple Primary Focus Feeds for Deep Reflector. **Proc. IEE.** 136: 169–171.

Kurup, D.G., Himdi, M., and Rydberg, A. (2003). Design of an unequally spaced reflectarray. **IEEE Antennas and Wireless Propagation Letters**. 2(1): 33-35.

Lee, K.F., and Chen, W. (1997). **Advances in Microstrip and Printed Antennas**. John Wiley and Sons, New York.

Leberer, R., and Menzel, W. (2005). A dual planar reflectarray with synthesized phase and amplitude distribution. **IEEE Transactions on Antenna and Propagation**. 53(11): 3534-3539.

Love, A.W. (1978). **Reflector Antenna**. IEEE press.

Martynyuk, A.E., Lopez, J.I.M., and Martynyuk, N.A. (2004). Spiraphase-type reflectarrays based on loaded ring slot resonators. **IEEE Transactions on Antenna and Propagation**. 52(1): 142-153.

Menzel, W., Pilz D., and Al-Tikriti, M. (2002). Millimeter-Wave Folded Reflector Antennas with High Gain, Low-Loss, and Low Profile. **IEEE Antennas and Propagation Magazine.** 44(3): 24–29.

Metzler, T.A. (1993). **Design and Analysis of a Microstrip Reflectarray**, Ph.D. Dissertation, University of Massachusetts, Amherst.

Misran, N., Cahill, R., and Fusco, V.F. (2003). Concentric split ring element for dual frequency reflectarray antennas. **IEE Electronics Letter**s. 39(25): 1776-1777.

Misran, N., Cahill, R., and Fusco, V.F. (2003). RCS reduction technique for reflectarray antennas. **IEE Electronics Letter**s. 39(23): 1630-1632.

Misran, N., Cahill, R., and Fusco, V.F. (2003). Design optimisation of ring elements for broadband reflectarray antennas. **IEE Proceedings Microwaves, Antennas and Propagation**. 150(6): 440-444.

Mittra, R., Chan, C.C., and Cwik T. (1988). Techniques for Analysing Frequency Selective Surfaces - A Review**. Proceedings of IEEE**. 76(12):1593-1615.

Munson, R.E., Haddad, H.A., and Hanlen, J.W. (1987). Microstrip Reflectarray for Satellite Communication and RCS Enhancement or Reduction. **U.S. patent 4,684,952,** Washington, District of Columbia.

Olver, A.D., Clarricoats, P.J.B., Kishk, A.A., and Shafai, L. (1994). **Microwave Horns and Feeds**, IEEE, New York.

Phelan, H.R. (1977). Spiraphase Reflectarray for Multitarget Radar. **Microwave Journal.** 20: 67–73.

Pilz, D. and Menzel, W. (1998). Foled reflectarray antenna. **IEE Electronics Letters**. 34(9): 832-833.

Pozar, D.M. (1989). Analysis and Design Considerations for Printed Phased Array Antenna. **Microstrip Antenna Handbook**, Peter Peregrinus, London.

Pozar, D.M. (2003). Bandwidth of reflectarrays. **IEE Electronics Letters.** 39(21): 1490–1491.

Pozar, D.M. and Metzler, T.A. (1993). Analysis of a Reflectarray Antenna Using Microstrip Patches of Variable Size. **Electronics Letters**. 29(8): 657–658.

Pozar , D.M., and Schaubert, D.H. (1995). Microstrip Antennas: The Analysis and Design of Microstrip Antennas and Arrays. IEEE Press, New York.

Pozar, D.M., Targonski, S.D., and Pokuls, R. (1999). A Shaped-beam Microstrip Patch Reflectarray. **IEEE Transactions on Antenna and Propagation**. 47: 1167-1173.

Pozar, D., Targonski, S.D., and Syrigos, H.D., (1997). Design of Millimeter Wave Microstrip Reflectarrays. **IEEE Transactions on Antennas and Propagation**. 45(2): 287–296.

Rengarajan, S. R. (2005). Choice of basis functions for accurate characterization of infinite array of microstrip reflectarray elements. **IEEE Antennas and Wireless Propagation Letters**. 4: 47-50.

Shaker, J., and Cuhac, M. (2005). Multi-band, multi-polarisation reflector-reflectarray antenna with simplified feed system and mutually independent radiation patterns," **IEE Proceedings Microwaves, Antennas and Propagation**. 152(2): 97–101.

Smulders, P.F.M. and Herben, M.H.A.J. (2001). A Shaped Reflector Antenna for 60-GHz Radio Access Points. **IEEE Transactions on Antennas and Propagation**. 49:1013–1015.

Smulders, P.F.M., Khusial, S., and Herben, M.H.A.J. (2001). A Shaped Reflector Antenna for 60-GHz Indoor Wireless LAN Access Points. **IEEE Transactions on Vehicular Technology.** 50(2): 584-591.

Strassner, B., Han, C., and Chang K. (2004). Circularly polarized reflectarray with microstrip ring elements having variable rotation angles. **IEEE Transactions on Antenna and Propagation**. 52(4): 1122-1125.

Targonski, S.D. and Pozar, D.M. (1994). Analysis and design of a microstrip reflectarray using patches of variable size. **Proc. IEEE International Symposium Antennas and Propagation** (Seattle, WA). 1: 1820-1823.

Tolkachev, A.A., Denisenko, V V., Shishlov, A.V., and Shubov, A.G. (1996). High-Gain Antenna System for Millimeter-Wave Radars with Combined

Electrical and Mechanical Beam Steering. **Proc. IEEE Symposium on Phased Array Systems and Technology**. 1: 266–271.

Tsai, F.-C.E. and Bialkowski, M.E. (2003). Designing a 161-element Ku-band microstrip reflectarray of variable size patches using an equivalent unit cell waveguide approach. **IEEE Transactions on Antennas and Propagation**. 51(10): 2953-2962.

Venneri. F., Costanzo, S., Di Massa, G., and Angiulli, G. (2005). An improved synthesis algorithm for reflectarrays design. **IEEE Antennas and Wireless Propagation Letters**. 4: 258–261.

Wang, J.J.H. (1991). **Generalized Moment Methods in Electromagnetics**. New York: John Wiley & Sons.

Wiley-Interscience (1979). **IEEE Standard Test Procedures for Antenna**. IEEE Ttd 149-1979, IEEE.

Wongsan, R., Thaivirot, V. (2006). Synshesis of Radiation Pattern of Variety of Shaped Backscatters Using Physical Optic. **Proc. the 2006 Electrical Engineering, Computer, Telecommunications and Information Technology (ECTI) International Conference**. 1: 155-158.

Wu, D.I., Hall, R.C., and Huang, J. (1995). Dual-frequency microstrip reflectarray. **Proc. IEEE International Symposium Antennas and Propagation**. 4:2128-2131.

Wu, Z. H., Zhang, W. X., Liu, Z. G., and Shen, W. (2005). Circularly polarised reflectarray with linearly polarised feed. **IEE Electronics Letters**. 41(7): 387–388.

Zawadzki M. and Huang, J. (2003). A Dual-Band Reflectarray for X- and Ka-Bands. **Digest Progress in Electromagnetics Research Symposium (PIERS)** (Honolulu, Hawaii). 1: 525.

Zhang, Y., Wu, K.L., Wu, C., and Litva, J. (1993). Microstrip Reflectarray: Full-Wave Analysis and Design Scheme. **Proc. IEEE International Symposium Antennas and Propagation** (Ann Arbor, Michigan). 1: 1386–1389.

Zich, R.E., Mussetta , M., Tovaglieri, M., Pirinoli, P., and Orefice, M. (2002). Genetic Optimization of Microstrip Reflectarrays. **Proc. IEEE International Symposium Antennas and Propagation**. 1: III-128–III-131.

APPENDIX

PUBLICATIONS RELATED TO

THE PhD RESEARCH

International Journal Paper

Krachodnok, P. and Wongsan, R. (2008). Performance Improvement in the Design of Broad-Beam Microstrip Reflectarray. ***Engineering Letters*.** 16(1): 68-75.

Krachodnok, P. and Wongsan, R. (2008). Design of Broad-Beam Microstrip Reflectarray. ***WSEAS Transactions on COMMUNICATIONS***.

International Conference Papers

Krachodnok, P. and Wongsan, R. (2006). Design of Microstrip Reflectarray Antenna Using Backscattering Technique. ***Proc. The International Technical Conference on Circuits/Systems, Computers, and Communications***. 3:513-516.

Krachodnok, P. and Wongsan, R. (2007). Performance Improvement of Broad-Beam Microstrip Reflectarray by Reduction of Elements Spacing. ***Proc. the 2007 Electrical Engineering, Computer, Telecommunications and Information Technology (ECTI) International Conference***. 2: 604-607.

Krachodnok, P. and Wongsan, R. (2007). Design and Performance Improvement of Broad-Beam Microstrip Reflectarray. ***The 2007 International Conference of Electrical and Electronics Engineering***. 1: 429-433.

Krachodnok, P. and Wongsan, R. (2007). Optimum Design of Broad-Beam Microstrip Reflectarray. ***The 11th WSEAS International Conference on COMMUNICATIONS***. 1: 121-126.

Krachodnok, P. and Wongsan, R. (2007). Synthesis of Phase and Radiation Pattern for Microstrip Reflectarray using Discretization of Elementary Geometrical Functions. ***The 2007 International Symposium on Antennas and Propagatio***. 1: 1286-1289.

Krachodnok, P. and Wongsan, R. (2007). Broad-Beam Microstrip Reflectarray Using Gaussian Backscatter Function. ***The Second European Conference on Antennas and Propagation***. 1: 387-388.

BIOGRAPHY

Miss Piyaporn Krachodnok was born in Khon Kaen, Thailand, in 1974. She graduated with the Bachelor Degree of Engineering in Telecommunication Engineering in 1996 from Suranaree University of Technology, Nakhon Ratchasima, Thailand, and she had worked at this University for a year. After that, she attended Chulalongkorn University, Bangkok, Thailand and received a Master Degree in Electrical Engineering in 2001. She has been with the School of Telecommunications Engineering, Suranaree University of Technology, Thailand since 2001, and is currently working toward the Ph.D. degree in the same place. Her research interests the electromagnetic wave applicationsand antenna theory/design.